Charged Hadron Production in Pb-Au Collisions at 158 AGeV/c

INAUGURAL-DISSERTATION

Federica Ceretto

INAUGURAL-DISSERTATION
zur
Erlangung der Doktorwürde
der
Naturwissenschaftlich-Mathematischen
Gesamtfakultät
der
Ruprecht-Karls-Universität
Heidelberg

vorgelegt von
Dipl.-Phys. Federica Ceretto
aus Cuorgné (Turin-Italien)

Tag der mündlichen Prüfung: 6. Mai 1998

Charged Hadron Production
in Pb-Au Collisions at 158 AGeV/c

Gutachter: Prof. Dr. Johann Peter Wurm
Priv. Doz. Dr. Norbert Herrmann

Charged Hadron Production in Pb-Au Collisions at 158AGeV/c

This work concentrates on hadronic observables in ultra relativistic heavy ion interactions. The data were taken at the CERN-SPS in the fall of 1995.

Although the CERES experiment was originally designed to measure electron-positron pairs, it incorporates several possibilities to detect hadrons since it was upgraded in 1994.

In this work the production of charged hadrons close to midrapidity is studied. While the multiplicity of charged particles increases when approaching more central collisions, the width of the pseudorapidity distribution becomes narrower. This implies that a higher degree of stopping is achieved in the most central collisions.

The pion transverse mass spectra show a deviation (concave shape) from an exponential shape. This deviation decreases with increasing centrality. The local slope of those spectra is for $m_t > 3\ GeV/c^2$ comparable to the value obtained in p-p collisions. However, for $m_t < 2.5\ GeV/c^2$ a clear difference is observed. The 'proton' m_t-spectra, extracted by subtracting the distributions of positive and negative hadrons, also exhibit a centrality dependence which is strong only at small m_t.

Produktion geladener Hadronen in Pb-Au Kollisionen bei 158 AGeV/c

Diese Arbeit beschäftigt sich mit dem Studium hadronischer Observablen in ultrarelativistischen Kollisionen. Die Messungen hierfür wurden 1995 am CERN-SPS mit dem CERES Experiment durchgeführt.

Obwohl CERES ursprünglich für die Detektion von Elektron-Positron Paaren konzipiert worden ist, besteht seit der Erweiterung des Experimentes im Jahr 1994 zusätzlich die Möglichkeit, geladene Hadronen zu messen.

Im Rahmen dieser Arbeit wird die Produktion geladener Hadronen in Bereich mittlerer (Pseudo-)Rapiditäten untersucht. Während die Multiplizität der geladenen Hadronen mit der Zentralität der Kollisionen zunimmt, wird die Breite der Pseudorapiditätsverteilung deutlich kleiner. Hieraus kann auf ein gr"o"seres Ma"s des 'Abstoppens' der Kerne in zentralen Stössen geschlossen werden.

Die Analyse der Pion m_t (transversale Masse) Verteilungen zeigt eine deutliche Abweichung (konkave Form) von einer exponentiellen Form. Diese Abweichung wird allerdings geringer mit zunehmender Zentralität. Eine Studie des lokalen Gradienten der Pion m_t-Spektren ergab, da"s dieser im Bereich $m_t > 3\ GeV/c^2$ mit Werten aus p-p Kollisionen vergleichbar wird. Für $m_t < 2.5\ GeV/c^2$ ergibt sich jedoch ein klarer Unterschied zu p-p Reaktionen. Die m_t-Spektren der Protonen, bestimmt über die Differenz der Spektren positiven und negativen Hadronen, zeigen ebenfalls eine Zentralitätsabhängigkeit des lokalen Gradienten. Diese ist aber nur ausgeprägt bei kleinen transversalen Massen, bzw. transversalen Impulsen.

Table of Contents

Chapter 1

Introduction

In the last years, both, the Brookhaven National Laboratory (BNL) in the United States of America and the Conseil Européen de la Recherche Nucléaire (CERN) in Europe have succeeded to accelerate Au and Pb ions to very high energies, 11 AGeV and 158 AGeV respectively. In reactions of those beams with fixed targets of heavy elements, it is possible to create, in the laboratory, energy densities which might have existed only during the very early stages of the universe. Using heavy ion reactions, where a hot and dense nuclear matter is formed in a small volume which is, however, much larger than in p-p collisions, one hopes to approach conditions favorable to the formation of a new state of matter, the quark-gluon plasma.

Dedicated experiments have been designed and built to analyze the products of such collisions. Various signals, associated to the different stages of the reaction, can be systematically studied.

The main purpose of the CERES (ChErenkov Ring Electron Spectrometer) experiment is to measure low mass electron-positron pairs produced in hadron-nucleus and nucleus-nucleus collisions. Electron pairs, as well as photons and lepton pairs in general, are ideal probes due to the absence of strong final state interactions. The detection of those low mass electron pairs which have a production probability smaller than 10^{-5} relative to pions in the environment of Dalitz decays, conversion pairs and hundreds of pions per event has already been described elsewhere [1, 2].

In addition to dilepton detection, the CERES experiment is capable to measure many other quantities, which also provide informations useful to characterize heavy-ion collisions. The global event features specify the initial conditions of the interaction. From the multiplicity of the charged particles and their rapidity distribution, one can derive the impact parameter and subsequently the energy density reached in the collision. Information on the expansion and cooling of the system during the hadron gas phase, can be obtained by investigating the transverse momentum spectra of the produced particles.

The methods presented here will allow to measure p_t spectra of identified charged pions until 4 GeV/c, well in the realm of perturbative QCD. This opens the exciting possibility to investigate the transition from early parton scattering to preequilibrium or thermal pion emission via the p_t, y and N_{ch} dependence of the spectral slopes.

Based on two Ring Imaging Cherenkov detectors (RICH) to identify particles and a solenoidal magnetic field to measure momenta, CERES was upgraded in 1994. To enhance the track reconstruction efficiency a Pad-Chamber was installed at the end of the experiment together with a doublet of Silicon Drift detectors located behind the target but upstream of the RICHes. Those modifications added excellent hadron detection capabilities to CERES.

In this work, the production of charged hadrons is studied for the data taken during the beam time in the fall of 1995. After a brief discussion of the relativistic heavy ion collisions in chapter 2, chapter 3 will describe the experimental methods. An overview of the tracking strategy and calibration procedures is given in chapter 4. The Monte-Carlo simulation of the spectrometer, fundamental for the data correction, is reported in chapter 5. The hadronic signals derived by this analysis are presented in details as function of the centrality of the collision. In particular, the multiplicity distribution and the obtained charged particle pseudorapidity densities are described in chapter 6. In chapter 7, it is shown how the combination of the silicon drift detectors and the Pad Chamber permits the extraction of the transverse mass spectra of negative hadrons and of the positive charge excess. The full spectrometer was extremely useful to identify high momentum positive and negative pions. Their spectra are presented in chapter 8. Finally, chapter 9 contains a discussion of the results and the conclusions.

Chapter 2

A New State of Matter

2.1 QCD Phase Transition

The strong interaction which stabilizes nuclei is described by quantum chromodynamics (QCD). In analogy to the quantum electrodynamics (QED), the force between the carriers of color charge, the *quarks*, is mediated by exchange of particles, the so-called *gluons*.

The strength of the interaction, described by the strong coupling 'constant' α_s, depends on the the momentum transfer between the constituents. In case of large momentum transfer ($\alpha_s << 1$) interactions can be calculated perturbatively. While in perturbative QCD a lot of progress has been made by solving many problems, the analytical or numerical solutions in non-perturbative QCD are very difficult to obtain. At present, numerical calculations on the lattice [3] permit to investigate some features of the long range behavior of the strong interactions.

One of the most interesting results is that, for high energy density, lattice QCD predicts a *phase transition* to a new state of matter in which quark and gluons are *deconfined*, the so-called Quark-Gluon Plasma (QGP). Fig. 2.1 shows the dependence of the energy density ε and pressure P from the temperature T obtained from lattice calculations: the energy density rises rapidly at a critical temperature of $\sim 160MeV$ whereas the pressure increases only moderately. This effect has been associated to a phase transition [4].

In Fig. 2.2 a phenomenological phase diagram of strong interacting matter is presented. The early universe, during its expansion, has probably undergone $10^{-5} - 10^{-6}$ s after the Big Bang the phase transition from QGP to hadronic matter. At the other extreme, for high densities about 5-10 times the normal nuclear density, the core of neutron stars could eventually also be in a different phase (strange matter condensate [6]) than normal nuclear matter. Since those events can not be studied directly (apart from measurements of pulsar rotational frequencies), other possibilities to form a QGP need to be explored. Because of the high energy and baryon density reached in an ultra relativistic heavy ion collisions, such reactions may provide a possibility to produce the QGP in the laboratory.

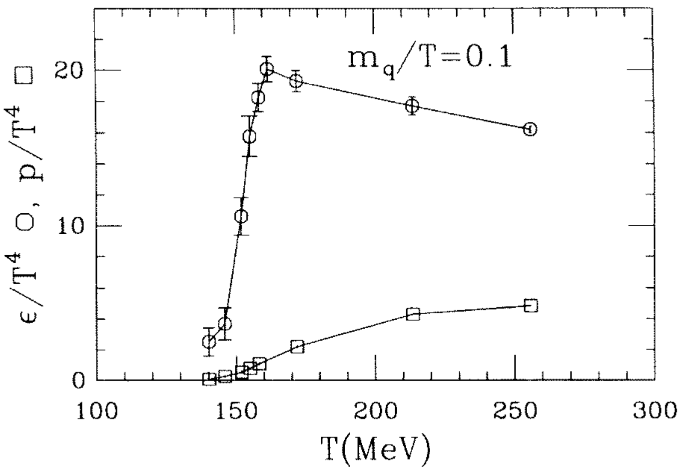

Figure 2.1: Energy density ε and pressure P as function of temperature T [4].

2.2 Signatures of a Quark-Gluon Plasma

Many different experimental observables have been proposed during the last 10 years as possible signatures for the QGP formation. Usually, the attention is on signals which come directly from the hot and dense phase of the reaction and are not influenced by the high number of hadrons produced in the collisions. The signals that are at present mostly discussed are an enhancement of the production of strange particles, the J/Ψ suppression and the enhanced production of dileptons and thermal photons.

- In hadronic reactions the production of particles containing strange quarks is normally suppressed due to the high mass of the s-quark (500 MeV/c^2) compared to the u and d-quarks. In the presence of QGP, the expected reduction of the s-quark mass to 150 MeV/c^2 should favor the enhancement of production of multi-strange baryons and strange antibaryons [7, 8].

- The J/Ψ mesons are produced in nucleon-nucleon interactions by the process

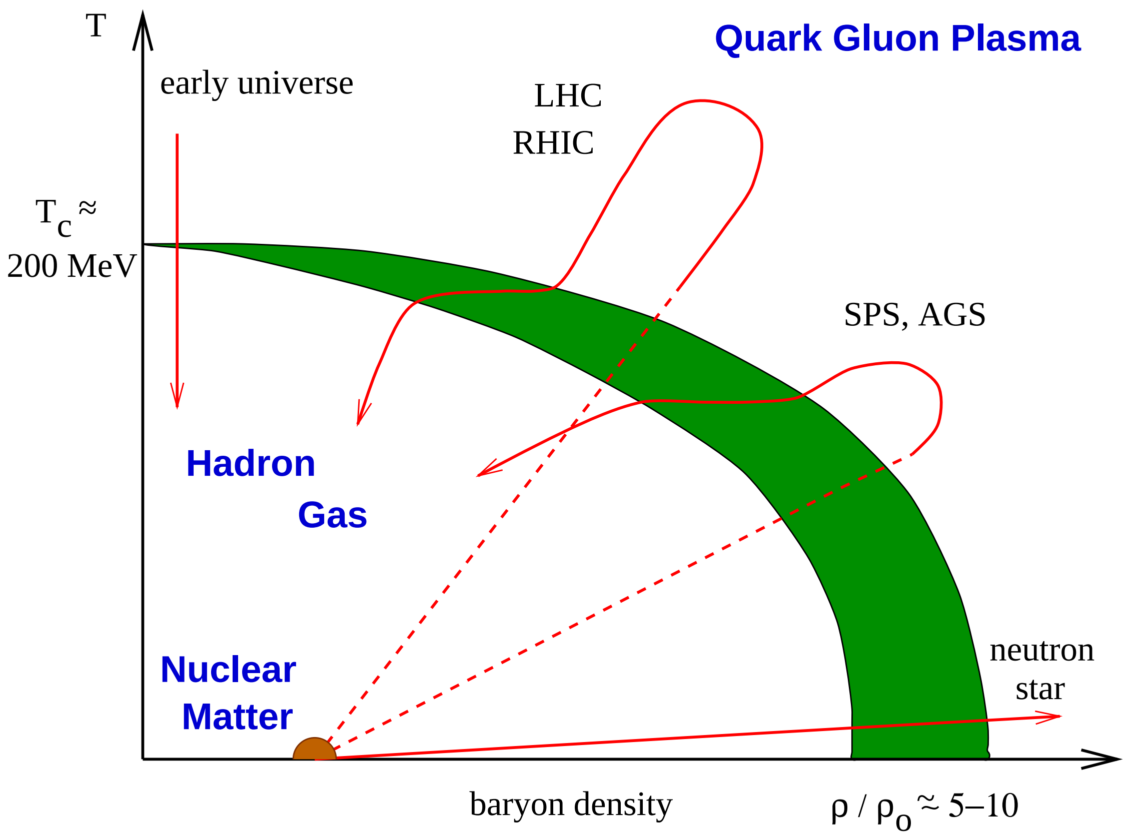

Figure 2.2: The phase diagram of strongly interacting matter. The plot shows the hadronic phase at low temperature and baryon density, the transition region (mixed phase) and the QGP phase. The lines illustrate the trajectory followed in supernovae explosions, Big Bang evolution, and (possibly) in heavy-ion reactions at present and future accelerators.

$g + g \longrightarrow c + \bar{c}$. In a QGP J/Ψ mesons should be suppressed because of the screening effect from free color charges on the two c-quarks [9, 10].

- Another signature are dileptons and thermal photons formed in the QGP via the $q\,\bar{q}$ annihilation or $q\,g$ Compton scattering. Since they are not affected by the strong final state interaction, their production, which is highly correlated with the temperature of the QGP, probes the interior of the quark-gluon plasma during the earliest and hottest phase of the evolution. Lepton pairs from hadronic sources in the invariant mass range between 0.5 and 1 GeV/c^2 can provide exclusive information about possible medium modification of hadronic properties, especially of the ρ-meson, at high density where the chirial symmetry might be approached [11, 12]. Unfortunately, the yield of such probes is rather small and must compete with large background sources coming from hadronic processes, in particular from electromagnetic hadron decays.

2.3 Ultra-Relativistic Heavy Ion Collisions

To analyze and study the properties of a quark-gluon plasma, ultra-relativistic heavy ion collisions have been proposed as a possibility for the laboratory production of this new state of matter. The large densities and high temperatures that are achieved for example in a central Pb-Pb collision, represent a favorable condition for the QGP formation.

The evolution of an ultra-relativistic heavy ion reaction is sketched in Fig. 2.3. One can distinguish different phases: the first moments of the interaction are characterized by the formation of a high density region in which the original beam energy is redistributed into other degrees of freedom. In the case of QGP formation, after a short time, usually taken as $\tau_0 = 1$ fm/c, partons materialize in this highly energetic matter and eventually build a thermalized system. In the successive stage, due to the rapid expansion and cooling of the plasma, a mixed phase of hadrons and partons is formed. In the case of a first order phase transition, the system spends a relatively long time in the mixed phase until a hadron gas is formed. The still interacting system expands until the *freeze-out*[1] occurs at the time τ_f and a large number of hadrons are emitted.

Ultra-relativistic heavy ion collisions have been discussed in the context of two extreme pictures with essentially different physics. The first is consistent with the Landau picture, in which the *participant* baryons from projectile and target nuclei are fully stopped during the collision before they start expanding into longitudinal and transverse direction. The consequence is the transient formation of a baryon rich matter in the middle of the reaction zone and eventually a baryon rich QGP.

The second picture is described by the Bjorken model [5] in which the initial target and projectile are so far apart in phase space that the collision will not slow them down completely. The particle production begins with the interpenetration of the two nuclei and continues also after the colliding nucleons have separated. In this case, the baryon rapidity distribution should show a wide plateau which extends over several units of rapidity. If the QGP is formed, it would be a baryon poor plasma similar to the one formed in the early stage of the universe.

From the present experimental data it is however very complicated to clearly decide which picture is more appropriate to describe heavy ion collisions at CERN SPS energies. As shown by model calculations [13] the analysis of p_t-spectra alone is not sufficient for this task. Therefore, other additional hadronic observables need to be considered. Their systematic dependence on centrality might provide new informations which will improve the understanding of the global characteristics of ultra relativistic heavy ion reactions. Comparisons of the results with both empirical observations (i.e. known pp and pA systematics) and theoretical models

[1] Freeze-out is the condition in which the interactions cease and the particle stream freely away toward the detectors

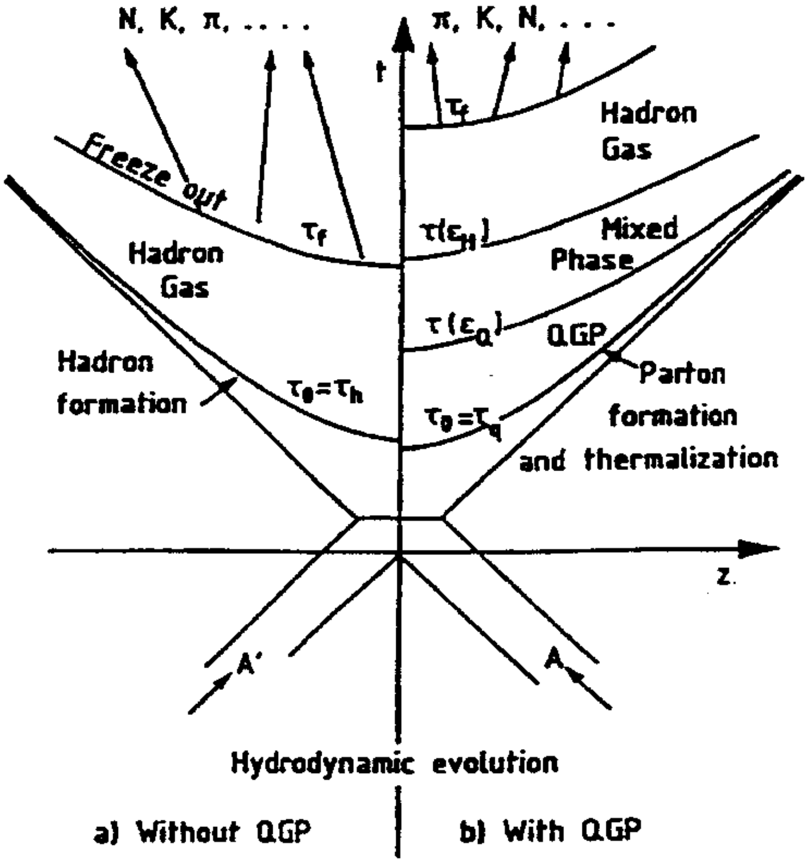

Figure 2.3: Schematic evolution of a heavy ion interaction in the scenario with (right) or without (left) QGP formation.

(i.e. hydrodynamical and random walk approaches) are also necessary to develop a comprehensive picture and obtain more inside into this field.

Chapter 3

The CERES Experiment

The main goal of the CERES[1] experiment at the CERN Super Proton Synchrotron (SPS) is to systematically measure electron-positron pairs produced in hadron-nucleus and nucleus-nucleus collisions [14, 15, 16]. The spectrometer was appositely designed to tackle this experimental challenge and to cope with the high physical background characteristic of heavy ion interactions. Therefore all aspects of the system have been optimized. CERES was approved for the first time in 1989, after successful measurements with proton and sulphur beams, it became upgraded in 1994 for the Pb beam. The essential characteristics of the this setup are summarized in the following chapter.

3.1 Experimental Setup

Fig. 3.1 presents a schematic view of the CERES experiment as used in the 95 data taking [17, 18]. Lead beam particles coming from the left hand side, interact in one of eight gold target discs. The charged particles produced in the collision generate signals in two silicon drift detectors (SDD) situated in the *target area*. Successively, they cross the radiators of two azimuthally symmetric Cherenkov detectors (RICH1 and RICH2). Their task is to identify electrons and measure their momenta via the azimuthal deflection in the magnetic field which is produced by a super-conducting magnet system in between the two RICH detectors.

At the downstream end of the spectrometer, at about $3m$ from the target, an additional point is measured on each charged particle trajectory using a Multi Wire Proportional Chamber with Pad-readout (Pad Chamber). Together with the two SDDs, it constitutes an excellent tracking device which is of central importance for

[1]ChErenkov Ring Electron Spectrometer

the analysis presented in this thesis.

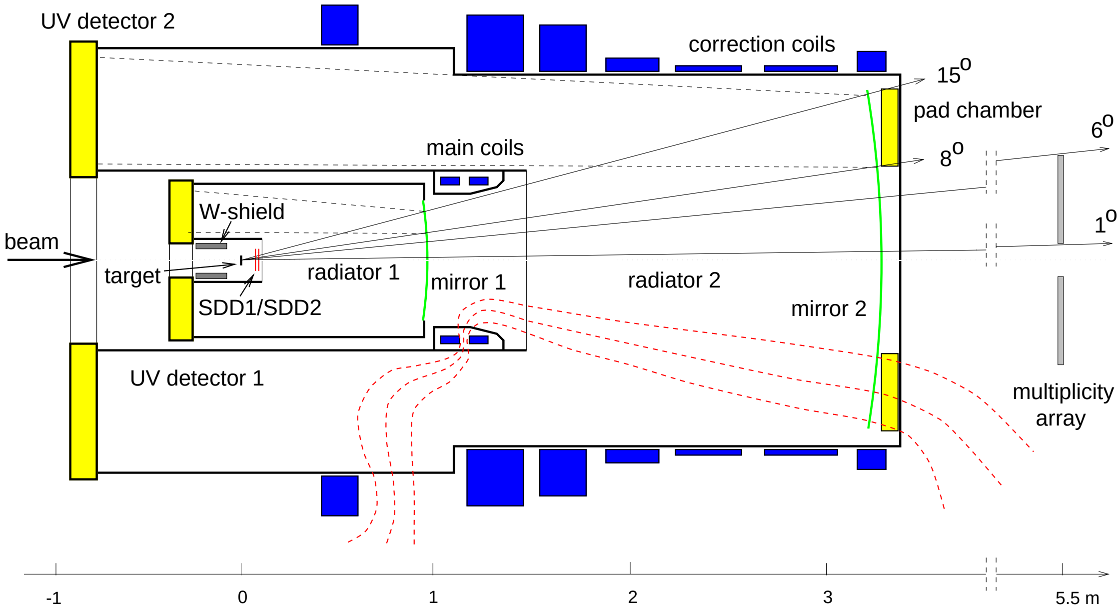

Figure 3.1: Schematic view of the CERES experiment.

3.2 The Target Region

The target region shown in Fig. 3.2, is situated at the upstream end of the spectrometer. It consists of the target itself and two radial silicon drift detectors, all concentrated in a limited volume of $\sim 12cm$ length and $\sim 14cm$ diameter. Both the target and the SDD are mounted in a carbon tube independent from the rest of the spectrometer. The tube is surrounded by a cooling system needed to isolate the silicon wafers from the rest of the spectrometer which is heated to $50^o\ C$ (see section 3.3).

3.2.1 The Target

For the 1995 run a new segmented gold target was realized with the aim of minimizing the number of δ electrons produced by the Pb projectile as well as the number of photons converting into e^+e^- pairs in the target. It is composed of eight Au discs of $25\mu m$ thickness and $600\mu m$ width, which give a total nuclear interaction probability of about 0.5%. The spacing of $3mm$ is chosen such that particles emitted into the spectrometer acceptance do not traverse any of the successive discs. Within the acceptance, the thickness of the target is therefore on average only 0.22% of a radiation length.

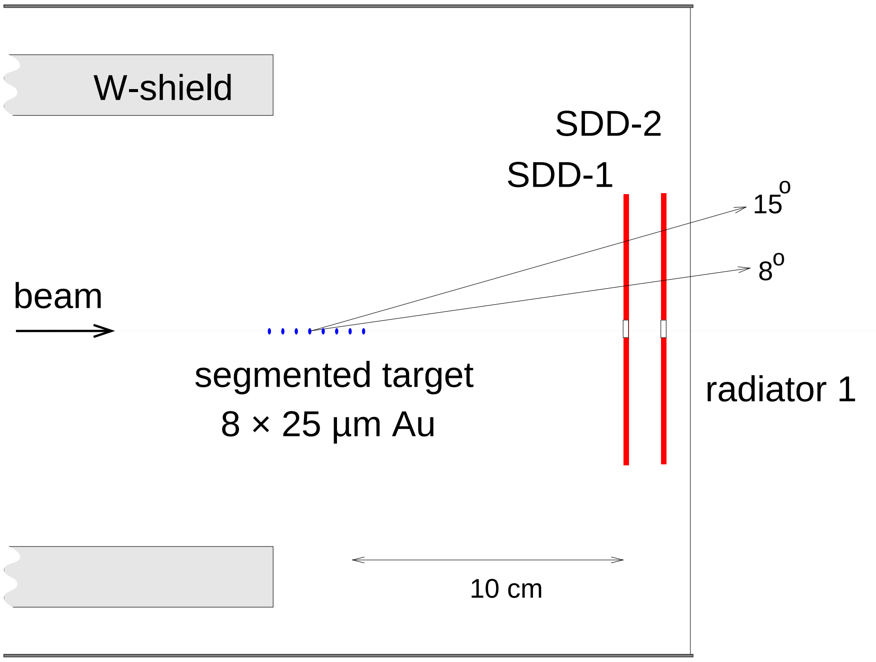

Figure 3.2: The target region.

3.2.2 The SDD Detectors

CERES was the first experiment using radial silicon drift chambers. These novel detectors offer the possibility to measure energy loss and coordinates of hundreds of charged particles with high spatial resolution and high interaction rate. To match the already present spectrometer and its full azimuthal coverage, the detectors were designed with an annular shape and radial symmetry [19].

The silicon drift detectors which are a central part of the event and track reconstruction in the CERES experiment provide:

- a very precise and independent vertex reconstruction [20];
- a very accurate off-line event characterization by the pseudo-rapidity density of charged particles $dn_{ch}/d\eta$;
- track reconstruction before the magnetic field and, for electrons and high momentum pions, an *a priori* knowledge of the ring-center location in RICH1;
- a powerful rejection of photon conversions.

During the 1995 beam time, two types of silicon drift detectors were used: one consisting of a 3″ and the other of a 4″ silicon wafer. The working principle is the same for both detectors (Fig. 3.3). A charged particle that crosses the depleted silicon produces an electron cloud which, due to the presence of an external electric field, drifts towards the outer limit of the wafer. Here 360 anodes connected with

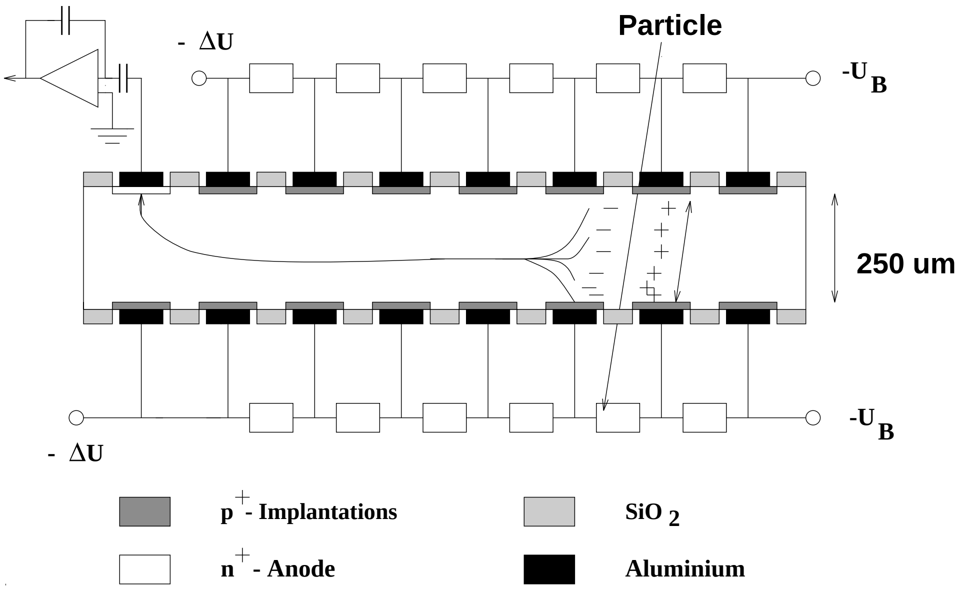

Figure 3.3: The working principle of the Silicon Drift Detector. The ionized electrons are collected in the center of the detector and then drifted toward the anode region under the influence of the drift field generated by the voltage U_B.

the readout chain, collect the charge. The signal is amplified by a charge sensitive amplifier, shaped in a quasi-Gaussian form and then send to an FADC (Flash Analog Digital Converter) system where it is digitized with a sampling frequency of $50MHz$.

The radial position of the track is reconstructed using the drift-time information. The azimuthal angle is given by the anode or by the center of gravity of all neighboring anodes that have collected the charge.

Although the principle is the same, the two detectors differ in several aspects. The $3''$ chamber is an improved design of the detectors used in previous beam times. It has an active radius of 28 mm, defined by 241 field rings which are separated by 120 μm. The drift field, produced by implanted voltage dividers (12 for each field ring), has a nominal value of 500 V/cm that results in a drift velocity of 6.6 $\mu m/ns$. The maximum drift time of the electron cloud is 4.4 μs.

Due to imperfections in the layout, the field rings are not completely radially symmetric but are approximated by 120 concentric regular polygons on both surfaces on the detector. Each side of the polygons spans 3^o, here the field lines are straight. On the original detector this approximation caused a deviation from the expected, ideal radial field in the way that an undesired, azimuthal component of the electric field appears in the detector. Its value depends on the position inside the 3^o sector and causes a distortion of 1% of the total field. The resulting effect is a focusing of the drifting charge toward the central anodes of the sectors (*central anode effect*) while the other two thirds of the anodes, those at the segments edges, receive a substantially smaller portion of the signal with a consequent worsening of the azimuthal resolution.

For the new generation of $3''$ detectors, during the manufacturing the front lithography mask was rotated by 1.5^o with respect to the back lithographies. The consequence is a better approximation of the radial drift field inside the depleted silicon and the symmetry is increased from a 120 to a 240 polygonal structure. The value of the azimuthal field component is decreased to 0.17% and the *central anode effect* is reduced.

The $4''$ detector has a completely new design which benefits from the progress in technology of the silicon drift detectors production which today allows the fabrication and the manufacture of bigger, very homogeneous wafers free of fatal defects. The maximum radius increases from 32 mm to 42 mm, the sensitive area of the chamber is enlarged from 32 cm^2 to 55 cm^2.

Besides the larger size and higher quality also the design has several new features:

- an improved approximation of ideal circles with polygons of 360 instead 120 sides;

- an increase of the designed drift field which allows an increase of the drift velocity of electrons from 6.5 to 10 $\mu m/s$;

- the introduction of injection pads at three different radii to measure the drift velocity of electrons with a simple voltage pulse;

- the development of an interlaced anode structure (Fig. 3.4) to improve the azimuthal resolution of the detector.

All these characteristics are extremely desirable in order to increase the performance of the detector. In particular, in CERES, the interlaced anode readout is very important because it significantly improves the measurement of the azimuthal coordinate of a track and therefore the momentum resolution of the spectrometer.

Since a spread of the signal over neighboring channels permits a better position determination, the new detectors have been designed to optimize the charge sharing. For signals generated close to the inner part of the wafer, the electron cloud is distributed over neighboring anodes by diffusion. To increase the number of responding anodes also for small drift times, the anodes are divided into several parts. In our case the optimal configuration is represented by the segmentation of a 1^o anode in five fractions: a large central part ($366 \mu m$ wide) which is bonded to the readout electronic and connected to the leftmost and rightmost part of the 1^o segment, two narrow ($61 \mu m$ wide) parts situated within the segment but connected to the neighboring anodes like in Fig. 3.4.

With this kind of interlaced anode structure, also signals with a small lateral spread are distributed over an higher number of readout channels.

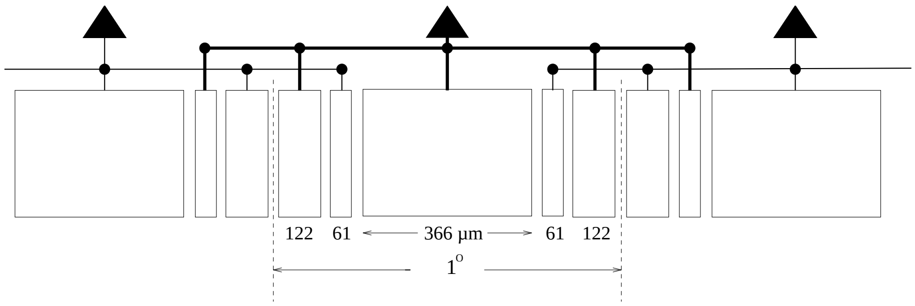

Figure 3.4: Schematic view of the interlaced anode structure of the 4″ detector.

3.3 The RICH Detectors

The basic concept of the RICH is that the Cherenkov light emitted by charged particles traversing a radiator of refraction index n, is reflected via a spherical mirror on ring in the focal plane where it is detected by position sensitive devices.

In CERES, the Cherenkov photons, produced in the RICH radiators and reflected by the mirrors, are registered in two UV-detectors which are separated from the radiator by a UV-transparent window (CaF_2 for RICH1 and Quartz for RICH2). They are placed upstream of the target and are, in this way, not traversed by the intense flux of forward going particles (Fig. 3.5). The UV-detectors [22] are gas counters (94% Helium, 6% Methane) in which the incoming photons are converted in electrons via photoionization of TMAE (Tetrakis-di-Methyl-Amino-Ethylen) vapor. To enhance the quantum efficiency of photon conversion, the vapor pressure is increased by heating TMAE to $42^o\ C$, consequently the detector is maintained to $50^o\ C$ to avoid TMAE condensation. In order to minimize the background and reduce the loss of momentum resolution due to multiple scattering, the amount of material within the acceptance is kept as low as possible [21]. The RICH1 mirror is based on a carbon fiber laminate shell of only $1mm$ thickness, whose radiation length is only 0.4%. The one of RICH2 is made of 10 glass segments 6 mm thick.

As radiator CH_4 at atmospheric pressure was chosen. It has the advantage of having a high Cherenkov threshold ($\gamma_{th} \simeq 32$), for which practically only electrons and positrons produce Cherenkov light. The spectrometer is thus insensible to more than 95 % of all charged hadrons (*hadron blind tracking*). Only the charged particles whose velocities satisfy:

$$\beta > \frac{1}{n} \ .$$

emit Cherenkov light in a cone of opening angle θ_c:

$$\theta_c = \arccos(\frac{1}{\beta n}) \ . \tag{3.1}$$

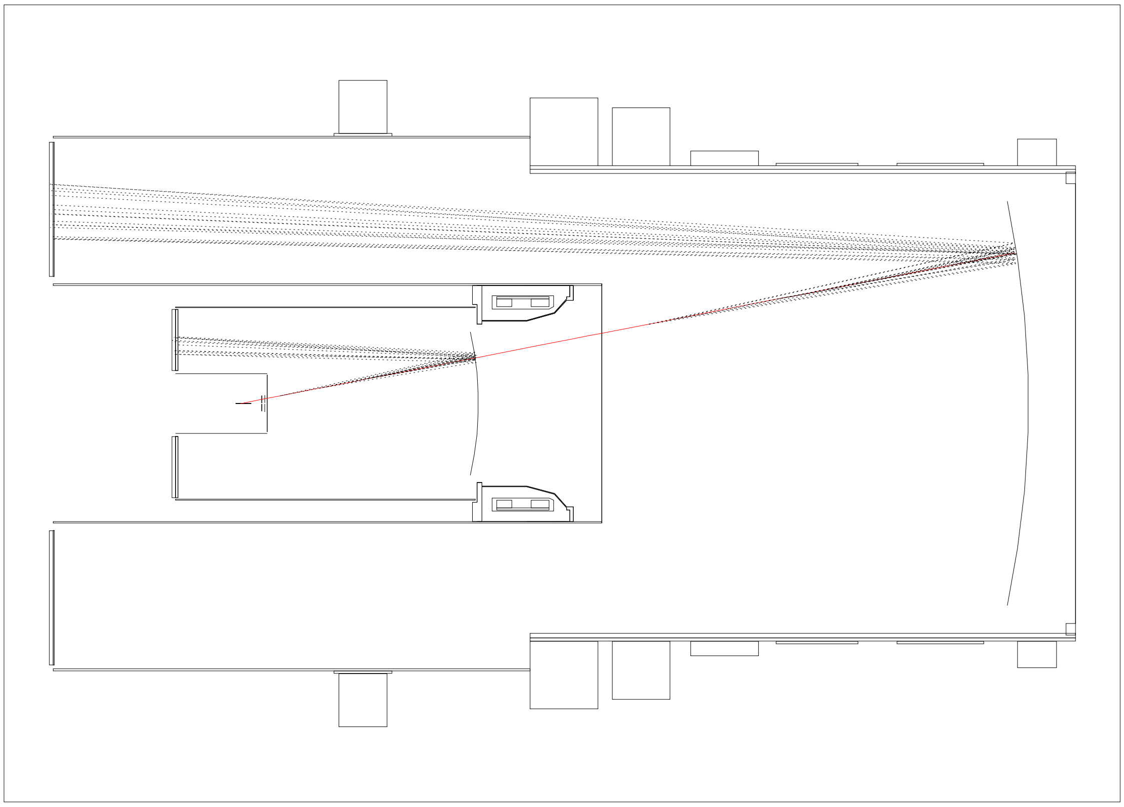

Figure 3.5: GEANT simulation of the signal produced from an electron traversing the CERES spectrometer.

For highly relativistic particles it is more common to use , instead of the velocity, the Lorenz factor, so that the relation for the threshold transforms to:

$$\gamma = (1 - \frac{1}{n^2})^{-1} \quad . \tag{3.2}$$

The photons emitted at a fixed angle are focused in a ring image by the mirror. The ring radius depends on γ as:

$$R = R_\infty \left[1 - \left(\frac{\gamma_{th}}{\gamma} \right)^2 \right]^{-\frac{1}{2}} \quad . \tag{3.3}$$

where the asymptotic radius R_∞ is 31.25 *mrad* $\approx$ 16 *pad units*[2]. The ring radius measures the particle velocity which can be used, knowing the momentum, to identify particles or knowing the particle mass, to calculate the momentum.

[2]Since the RICHes are characterized by a pad readout, often the ring radius is reported in pad units

Not only the radius but also the number of emitted photons on the ring depends on γ:

$$N = N_\infty \left[1 - \left(\frac{\gamma_{th}}{\gamma}\right)^2\right]. \tag{3.4}$$

The asymptotic number of reconstructed photons N_∞ is 11.2 for RICH1 and 9.5 for RICH2.

3.4 The Pad Chamber

The Pad Chamber, located after the mirrors of RICH2, behind the spectrometer, consists of a Multi Wire Proportional Chamber (MWPC) with pad readout. Its main role is to help the pattern recognition in RICH2 by providing the knowledge of the ring-center location and so reducing the number of fake-rings coming from the high background. Its angular coverage, between 7.8 and 15.1 degree, matches the full spectrometer acceptance and corresponds to the pseudorapidity interval $2.0 < \eta < 2.7$. More than 20000 channels constitute its readout. Each of them has a dimension of 7x7 mm^2, which allows a polar angle resolution better than 0.6 *mrad*. The granularity is such that the pile up probability remains below 10% for the highest multiplicity environment.

3.5 The Magnetic Field

A pair of super-conducting magnets produces, between the two RICH detectors, an azimuthal symmetric magnetic field for momentum measurement. Charged particles crossing this region are azimuthally deflected (between RICH1 and RICH2) by an angle $\Delta\phi$ equal to:

$$\Delta\phi = \frac{144 \text{ mrad}}{\text{p}} \text{ with p in GeV/c.} \tag{3.5}$$

By choosing opposite sign currents appropriately adjusted in the super-conducting coils, RICH1 is free of any magnetic field. In RICH2 the field lines are shaped by a set of correction coils to point back to the target. The field lines are schematically sketched in Fig. 3.1. In first order, the particles are only deflected in azimuthal direction and the polar angle of their trajectory is not affected. To second order approximation the polar direction of each track is slightly modified in direction of the beam axis (*second order field effect*) :

$$\Delta\theta = 78(\Delta\phi)^2 \frac{mrad}{rad^2} \tag{3.6}$$

Since the Pad Chamber samples a *point* on a particle trajectory, 2.5 *m* downstream of the field deflection, for the same momentum particle only a fraction of 65% of the total deflection is measured (see chapter 4).

3.6 The Trigger

The trigger system consists of three Beam Counters (BC1, BC2, BC3), a Veto (VC) and a Multiplicity detector (MD). The Beam Counters [23] are positioned 60 m upstream of the spectrometer (BC1), directly after the target (BC3) and beyond RICH2 (BC2). They are based on the Cherenkov effect. The Veto Counter and the Multiplicity Detector are made of standards plastic scintillators. The VC is $2m$ upstream of the target whereas the MD is located 5 m after the second mirror permitting a fast measure of the number of particles produced in the collision. A detected beam particle in BC1, none in BC2, BC3 and VC together with a measured multiplicity of 100 charged particle in MD, constitute a positive trigger decision which represents 35% [31] of the geometric cross-section.

Chapter 4

Tracking and Calibration

4.1 Reconstruction of Charged Particle Trajectories

The working principle of the important detector components of the CERES spectrometer has been explained in the previous chapter. Now the successive analysis steps are described. To illustrate the local hit density in the SDD and RICH detectors, we present an event display for one typical Pb-Au collision. Fig. 4.1 shows one event as it is measured by the two SDD detectors.

Each group of firing cells, which is defined as *cluster*, represents an ionisation center produced by a charged particle track. During the analysis, every *cluster* is inspected. It passes through a splitting procedure that tries to divide it into groups of smaller dimension, the so called *hits*. Each of these hits (apart from the ones that originate from electronic noise of the read-out chain) corresponds to a charged particle that has crossed the detector.

In the displayed event there are more than 300 hits in each of the two detectors. They correspond to the total number of charged particles emitted in 1.4 units of pseudorapidity covered by the SDD system.

Combining the information from SDD1 and SDD2, the Vertex, i.e. the point where the interaction has taken place, is reconstructed. With an assumed vertex position and a hit in SDD2, a point in SDD1 is predicted. The mean quadratic distance between this position and the hits in SDD1 within a restricted region is used as a χ^2 for a minimization procedure. By varying the assumed vertex position using the software MINUIT [24] the best fitting interaction point is determined. The vertex distribution for one run ($\approx$ 250000 events) is shown in Fig. 4.2. The resolution in z-direction is $200 - 300\ \mu m$ depending on the target position itself.

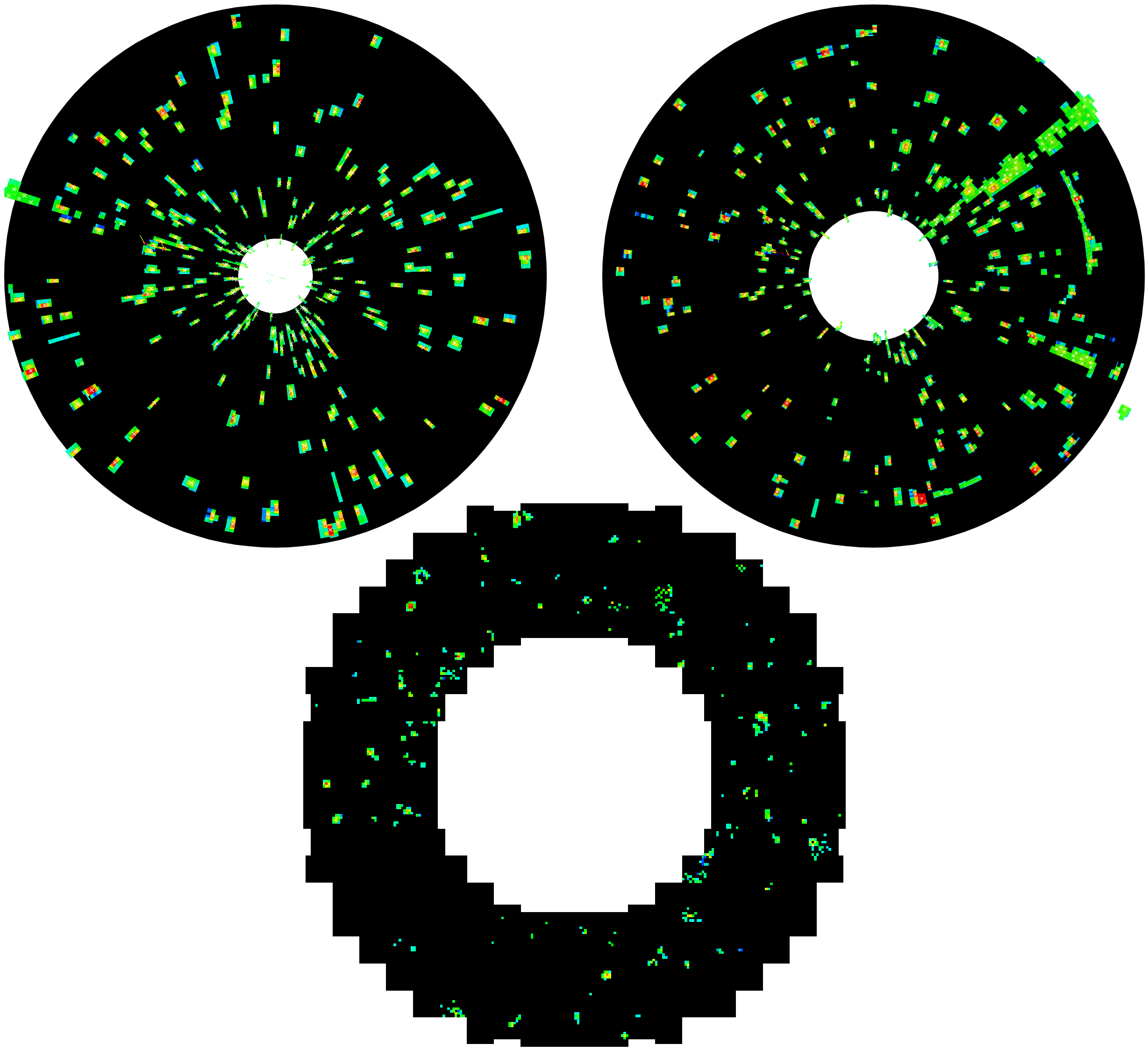

Figure 4.1: Event Display for SDD1 (left), SDD2 (right) and Pad Chamber (center).

Once the SDD track segments and the vertex are reconstructed, the trajectory of the charged particles is extrapolated into the Pad Chamber (Fig. 4.1 center). The polar angle remains unchanged, excepted for the second order field deflection (see chapter 3.5). In azimuthal direction a search area is defined by a lower momentum cut off. Depending on the momentum cut off, a different number of matching is found. Since the correct match is not known, all of them are considered as track candidates (see chapter 7). For each candidate a ring search is performed at the predicted position in the RICHes. Fig. 4.3 represents an example the RICH1 (left) and RICH2 (right) event display. On the right side of both pictures, two rings, overlapping in RICH1 and separated in RICH2, can be observed. This signature is typical for a e^+e^- pair originating from a π^0 Dalitz decay or a γ conversion. The

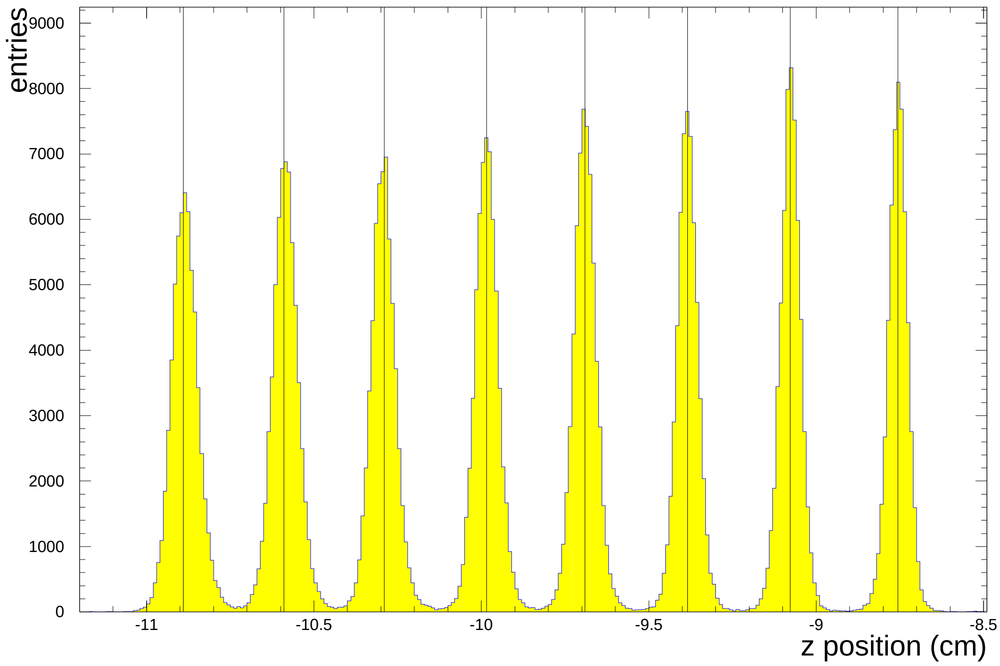

Figure 4.2: Reconstructed vertex position. The vertical line represents, for comparison, the real width of a target discs.

marked ring of photons on the left side is instead assigned, because of its smaller ring radius, to belong to a track of a charged pion.

4.2 Particle Identification

The CERES spectrometer allows the detection of charged pions which are fast enough to produce Cherenkov light. Due to the high gamma threshold only pions that have at least a momentum of 4.5 GeV/c are visible in the RICHes. They generate a ring with a variable radius, correlated to the momentum according to the relation:

$$R = R_\infty \sqrt{1 - \left(\frac{m\gamma_{th}}{p}\right)^2} \quad . \tag{4.1}$$

Pions can be distinguished from electrons by the ring radius. For electrons p/m is large thus they generate ring of asymptotic radius R_∞ whereas the pions reach R_∞ only for very high momenta $15 - 20$ GeV/c.

The background generated by other particles is negligible, kaons for example will produce Cherenkov light only if they have a momentum larger than 16 GeV/c.

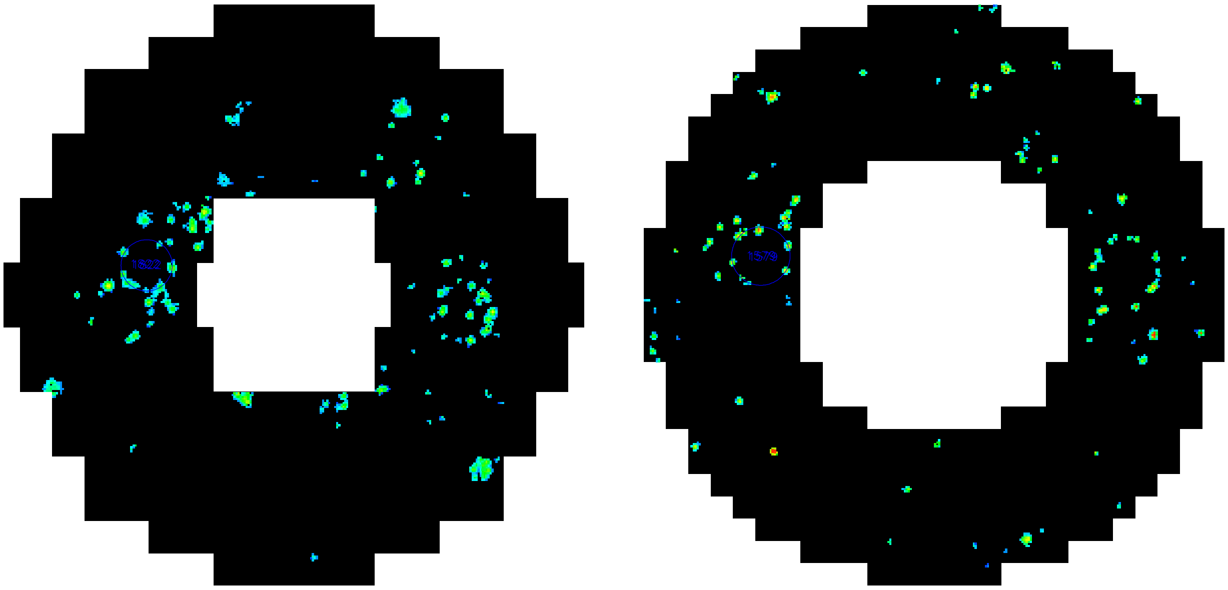

Figure 4.3: Event Display for RICH1 (left) and RICH2 (right).

4.2.1 Electron Identification

Before CERES was supplemented with external tracking devices the rings in the two RICH detectors had to be reconstructed without knowing a priori the ring centers. A solution to it was found by application of a point to ring Hough-Transformation (HT)[25]. Around every photon hit detected in the RICHes, a circle with a particular radius R_c is drawn and the produced circles are summed. Circles around points that lie on a ring of radius R_c, will join in the ring center, producing a maximum of the amplitude in the ring plane. For electrons the radius can be fixed to R_∞ and the algorithm works excellently.

For pions the situation is not as easy because their ring radii are not known. In principle, it is possible to use a discrete number of different radii for the HT but it is always necessary to compromise between the required computing time and the reconstruction efficiency. In fact, choosing an insufficient granularity in radius for the HT will produce a minimum in the ring reconstruction efficiency where the pion ring will not be recognized [26]. For this reason, and in order to profit from the upgraded and more complete experimental setup, a different approach was developed.

4.2.2 Pion Identification

The pion identification makes full use of the external tracking detectors, SDD and Pad Chamber, to predict the ring center positions in the RICHes.

The method is straight forward in the case of high momentum pions (p > 4.5 GeV/c). The information from vertex and SDD track segments are used to point into the Pad Chamber. For each track segment in the SDD system before the magnetic field, a matching hit in the Pad Chamber after the field is searched. Taking into account that the pions of interest have more than 4.5 GeV/c momentum and the deflection in the magnetic field is about 144 mrad/GeV/c, the search region is limited to ± 30 mrad in azimuthal direction. The polar angle stays constant and will be altered neither by the magnetic field, nor by multiple scattering which can be neglected for such high momentum particles. Therefore the search in polar direction is limited to an interval which depends only on the match quality between the two detectors.

All hits in the Pad Chamber, connected with the track segment in the silicon, are considered as pion candidates. With the knowledge of the candidate coordinates before and after the field, the position of ring centers in the RICH detectors can be predicted. For RICH1 the zone to be analyzed is restricted to the region around the point given by the extrapolation of the silicon track. Making use of the momentum information derived from the azimuthal deflection between SDD and Pad Chamber the tracks are extrapolated into RICH2, behind the field.

The photon hits that fall within an area around this predictors are collected and used as input for a fit procedure which aims to find the center and radius of the ring. To do so we minimize the function

$$\Psi\left(x_0, y_0, r_0\right) = -\frac{1}{N-3}\sum_{i=1}^{N} exp\left[\frac{\left(\sqrt{(x_i - x_0)^2 + (y_i - y_0)^2} - r_0\right)^2}{2\sigma_f^2}\right] \tag{4.2}$$

where the x_0, y_0 are the coordinates of the ring center, r_0 the correspondent ring radius, σ_{f} the sigma of the distribution of photon hits on the ring and x_i, y_i the coordinates of the $i - th$ of the N hits. The function represents a Gaussian-fit potential which has the advantage that hits far from the ring have a lower weight and therefore do not contribute (*robust fitting algorithm* [28]).

From this method a *candidate* track is obtained, which must still pass different quality cuts necessary to suppress the *fake* track background, i.e. purely random combinations of hits and rings.

4.3 Spectrometer Calibration

For the analysis of the 1995 data, every spectrometer component was carefully calibrated. The alignment of all detectors and the derivation of appropriate correction functions for the analysis chain were achieved in different, successive steps.

Firstly a rough calibration was performed which aimed to adjust the detector offset in X,Y and Z direction and to correct for eventual rotations. The center of SDD1 was chosen as origin of our reference system. The method of this calibration has been worked out in previous theses, a detailed explanation can be found in [1].

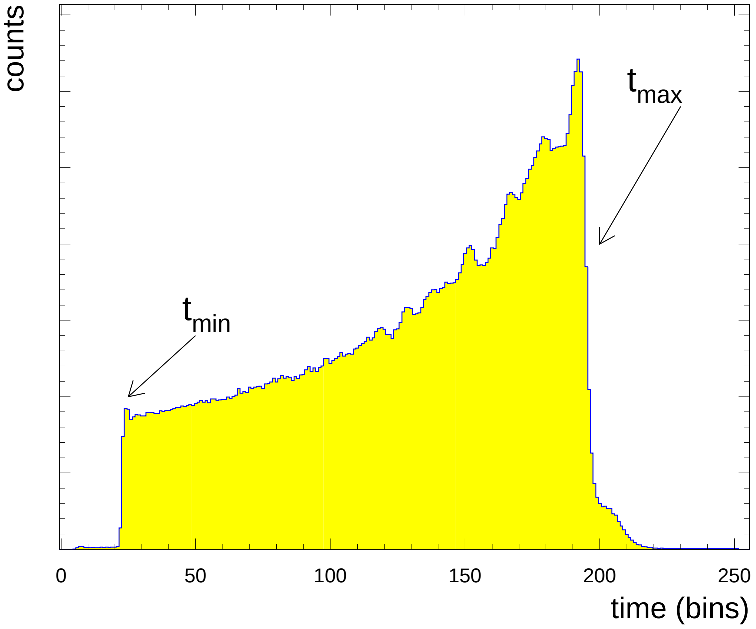

Figure 4.4: Hit distribution in SDD2: one time bin corresponds to 20 ns.

4.3.1 SDD Calibration

The SDD detectors needed specific calibrations. First the time information needs to be converted into a drift distance. To first order the time-distance relation is linear and therefore the drift velocity can be calculated knowing the radial extension $\Delta R = R_{max} - R_{min}$ of active area of the SDD and the total drift time $\Delta t = t_{max} - t_{min}$ as: $v_d = \Delta R / \Delta t$. The radial position is given by:

$$r = R_{max} - v_d \cdot (t - t_{min}) \tag{4.3}$$

where R_{max} is the anode position and t_{min} corresponds to hits that fall directly on anodes and consequently do not drift (t_{min} is not zero because of trigger delays). Fig. 4.4 shows a typical drift time distribution for the second SDD detector.

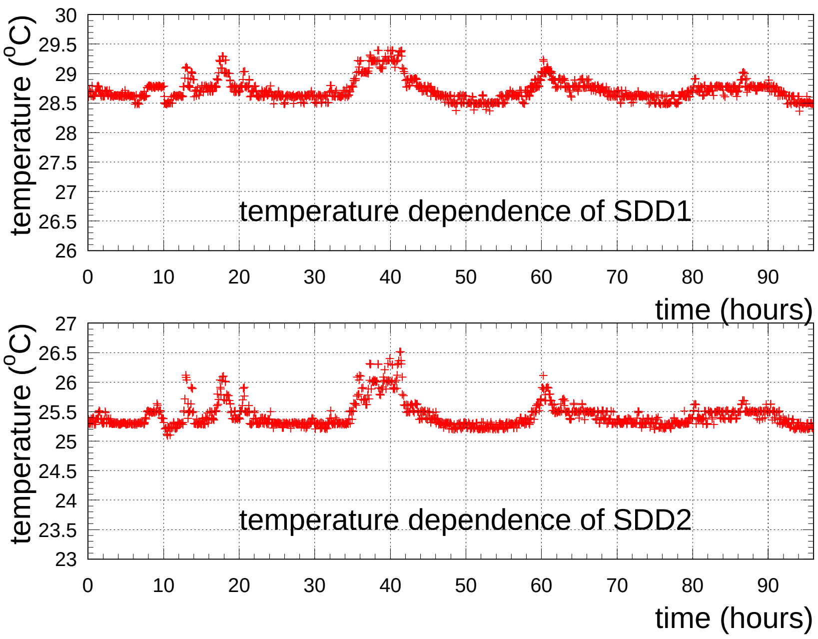

Figure 4.5: Temperature variation of the zone surrounding the silicon detectors. As it can be seen the variations in the two detectors are very good correlated even if the absolute value of the temperature differs by 3°K

Since the electron mobility depends on temperature with $\mu \propto T^{-2.4}$, the drift velocity strongly suffers from temperature variations. In the spectrometer and in particular in the region surrounding the SDD system, even though the cooling was continuously running during the data taking, changes in temperature of the order of $1^o\ K$ are actually observed (Fig. 4.5). At $300^o\ K$ a variation of $1^o\ K$ will produce around 1% change in the drift velocity which corresponds to a maximum of 300 μm mismatch for full drift time.

To study the effect of temperature changes, the cooling was switched off for a certain time. The consequence was that, fixing the calibration, the change of the drift velocity results in an unphysical movement of the z-coordinate of the vertex (Fig. 4.6 left). An automatic calibration method that uses the upper edge of the drift time distribution was developed (compare Fig. 4.4). This procedure is justified because the active area of the SDD does not change and the lower-time edge remains constant (hits that are very close to the anodes have negligible drift time). The right hand side of Fig. 4.6 shows that using the time-edge calibration method the vertex z-coordinate remains constant.

A further, more detailed and local run to run calibration of the SDD telescope was performed using a high statistical pion sample available after the first data production. Very strong quality cuts were applied to each pion track. A high number of photons on rings, a small number of hits in the region around the fitted circle, a tight radius to radius and radius to deflection correlation allow to separate a true track from a false one. Only those tracks which survived these requirements,

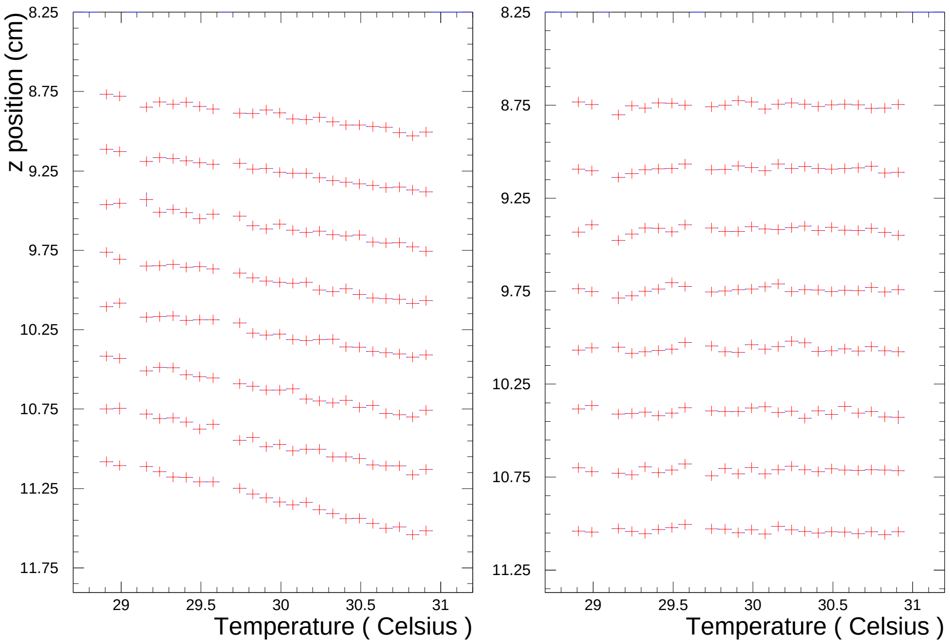

Figure 4.6: Temperature dependence of the reconstructed z-position of the eight target discs before (left) and after (right) drift velocity calibration.

were used in the next step.

The more precise calibration of the SDD system was obtained making use of the Pad Chamber. The idea is based on the interpolation between the vertex coordinates and the position of the hit in the Pad Chamber into the SDD detectors. Fig. 4.7 shows the distance between the extrapolated point and the SDD hit as function of the radial hit position on the SDD detector for one run. The slope of the full points on the left figure can be reduced to zero by tuning the drift velocity (open symbols) and the remaining offset can be minimized changing the minimum drift time (square points on the right hand side).

The difference between this new value for the *minimum drift time* and the one that corresponds to particles falling on anodes can be explained in the following way. Since this method calibrates only the part of the SDD detectors which is covered by the Pad Chamber acceptance, a distortion of the drift field over a limited region of the wafer will lead to a drift velocity value different from the one obtained with the linear assumption. The extrapolation to the maximum radius will then result in this effective minimum drift time. Fig. 4.8 presents the time variations of the calibrated drift velocities (plots 1-2). The method is very powerful and permits to calibrate the drift velocity at a level of 0.2%. The variations can be also compared to Fig. 4.5 which represents the temperature oscillations measured in the region surrounding the silicon system. As already mentioned, the drift velocity decreases with increasing temperature. The correlation between the calibrated values for SDD1 and SDD2, both suffering from the same temperature variations are shown in plots 3-4 of Fig. 4.8. Profiting from the high pion statistics, also a

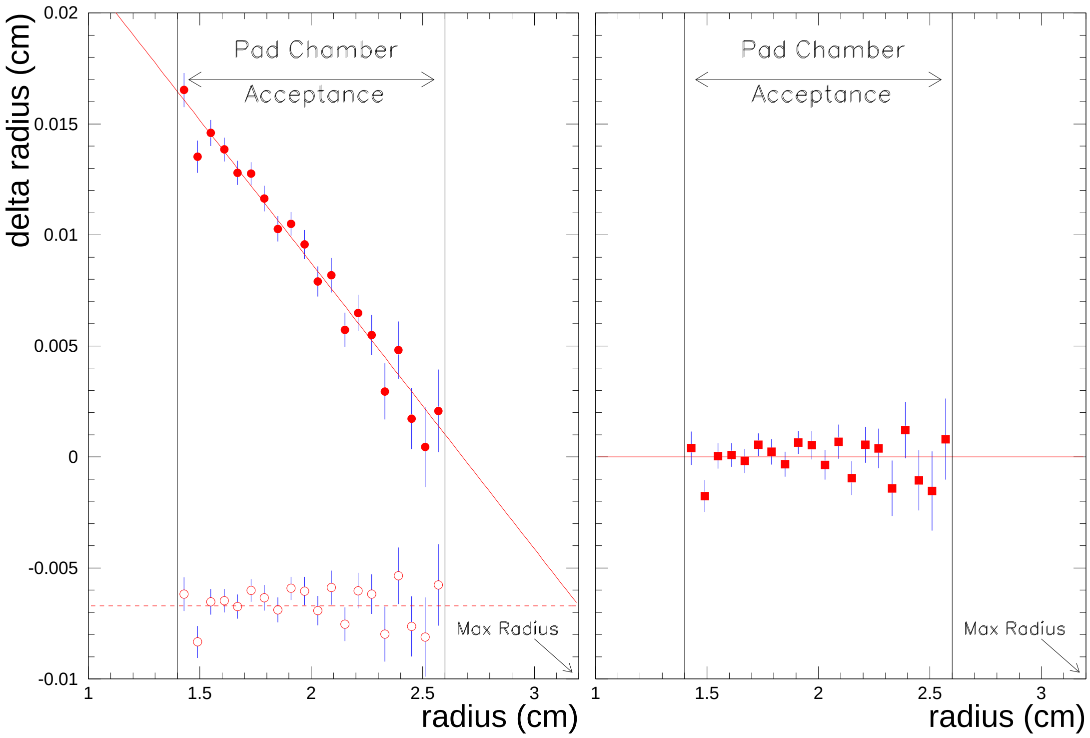

Figure 4.7: Calibration of SDD1 obtained with the Pad Chamber. Three different steps are presented: the situation before the calibration (•), after tuning of the drift velocity (◦) and final minimum drift time setting (right plot) .

detailed examination of small domains was possible. Anode to anode time-shifts were introduced and local corrections of the drift velocities were obtained over the range covered by the Pad Chamber acceptance.

4.3.2 RICH Calibration

In the past, the two RICHes were used to fix the coordinate scale to which all others detectors had to be matched. In the new calibration procedure, it was decided to give the priority to the detector which had the better resolution and was easier to understand: the Pad Chamber, for which in principle all pad positions are perfectly known. Studying in more detail the two RICH detectors using the Pad Chamber as a reference scale, it was found that slight deformations of the spherical mirrors (one segment in RICH1 and ten in RICH2) caused a non-linearity in the determination of the polar angle (Fig. 4.9, (•)). To first order, a constant variation of the focal length of the mirrors will produce only a change in the offset value of those points with consequent necessity to shift the Pad Chamber toward a position which is not allowed by the accuracy of the measured distance. The solution to

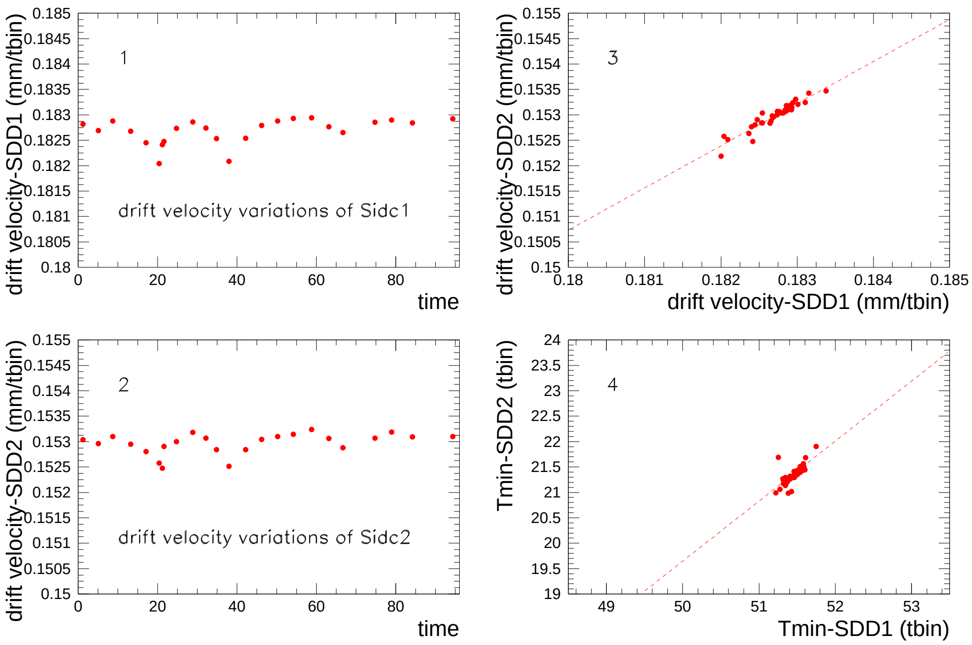

Figure 4.8: Calibration values of the SDD system obtained with the pion sample. Plots 1 and 2 represent the calibration values of the *drift velocity* as function of time. Plots 3 and 4 show the correlation between the values obtained for the *drift velocity* and *minimum drift time* for the two SDD detectors.

the problem is the introduction of a focal length which depends on the polar angle [2]. With this correction an improvement in the match with the Pad Chamber (Fig. 4.9 (∘)) is observed.

4.4 Momentum Measurement

The CERES spectrometer allows to determine momenta with two completely different methods:

- via the azimuthal deflection in the magnetic field (see chapter 7)
- via the radius of the Cherenkov rings in the RICHes (see chapter 8)

Fig. 4.10 shows the correlation between those two measurements.

4.4.1 Azimuthal Deflection

Due to the particular magnetic field configuration of CERES, the curvature of a charged particle trajectory is essentially equivalent to a *kick* in the azimuthal ϕ direction. The kick is inversely proportional to the particle momentum.

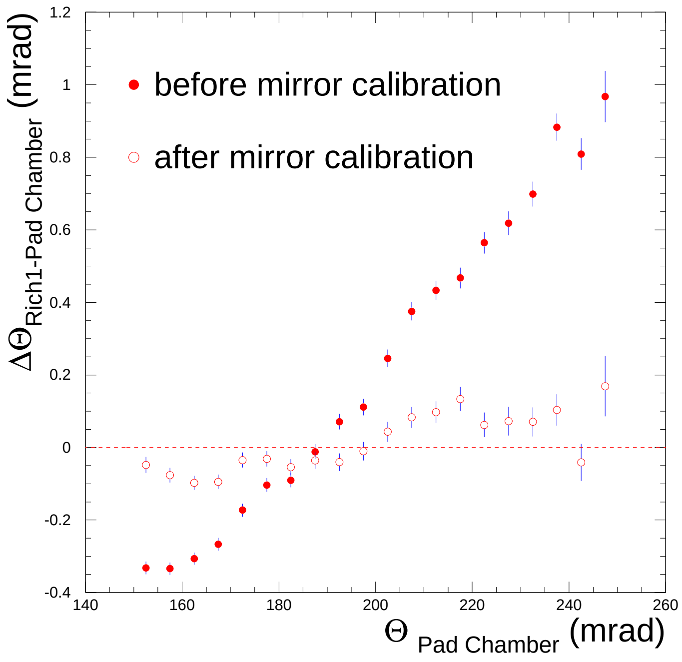

Figure 4.9: Calibration of the mirror of RICH1 using the Pad Chamber as a reference system.

In order to optimize the momentum resolution, the information from all five detectors is used to evaluate the deflection angle $\Delta\phi$. The measured azimuthal ϕ position of a track in every detector is plotted as a function of the expected relative deflection X in the magnetic field in Fig.4.11a.

SDD1, SDD2 and RICH1 are field free and X is zero. RICH2 measures the total deflection and X is set to 100. The Pad Chamber samples a point on a track 2.5 m downstream of the field kick, this corresponds to 65% of the value measured by RICH2 therefore $X = 65$ (Fig.4.11b).

Fig. 4.12 shows the correlation between the ring radius and the azimuthal deflection (like Fig. 4.10) obtained using different detector combinations. If one chooses a small ring radius interval ΔR which corresponds to a small momentum interval Δp, the width (or standard deviation) of the resulting $\Delta\phi$ distribution (Fig. 4.13) is a measurement of the azimuthal resolution of the system for the chosen momentum interval Δp.

Plots 1 in Figs. 4.12 and 4.13 reflect the situation where only RICH1 and RICH2 are used to calculate $\Delta\phi$. The two *bands* representing the positive and negative pions are strongly overlapping. If RICH1 is replaced by the SDD, the two charges are clearly separated (plots 2). In the plots 3, the Pad Chamber-SDD match is shown. Note that the relative resolution in ϕ is comparable to the measurement of RICH2 and SDD because the better angular resolution of the Pad Chamber is compensated by the smaller angular deflection measured.

The best result, displayed in plots 4, is obtained combining all measurements

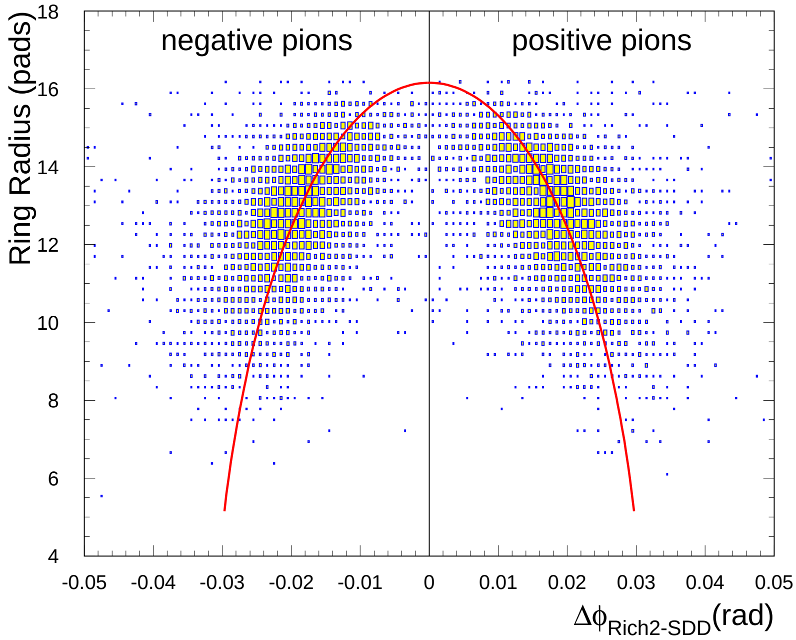

Figure 4.10: Correlation between the ring radius and the deflection in the magnetic field.

with appropriate weights. The weight function takes into account the momentum dependent multiple scattering term and the individual detector resolution σ_ϕ:

$$\frac{1}{\mathrm{weigth}} = \sqrt{(\frac{\sigma_{\mathrm{multipleScattering}}}{\mathrm{p}})^2 + \sigma_\phi^2} \ .$$

Table 4.1 shows the factors introduced in the weight function.

	$\sigma_{\mathrm{MultipleScattering}}$ $(mrad \cdot GeV/c)$	$\sigma_{\Delta\phi}$ (mrad)
SDDs	6.44	4.0
Rich1	4.42	7.0
Rich2	2.91	3.4
PadChamber	1.68	1.8

Table 4.1: Azimuthal detector resolutions and multiple scattering terms of the spectrometer.

4.4.2 Cherenkov Ring Radius

For the charged particles which exceed the threshold and produce Cherenkov light in RICH1 and RICH2, the momentum can be calculated from the radius of

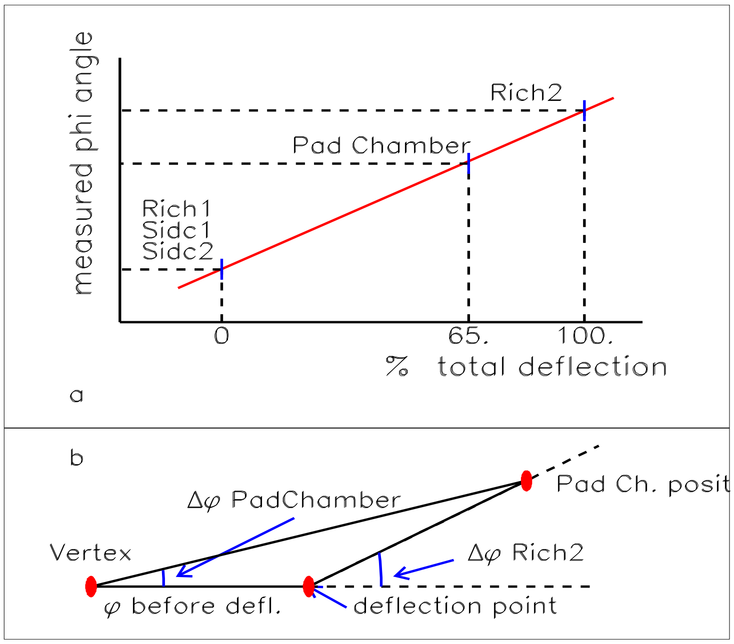

Figure 4.11: To calculate the best $\Delta\phi$, every detector is assigned a weight according to its sensitivity in a two two dimensional plot (a). RICH2 and Pad Chamber measure a different fraction of the deflection angle $\Delta\phi$ (b).

the reconstructed ring, using equation 4.2:

$$\mathrm{p} = \frac{\mathrm{m}\gamma_{\mathrm{th}}}{\sqrt{1-(\frac{\mathrm{R}}{\mathrm{R}_\infty})^2}} \tag{4.4}$$

where m is the mass of the particle. The ring radius increases with increasing momentum. In the limit of very energetic particles, the asymptotic ring radius is reached and the calculation of the momentum is no longer possible.

4.4.3 Momentum Resolution

The following section presents the estimation of the momentum resolution reached using the ϕ deflection or the ring radius. If the momentum is calculated from the ϕ deflection the relative error on the momentum, i.e. the momentum resolution, is given by:

$$\frac{\sigma_{\mathrm{p}}}{\mathrm{p}} = \frac{\sigma_{\Delta\phi}}{\Delta\phi} = 4\% \cdot \mathrm{p} \quad . \tag{4.5}$$

From the ring radius measurement one can derive the momentum resolution:

$$\frac{\sigma_{\mathrm{p}}}{\mathrm{p}} = \frac{\mathrm{R}}{\mathrm{R}_\infty^2 - \mathrm{R}^2}\sigma_{\mathrm{R}} < 0.1\% \cdot \mathrm{p}^2 \quad . \tag{4.6}$$

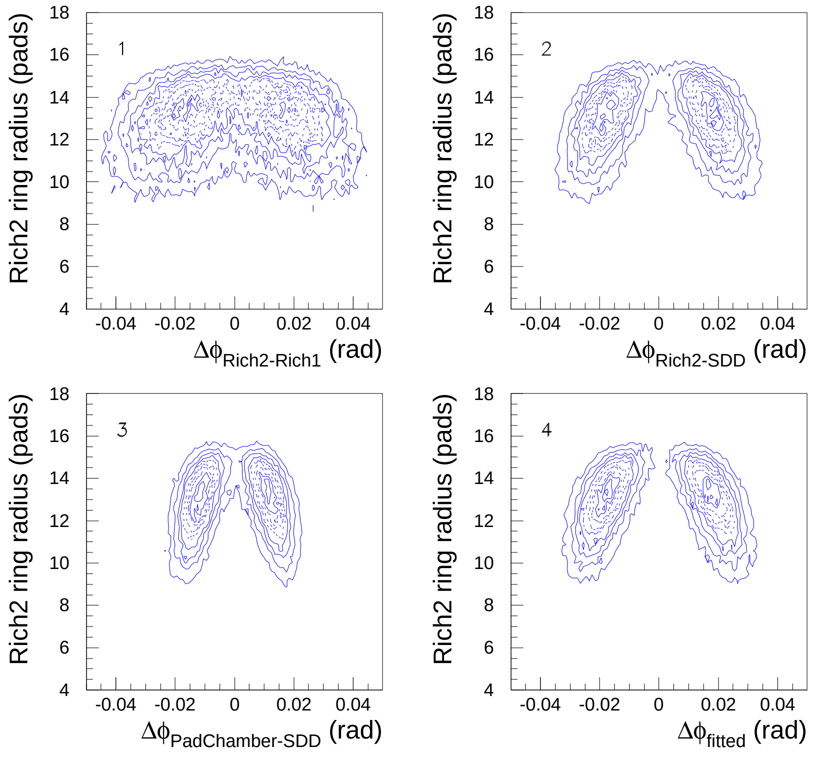

Figure 4.12: Radius-deflection correlation obtained using different detector combinations.

where the σ_{R} is the ring radius resolution. In absence of background, σ_{R} depends on the number N of hits on the ring and on the single hit resolution σ_{sh} in the following way:

$$\sigma_{\mathrm{R}} = \frac{\pi}{2}\frac{\sigma_{\mathrm{sh}}}{\sqrt{\mathrm{N}-\mathrm{N}_{\mathrm{dof}}}} \quad . \tag{4.7}$$

where $\mathrm{N}_{\mathrm{dof}}$ is the number of degrees of freedom, which in this case are three: the x, y position of the ring center and the ring radius R. In practice, the background hits dilute the $1/\sqrt{N}$ dependence. This effect can be reproduced in the Monte-Carlo simulation (see Fig. 5.6).

In fig. 4.14 the momentum resolutions corresponding to the different methods are shown. One can notice that the best individual momentum measurement is given by RICH2 ring radius. The deflection method becomes competitive only in the case of very high momenta (p > 40 GeV/c) where the two functions intersect. RICH1 presents the same quadratic dependence as RICH2. Its steeper rise is due to the worse radius resolution, caused by the much higher background contamination in comparison to RICH2. Consequently the RICH2 ring radius is chosen as measure of the momentum of the identified pions.

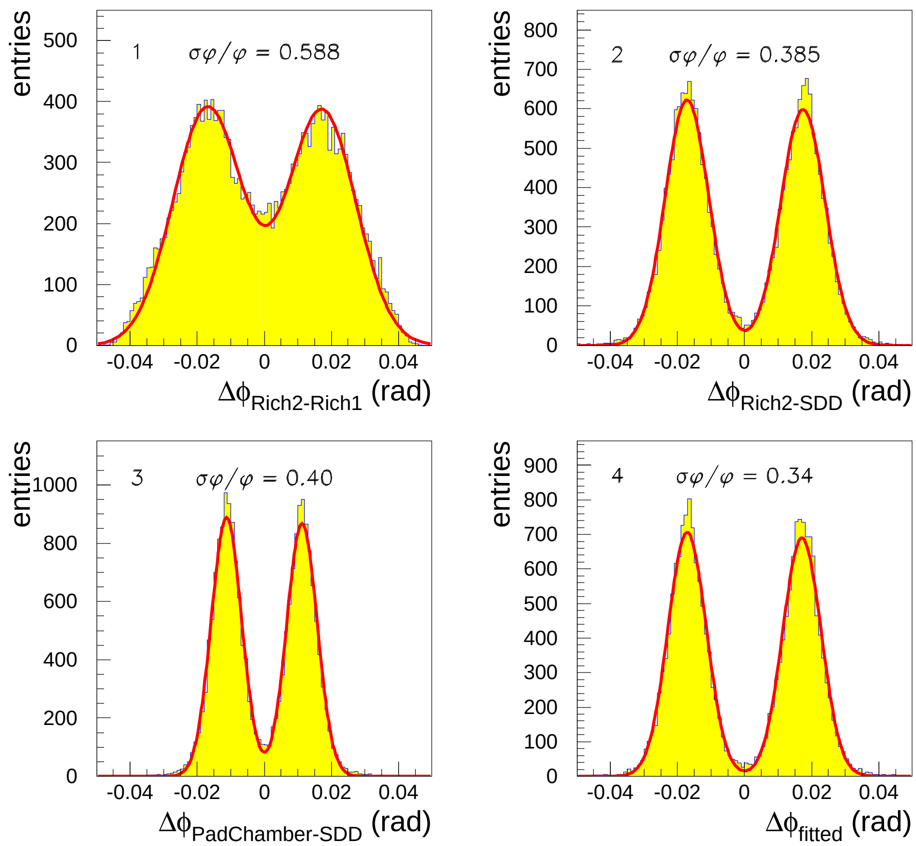

Figure 4.13: $\Delta\phi$ resolutions for the different detectors combinations obtained choosing a particular radius interval (13. $\leq$ ring radius in Rich2 $\leq$ 14.pads) which corresponds to a momentum of about 8 GeV/c.

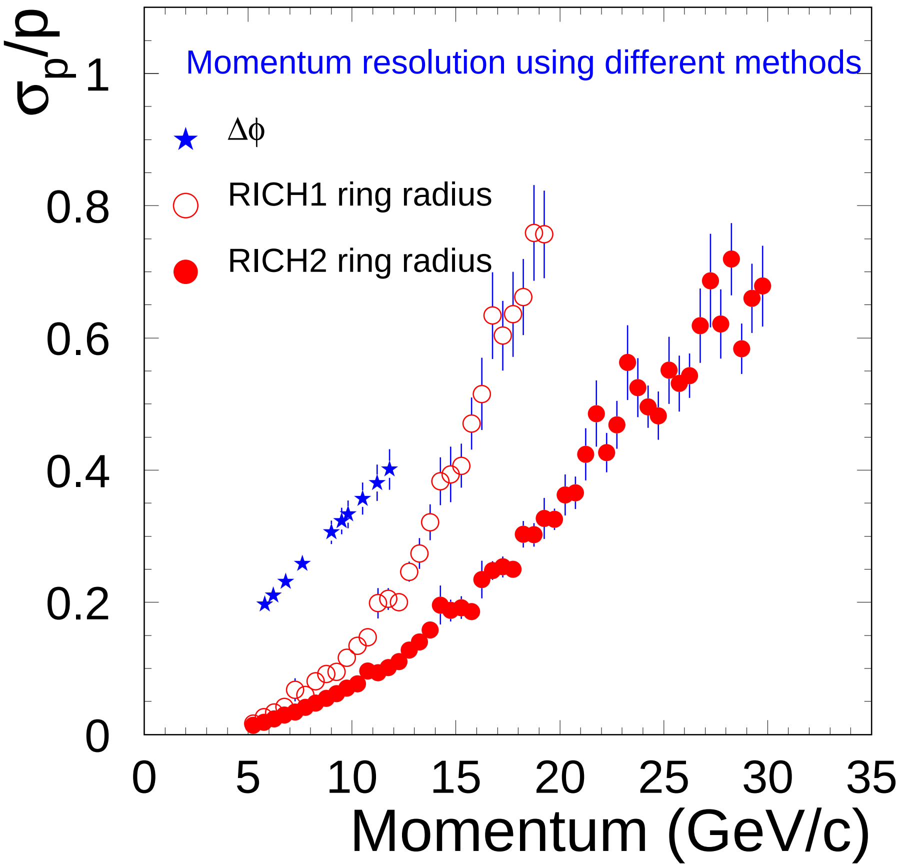

Figure 4.14: Momentum resolution obtained with different methods: ring radius and azimuthal deflection.

Chapter 5

Monte-Carlo Simulation

5.1 Overview

Due to the fact that each detector is characterized by a certain efficiency and has a restricted geometric and kinematic acceptance as well as a limited resolution, the measured data do not directly reflect the property and peculiarity of the 'true' physics. The data, affected by these detector 'defects', could at the same time be influenced by the problems an analysis program can have: inefficiency of the hit reconstruction and limitation of the track finding algorithm. Since an analytic calculation that corrects for all those effects is too complicated, the corrections are usually obtained with the help of a Monte-Carlo simulation. The technique determines the influence of the detector 'defects' and of the software analysis on a known sample which constitutes the *input* of the Monte-Carlo. The correction functions are obtained comparing the input and output distributions, which are the result of the processing through the full analysis chain.

The detailed description of all relevant parts constituting the experiment is based on a software package called GEANT [27]. The package allows to define the geometry and material quality of every detector in an easy and flexible way. Once the experimental setup has been fixed, the program calculates the path of the produced particles through the detectors. The trajectory of a particle will be modified by multiple scattering, hadronic interactions, deflection in a magnetic field and decay of unstable particles.

If a sensitive part of the spectrometer is crossed, all the necessary information for the simulation of the detector response is stored. In the successive step detector signals are generated with a structure which is identical to the one of the measured data. This allows to study the Monte-Carlo results with the same analysis program used to process the real data.

5.2 Detector Responses

The accurate description of every detector response is of prime importance and interest to extract the correction functions later on used to derive the final results. Several quantities need to be checked and tuned in such a way that the Monte-Carlo simulation agrees with the measured data. Starting from the hit description, one has to investigate the general characteristic of the signal generated from particles crossing the spectrometer. The following step controls whether the matching distributions between the different detectors are well reproduced. Finally it is necessary to verify that all the quantities correlated with the physics signal one wants to measure are properly simulated.

5.2.1 Hit Description

The following section will present some examples of how the signals have been simulated for the SDD system. Charged particles that cross the SDD detector deposit a certain amount of charge. These values, furnished directly by GEANT, follow the Bethe-Bloch [29] equation which describes the average rate of energy loss of a particle traversing a material. Since the total signal amplitude depends also on the gain of the electronics, this quantity was adjusted such that the mean amplitude produced by one particle (Minimum Ionizing Particle MIP) is well reproduced. The Monte-Carlo contains also a realistic description of the dead regions of the detectors and of the noise generated by the electronics. The zones of low gain are usually implemented with the introduction of a gain map.

Fig. 5.1 shows the amplitude distribution of the hits in the two SDDs. As one can observe, there is a good agreement between the Monte-Carlo distribution, represented by the histogram, and the data, shown as crosses. The difference of the maximum amplitude, 350 for SDD1 and 600 for SDD2 is due to the different gain setting chosen for the two chambers.

Another characteristic is the distribution of the number of anodes which contribute to a hit (Fig. 5.2). This is perhaps one of the most important features because the azimuthal resolution of the SDD telescope depends strongly on the number of anodes corresponding to a hit. From the figure, one can observe that most of the hits are composed by 1-2 anodes and only a small fraction (5%) of the particles distribute their charge over more than two.

Fig. 5.3 shows the distribution of the width (RMS) of the hit in azimuthal ϕ and radial r direction. The peak at zero of the σ_ϕ distribution (left side) corresponds to the hits composed only of one anode. The right plot shows that the mean radial width of a SDD hit is around 300 μm. The tail at higher σ_r values is produced by the so called *double hits* which consist of two hits whose distance is so small that they cannot be divided by the hit reconstruction algorithm.

In a similar way, all the general hit characteristics of the other detectors have been checked and they were found to be in good agreement with the real data.

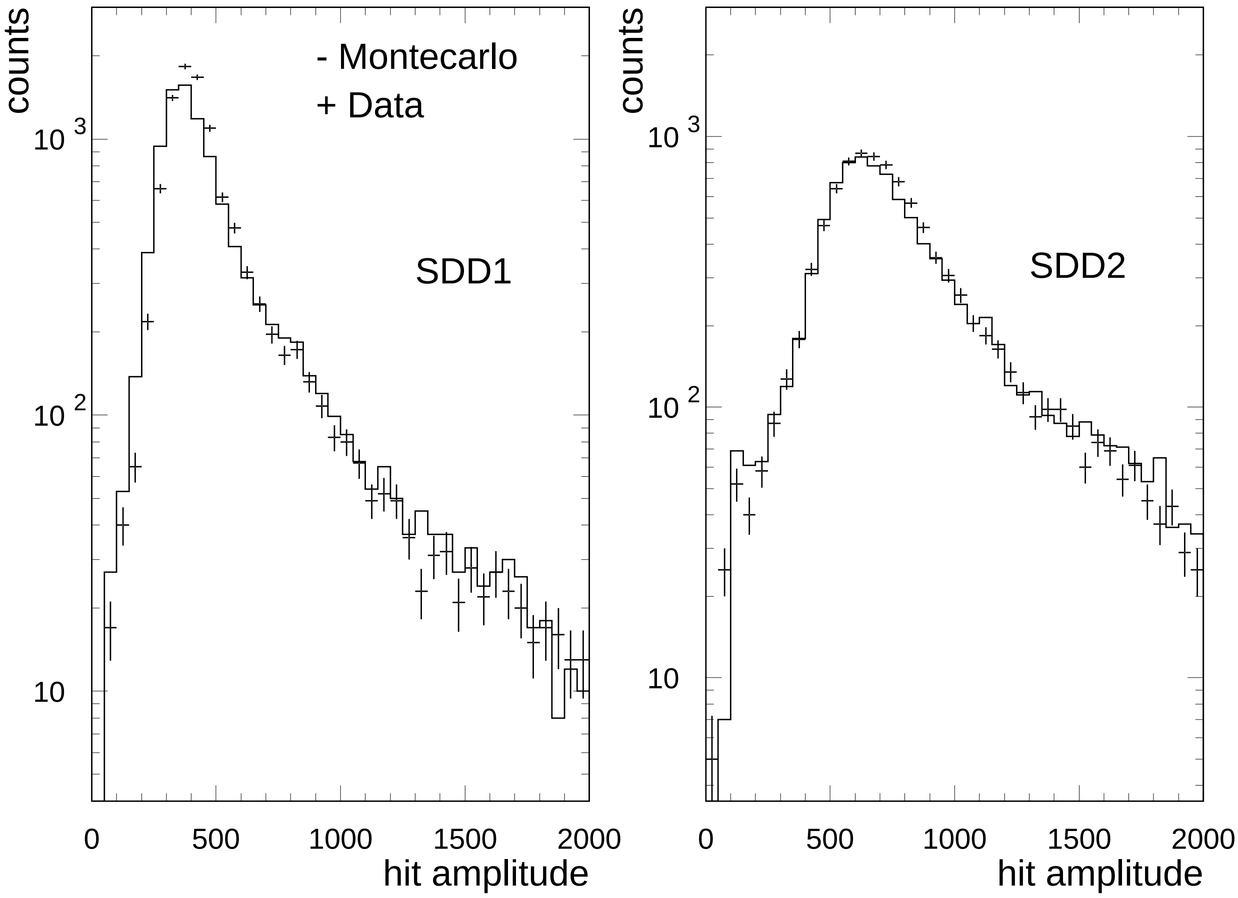

Figure 5.1: Amplitude distribution of the SDD hits.

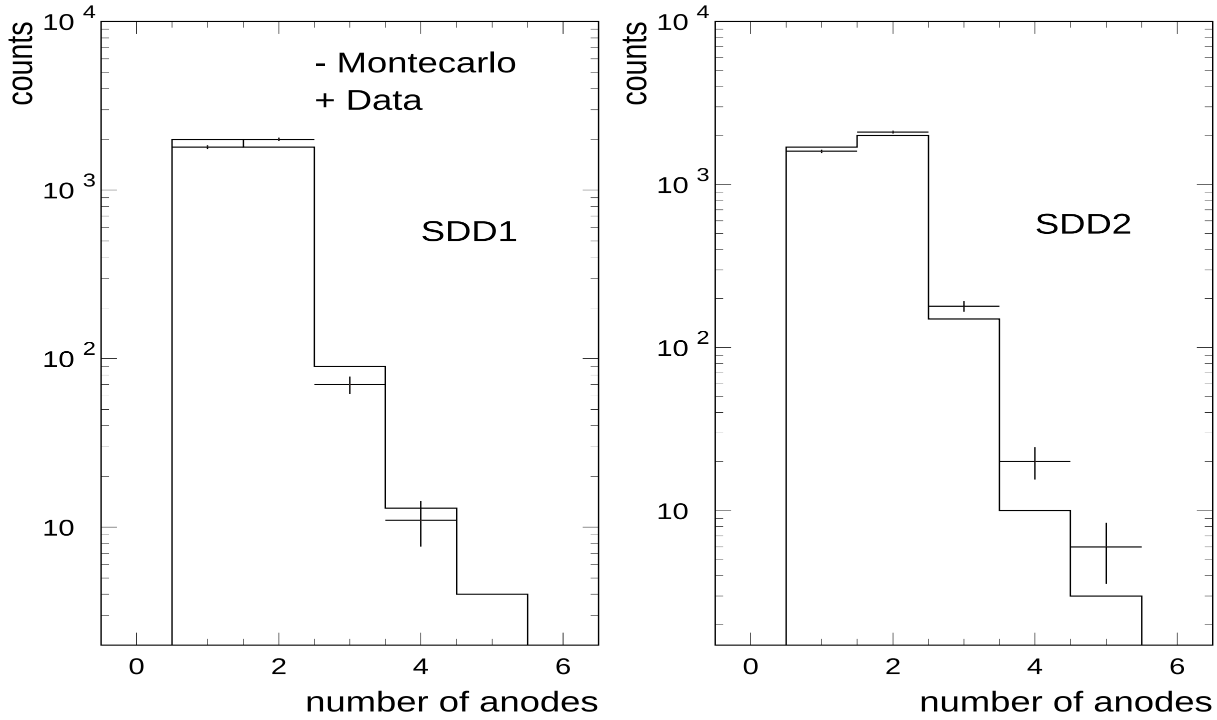

Figure 5.2: Distribution of the number of anodes composing a hit in SDD1 and SDD2.

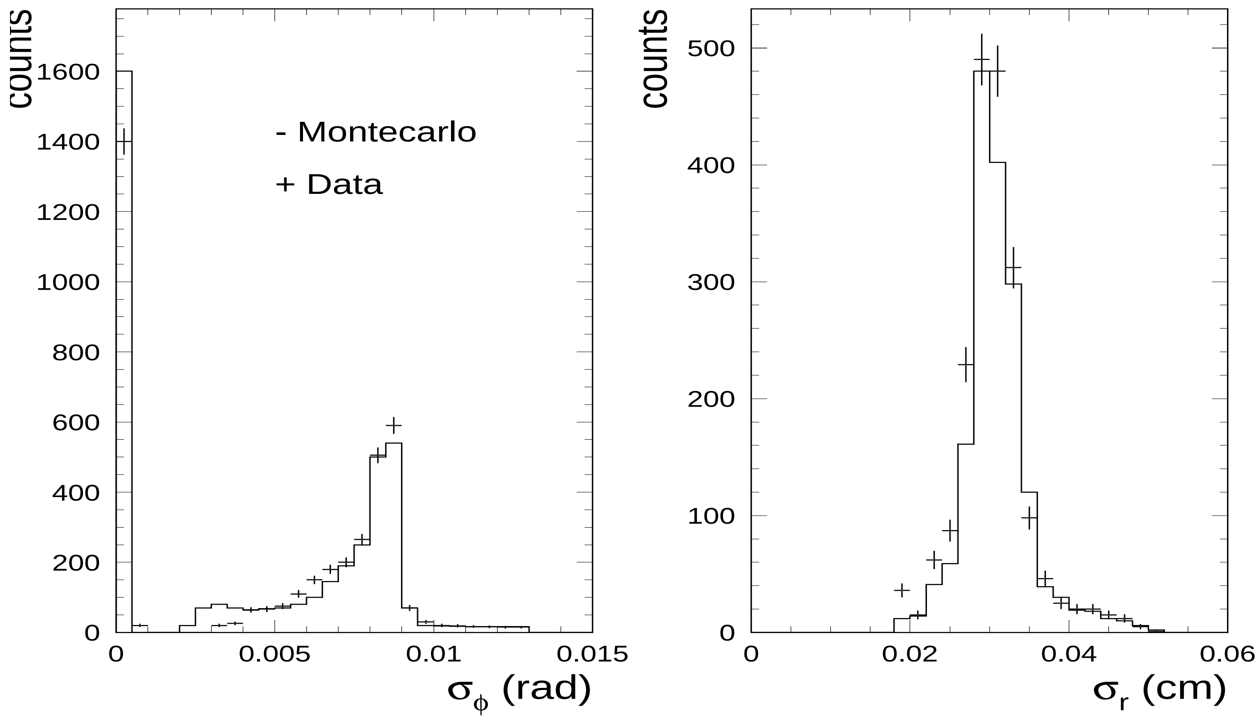

Figure 5.3: Distribution of the hit RMS in ϕ and r direction for the two SDD.

5.2.2 Matching Description

The next step of the simulation analysis was to check the matching distributions between the detectors composing the spectrometer. Some examples, particularly concerning the match in polar angle θ measured by different detector combinations, are presented in Fig. 5.4.

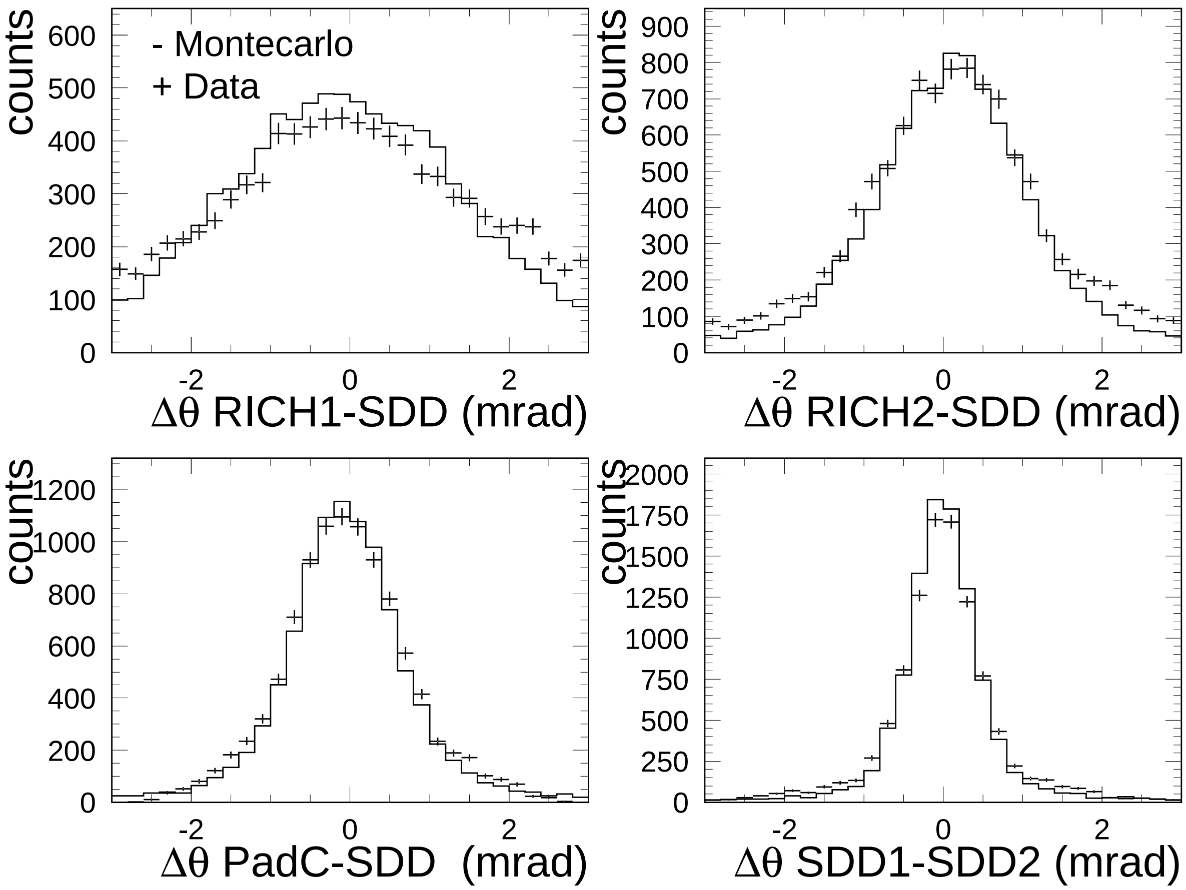

Figure 5.4: θ angle matching distribution for different detector components.

As one can notice, Pad Chamber-SDD and SDD1-SDD2 matches are well described by the Monte-Carlo. In the case of the two RICH detectors the two distributions do not completely coincide: the data seem to have a wider distribution in comparison to the simulation. A possible explanation could come from the fact that the data (crosses) are a superposition of two components: a physical one consisting of true tracks and an unphysical one generated by fake tracks, which contribute to the worsening of the matching distributions in particular for the RICH detectors.

The influence of those fake tracks to final results will be estimated in detail in chapter 7 for the charged particles and in chapter 8 for the identified pions.

5.2.3 Pion Description

It is of vital importance to verify that all the track related quantities are well reproduced by the simulation. In particular, all the momentum dependent quantities need to be carefully studied: number of photon hits, ring radius and azimuthal deflection in the magnetic field.

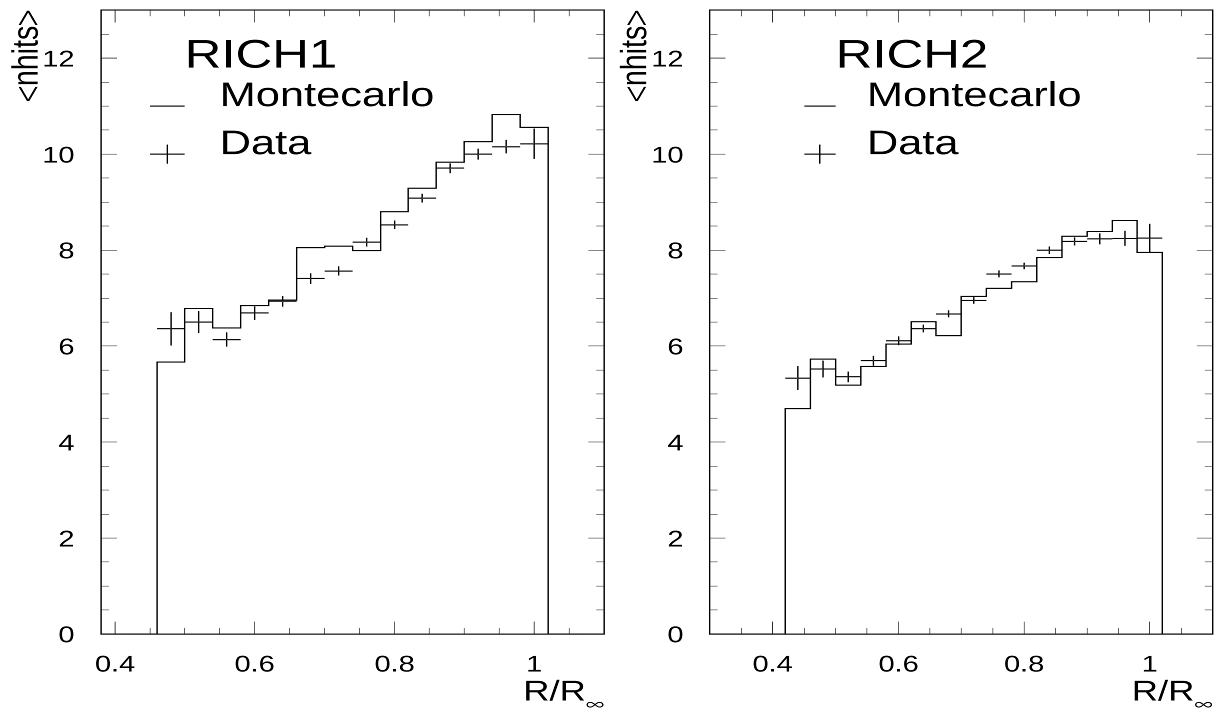

Figure 5.5: Mean number of photon hits as function of the relative ring radius for RICH1 (left) and RICH2 (right).

In Fig. 5.5, the mean number of reconstructed photon hits (*nhits*) is plotted as a function of the ring radius for both RICH1 and RICH2. As usual, the crosses represent the data and the histogram is the result obtained from the Monte-Carlo simulation. In contrast to the equations 3.3 and 3.4, which predict a parabolic dependence between *nhits* and ring radius, only a linear increase is observed. The deviation from the parabolic dependence which is not present in the pure GEANT simulation, i.e. without taking into account the detector responses (Fig. 5.6 left) originates from the finite single hit resolution of the two RICH detectors and from the limitation of the hit splitting algorithm, not able to reconstruct all of the produced hits. In Fig. 5.6 (right), the relation between the original number of GEANT hits and the reconstructed one is presented. The difference to the ideal case (dashed line) in which all photon hits are recovered is due, in the case of a small number of hits to the presence of background and for high *nhits* to the efficiency loss of hit reconstruction due to overlapping photons which are distributed over a restricted area on the ring radius.

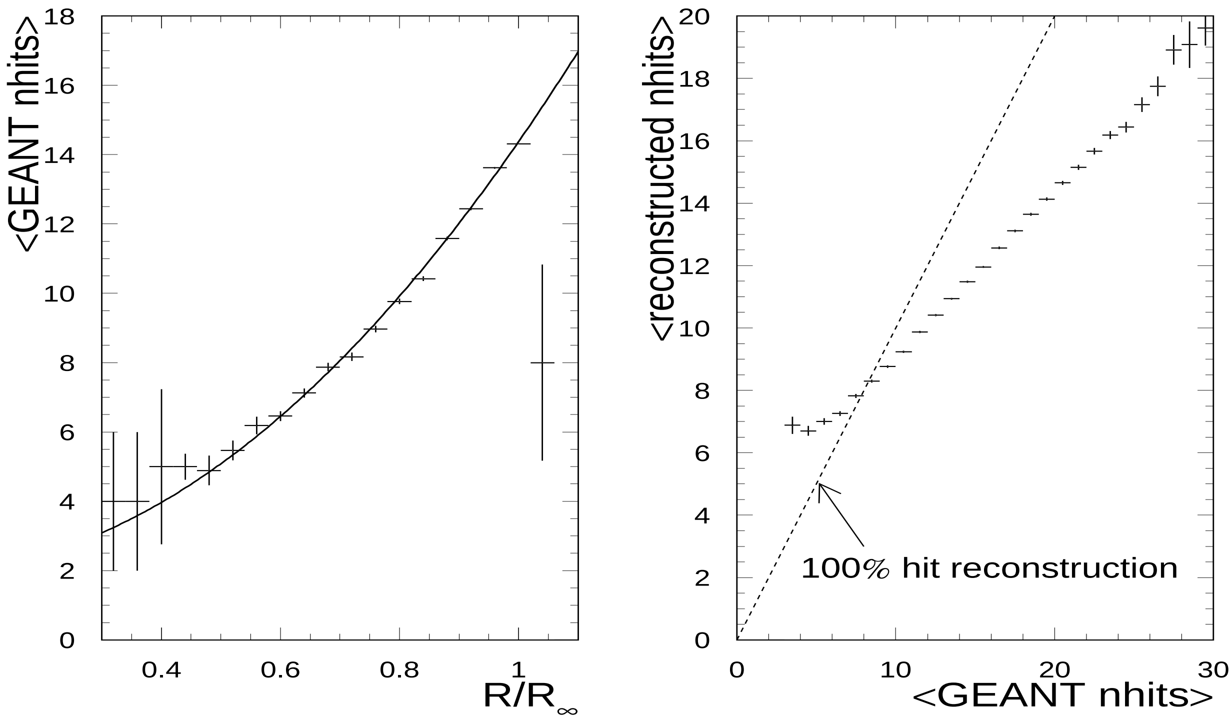

Figure 5.6: Mean number of original photon hits as function of the relative ring radius (left) and correlation between original hits and reconstructed hits (right) in the Monte-Carlo.

The deflection in the magnetic field and the ring radius determination are very important for the calculation of the particle momenta. To prove that the magnetic field configuration is well understood, one can make use of the method developed to measure the azimuthal resolution of the spectrometer (see section 4.4.1). Cutting on a small radius interval, the azimuthal deflection in Monte-Carlo and data can be compared. In Fig. 5.7 one can notice the agreement between data and simulation.

5.3 Correction Procedure

Once the simulation of the spectrometer has been implemented and all the relevant quantities characterizing the detector system have been tested and tuned, the Monte-Carlo program can be used in the correction procedure, which constitutes the most crucial parts in the whole analysis.

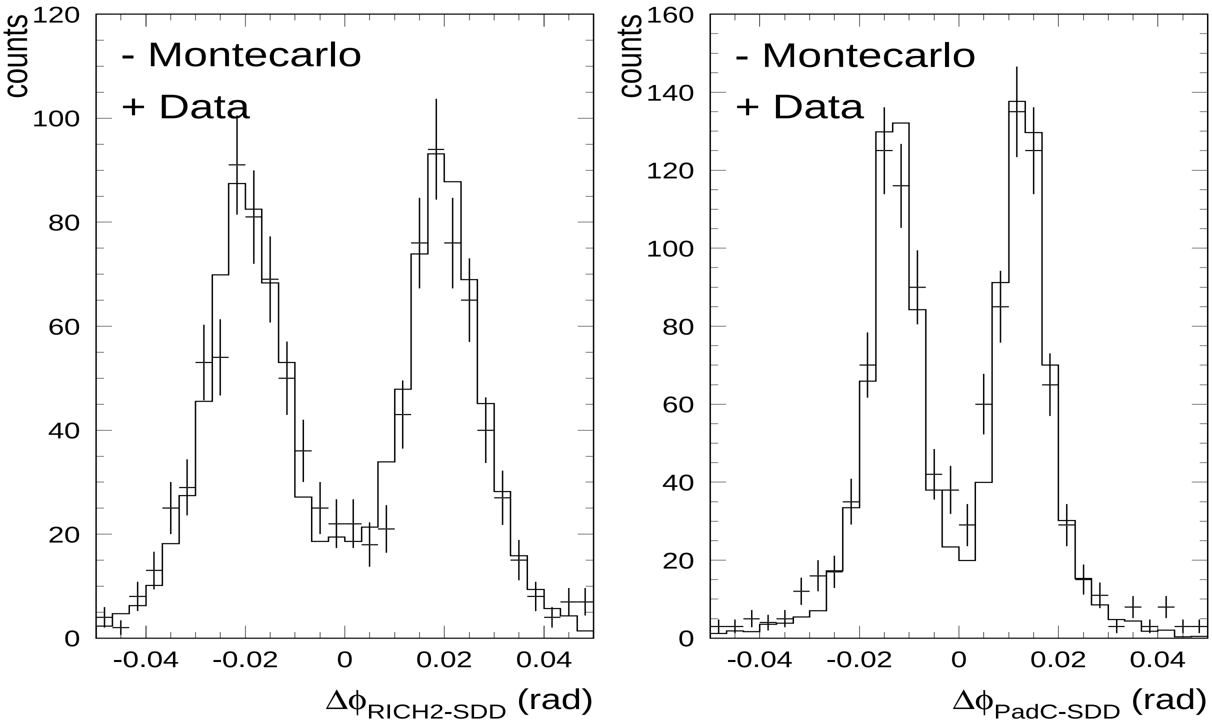

Figure 5.7: Azimuthal deflection of identified pions whose ring radius falls in the interval between 12 and 13 pads.

To study the momentum dependent track efficiency of the complete spectrometer, it is first of all necessary to produce a particle sample which consists of pions in our case. They are distributed 'white' in momentum ($dN/dp_t = const$) so that no limitation due to statistics is encountered (histogram on Fig. 5.8 left). The detector simulation and successively the processing through the whole analysis chain produces an output distribution given by the crosses on the same plot. The ratio between the two distributions, left hand side of Fig. 5.8 represents the efficiency ϵ of the system. The shape of the efficiency curve can be easily understood. At small momenta, the effect of the γ threshold of the RICH detectors produces a steep rise followed by a plateau over which the reconstruction efficiency stays constant at about 23%. The decrease for momenta larger than 20 GeV/c is due to the ring radius resolution. Ring radii in the vicinity of the asymptotic radius in fact can lead to a wrong radius determination ($\mathrm{R} > \mathrm{R}_\infty$) which has to be rejected because of the impossibility to extract the momentum (see equation 8.1).

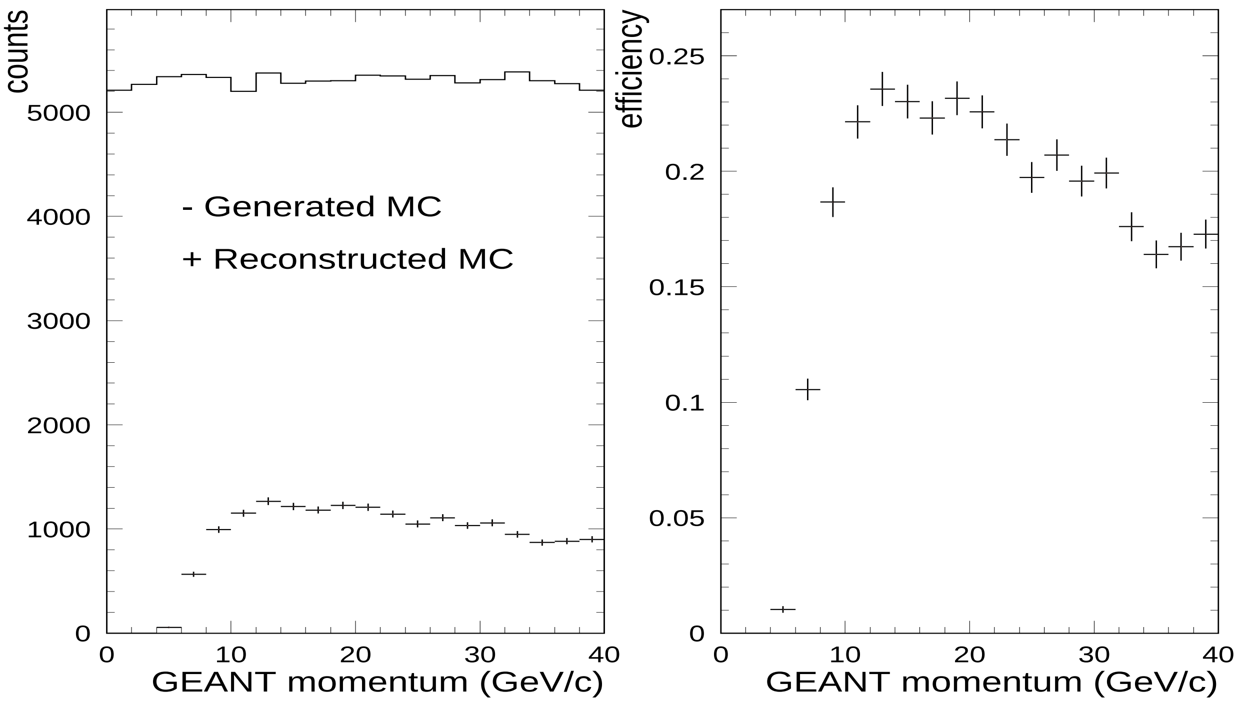

Figure 5.8: Example of momentum dependent efficiency determination using the Monte-Carlo simulation.

5.4 Overlay Technique

In CERES, many quantities, as for example the track reconstruction efficiency, are highly influenced by the number of particles produced in the collision. The reason for this is that a high hit density often leads to a wrong determination of the track coordinate and consequently to an inefficiency of the tracking algorithm. In a similar way, the presence of background hits could have a negative influence on the momentum resolution.

A standard procedure to study this effect is to use a real event as background. The simulated particle are overlayed and the usual analysis chain can be applied to the whole event (*event overlay*). Fig. 5.9 represents the dependence of the track reconstruction efficiency ϵ from the multiplicity. As expected, a growing hit density decreases the capability of the algorithm to reconstruct tracks. The trend is similar even when comparing quite different momentum regions.

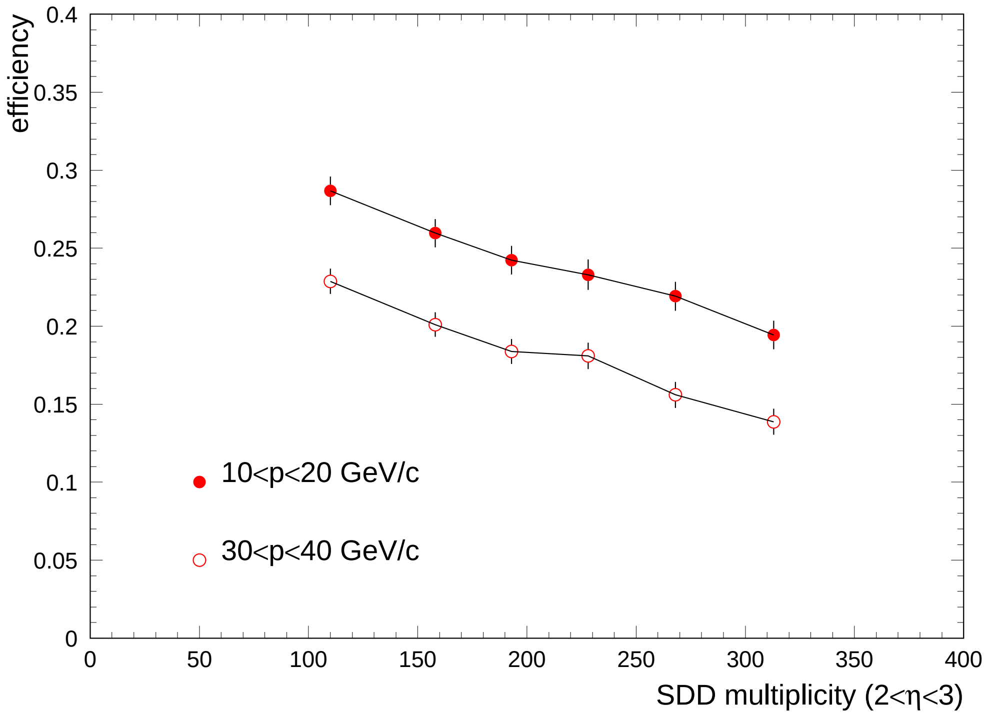

Figure 5.9: Monte-Carlo track efficiency as function of the particle multiplicity.

5.5 Systematic Errors

The accurate determination of the systematic errors is crucial to judge the quality of the data. Generally, the Monte-Carlo simulation can help to study the influence that different quantities have on the measurements.

Several sources of errors were evaluated:

- The asymptotic ring radius R_∞, which enters in the calculation of the pion momentum, is measured with a high statistic electron sample, from which an error of $< 0.1\%$ has been estimated.

- The γ threshold in both RICH detectors has been determined using a fit of the correlation between momentum calculated by the ring radius and the azimuthal deflection. From this study, the γ threshold value is obtained with an accuracy of $< 0.5\%$.

- Using identified pions, whose ring radii are correlated to the momentum, it is possible to estimate the error of the magnetic field, which is of the order of 2%.

- In the Monte-Carlo simulation a dependence of the track efficiency on the momentum of the particle and on the multiplicity that characterize the event, is observed. The influence is high for the identified pions, whose pattern recognition depends strongly on background and on the number of photons in particular near to the production threshold. The non-identified particles suffer a smaller effect: for $p_t < 1$ GeV/c, an error of 10% is estimated. It is due to gain variations and to changes on the track matching quality, residual effect of the SDD calibration as function of time. For small momenta, multiple scattering contributes to an increase of the error to 20%.

- The precision of the Monte-Carlo correction functions is dominated by the limited statistics of the simulated data and by the shape of the input distribution.

- The momentum distribution could also suffer from contamination of unrejected background or particle misidentification. A detailed analysis will be presented in chapter 7 and 8

Those different contributions produce a systematical distortion of the final results. Their influence is taken into account in the determination of the correction functions which will be discussed together with the corresponding data sets in the following chapters.

Chapter 6

Charged Particle Distributions

In this chapter global observables extracted from the data of the two SDD are presented. Beside the multiplicity of charged particles produced in the collisions, the high efficiency and excellent granularity of those detectors permit to study also local densities of particles as a function of (pseudo)-rapidity and impact parameter.

The good position resolution together with a complete azimuthal coverage allows also to examine the azimuthal anisotropy of particle production with respect to the plane which defines the reaction, the so called *reaction plane*[1]. This analysis is beyond the scope of this thesis, some preliminary results can be found in [30].

6.1 Multiplicity Distribution

In relativistic heavy ion collisions, the multiplicity, i.e. the number of particles N produced in the interaction, is a relevant observable because it quantifies to what extend the incoming beam energy is distributed to new degrees of freedom. Similar information is given also by the E_t distribution [32], i.e. the transverse energy of the particles, or by the complementary quantity E_z which represents instead mainly the energy of the fragments and nucleons that have not taken part in the interaction (*spectators*).

Using the SDD detectors, the number of charged particles $\mathrm{N_{ch}}$ emitted in one unit of pseudorapidity from 2 to 3 has been extracted. The raw data, obtained by matching silicon hits which point to the same vertex, have been corrected for efficiency and for *pile up*, which originates from the finite double hit resolution of the detectors. The necessary corrections have been derived with a Monte-Carlo which contains the full and complete simulation of a large number of particle

[1]The reaction plane is the plane defined by the beam direction and the impact parameter vector

traversing the spectrometer. In the simulation not only the products of strong interactions are described but also the beam passage through the target (producing δ electrons), particle decays and γ conversions in the material upstream of the SDD. In addition, a description of the electronic background, noise and pick up, which can produce fake tracks has been fully implemented.

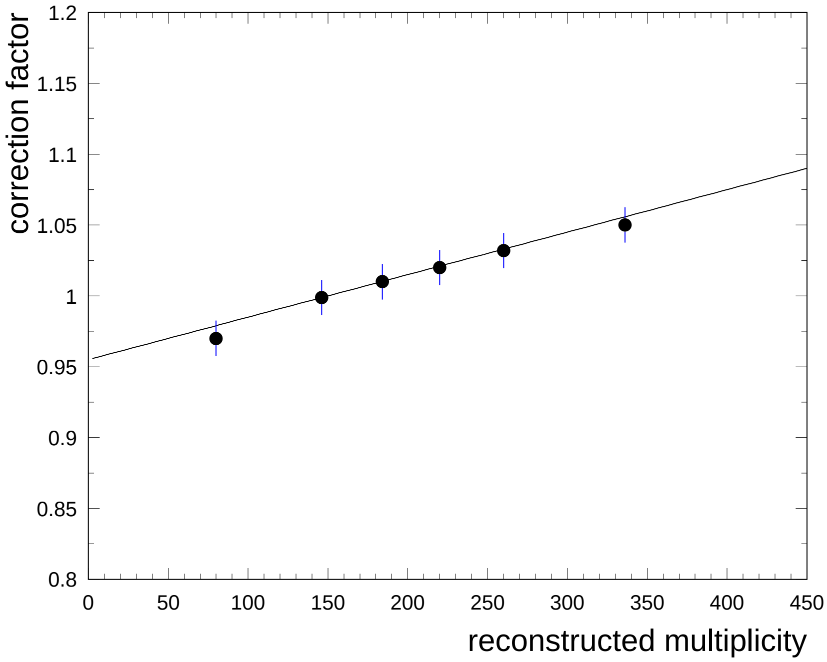

Figure 6.1: Multiplicity dependence of the correction factor.

Fig. 6.1 shows the correction factor necessary to achieve the true multiplicity:

$$\text{correction factor} = \frac{\text{number of MonteCarlo tracks}}{\text{number of reconstructed tracks}}$$

The curve has empirically been fitted by a linear function. For low multiplicities, more tracks than produced in the collisions are observed. This results from δ-electrons from target, up to a maximum of 20 δ electrons per event falls in the SDD acceptance, and fake combination of SDD1 and SDD2 hits. For high multiplicity the correction gets larger than 1, i.e. not all particles trajectory are reconstructed. The main reason is the double hit resolution which is in radial direction $600 - 800\ \mu m$.

The corrected data are illustrated in Fig. 6.2. The lines represent seven centrality selections, from semi-central collisions (M1) to the most central one (M7), corresponding to $\sigma_{geo} = 2.3\%$ (see next section).

6.2 Cross-Section

The data recorded in the 1995 beam time cover a wide range in impact pa-

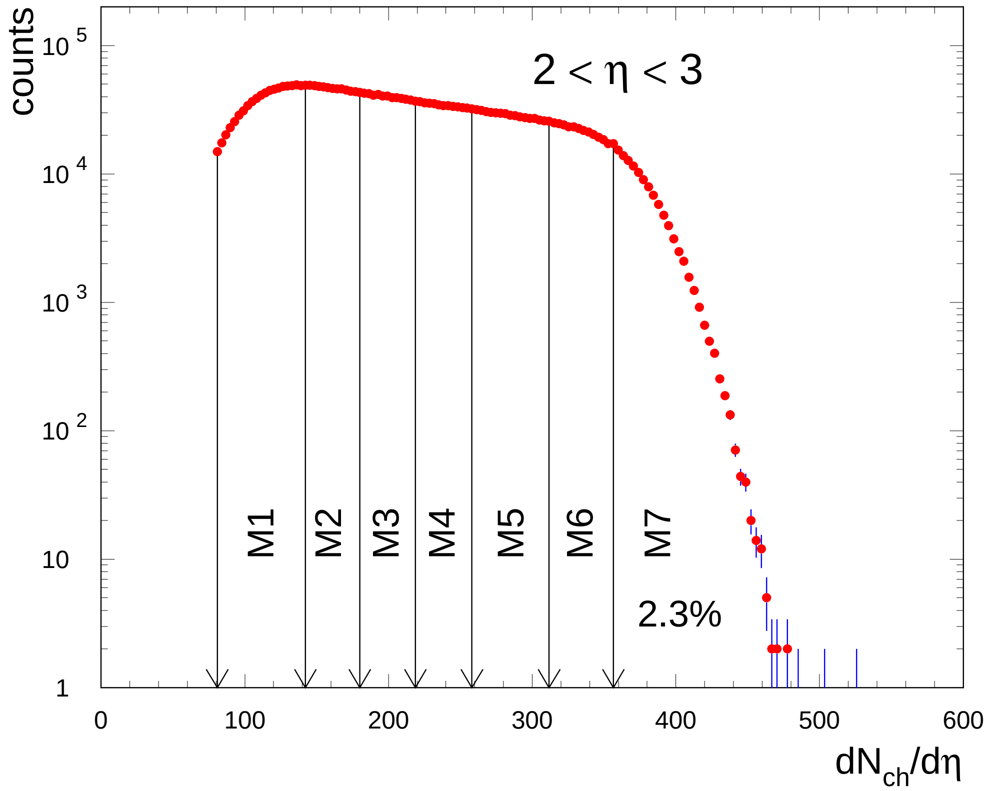

Figure 6.2: Multiplicity distribution.

rameter. The centrality of the collision is determined from the charged particle multiplicity and referred to the fraction of the total geometric cross-section σ_{geo}, which is defined by the size of the nuclei:

$$\sigma_{geo} = \pi \cdot (R_a + R_b)^2 \qquad R_{a,b} = r_0 \cdot A^{1/3} \tag{6.1}$$

$R_{a,b}$ are the radii of the target and projectile, whose dimension increases monotonically with the number of nucleons A (r_0 is typically 1.2 fm).

In Fig. 6.3, taken from reference [31], the relation between the cut on the charged particle multiplicity and the fraction X of the covered geometrical cross-section is plotted. X is given by:

$$X = \frac{1}{\sigma_{geo}} \int_{N_{ch}(cut)}^{\infty} (d\sigma/dN_{ch}) dN_{ch} \tag{6.2}$$

Cutting on the number of charged particles N_{ch} that are within the SDD acceptance allows to choose a different collision geometry. The possibility to study the centrality dependence of different quantities, provides additional constraints which are important for a realistic description of the produced hot and dense interaction zone and of the reaction mechanism.

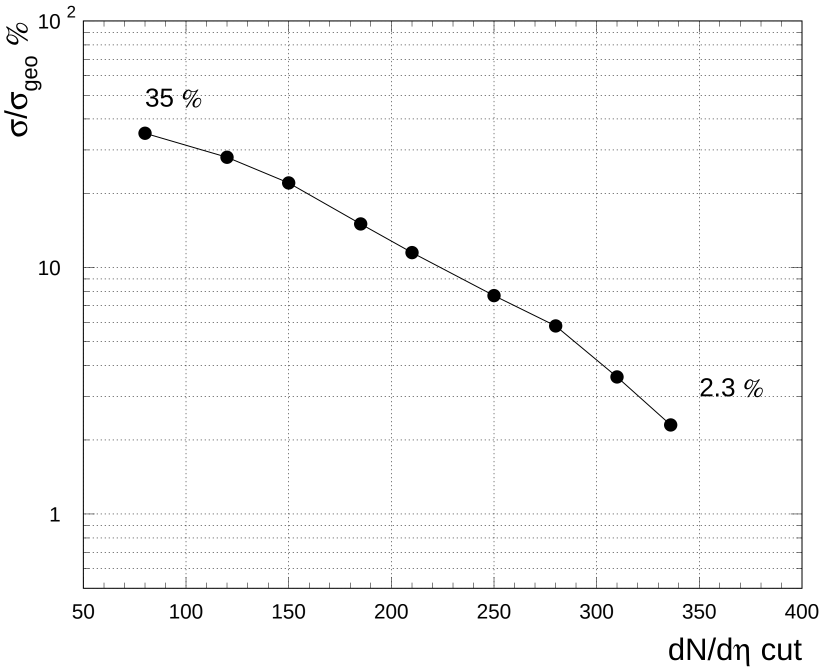

Figure 6.3: Fraction of geometric cross-section as a function of the cut on the charged particles emitted in one unit of pseudorapidity ($2 < \eta < 3$).

6.3 Pseudorapidity Distribution

Due to the high granularity of the SDD detectors and their wide coverage in pseudorapidity, it is possible to study the charged particle distribution and its dependence on centrality.

In the high multiplicity environment, the restricted reconstruction efficiency as well as the influence of the background produced by δ electrons and γ conversions causes the necessity of differential data corrections. Particularly the dependence of the track reconstruction efficiency on the local hit density was identified as the most important effect. A complete and accurate Monte-Carlo simulation of more than 1000 VENUS [33] events covering different impact parameters has been performed in a similar way to that described in section 6.1. For every multiplicity interval the pseudorapidity dependence of the correction term is calculated. Examples are shown in Fig.6.4, in which one can observe that the correction factor increases with centrality or in general with the local particle density.

The corrected data are presented in Fig. 6.5 for different centrality selections (Fig. 6.2). Interestingly the charged particle density becomes narrower when central collisions are approached (bottom –top). A more quantitative analysis can be done fitting the distributions with Gauss-functions. The maximum as well as the width of the Gauss-fit is plotted as function of the centrality in Fig. 6.6. In the top panel, the increase of the maximum corresponds to an increase in the number of participants in the collision. The width of the distribution (bottom panel) exhibits

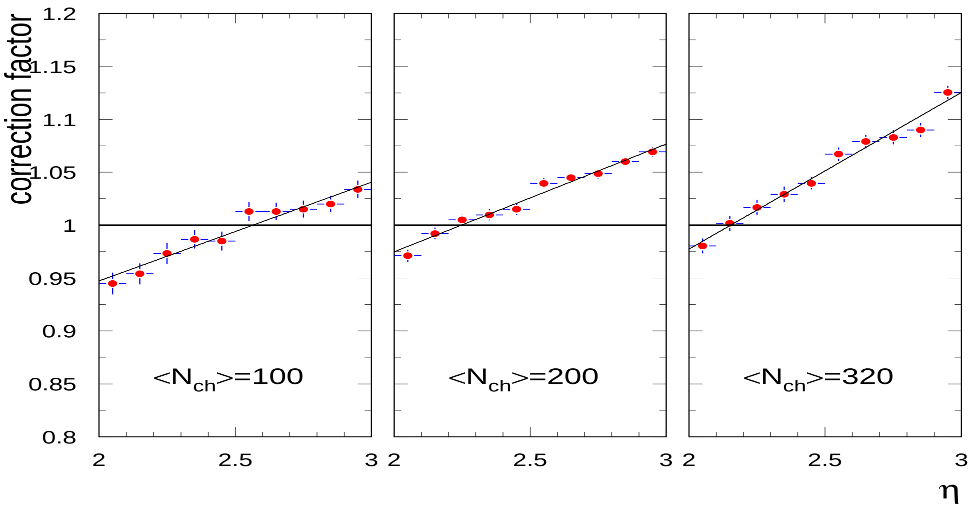

Figure 6.4: Dependence of the correction factor from pseudorapidity and multiplicity.

instead a narrowing of the shape. This can be associated with the higher degree of stopping reached in the interaction (see section 2.3).

The comparison of the CERES results with those of the NA49 experiment, which has measured only negative hadrons (h^-) for $\sigma/\sigma_{geo} = 5\%$, shows that the width of the distribution of the NA49 h^-[54] (open points in the Fig.6.6) is, as expected, somewhat (around 4%) narrower. The reason can be seen in the fact that CERES measures the sum of positive and negative charged particles, whose distribution is, due to the presence of protons, slightly wider.

Interesting is also the comparison with model predictions. Two of them have been studied: VENUS (version 4.10) [33] and RQMD (version 2.3) [34].

	σ/σ_{geo} %	$\langle\sigma/\sigma_{geo}\rangle$ %	Data N_{ch} cut	Models $b_{min} - b_{max}$ cut (fm)
M1	$22 - 35$	26.44	$80 - 140$	$6.6 - 8.35$
M2	$15 - 22$	18.27	$140 - 180$	$5.5 - 6.6$
M3	$11 - 15$	12.85	$180 - 215$	$4.7 - 5.5$
M4	$7.7 - 11$	9.11	$215 - 253$	$3.9 - 4.7$
M5	$5. - 7.7$	6.2	$253 - 308$	$3.15 - 3.9$
M6	$2.3 - 5$	3.22	$308 - 355$	$2.2 - 3.15$
M7	< 2.3	1.8	> 355	< 2.2

Table 6.1: Centrality selections: the cuts used on the data set and on the models are reported in correlation to the fraction of the covered cross-section.

Using the following equation:

$$\sigma = 2\pi \cdot \int_{b_{min}}^{b_{max}} b \, db$$

which correlates the impact parameter b to the cross-section σ, one can select for the models the same centrality range as for the data (see Table 6.1).

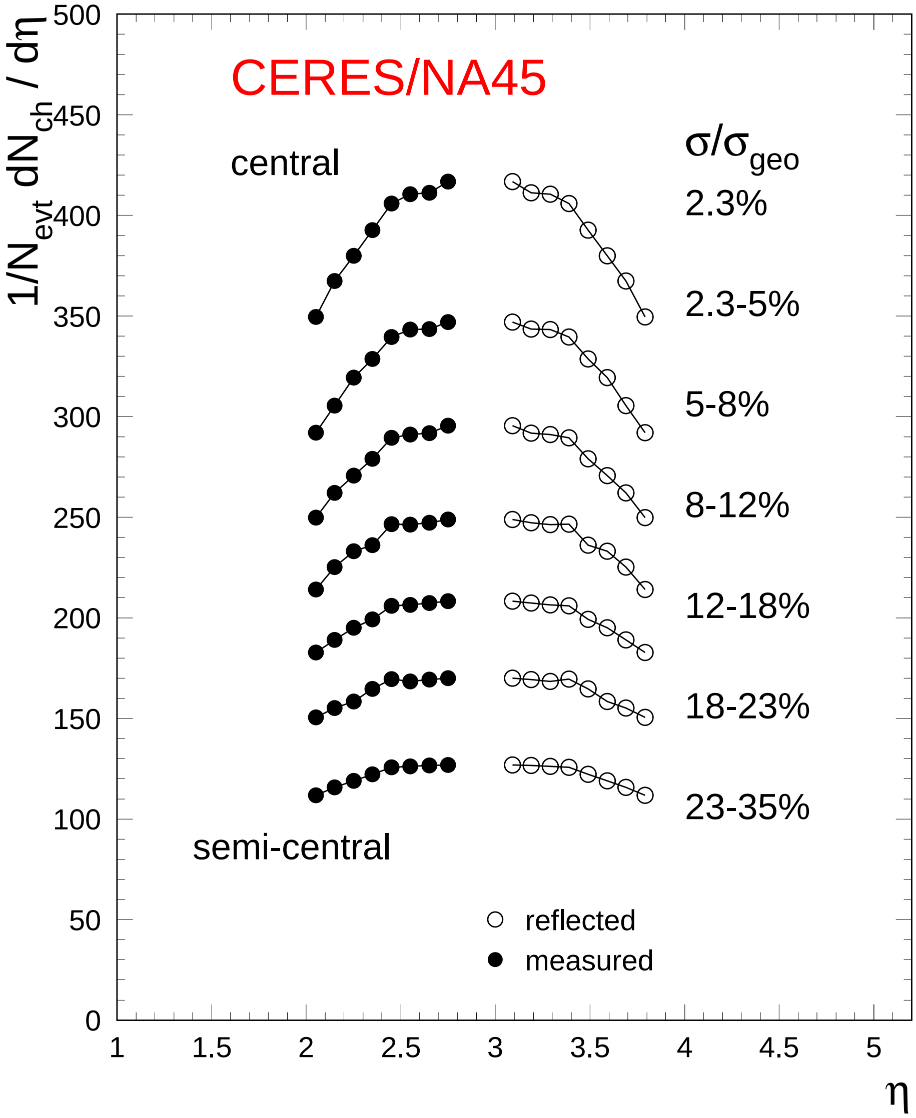

Figure 6.5: The charged particle pseudorapidity distribution is shown for different centrality selections. The full points (•) represent the measured data after correction. The open symbols (◦) are the data reflected around mid-(pseudo)-rapidity assuming also symmetry in pseudorapidity which should be valid at least for pions in this region.

As it can be seen in Fig. 6.6, both VENUS and RQMD seem to describe the shape of the maximum of the Gauss-distribution but overestimate its absolute value.

Concerning the width of the pseudorapidity distribution the models fail in reproducing the change with the centrality. RQMD, for example, does not describe the saturation for semi-central collisions ($\sigma/\sigma_{geo} = 20 - 30\%$) and VENUS is much narrower than the data.

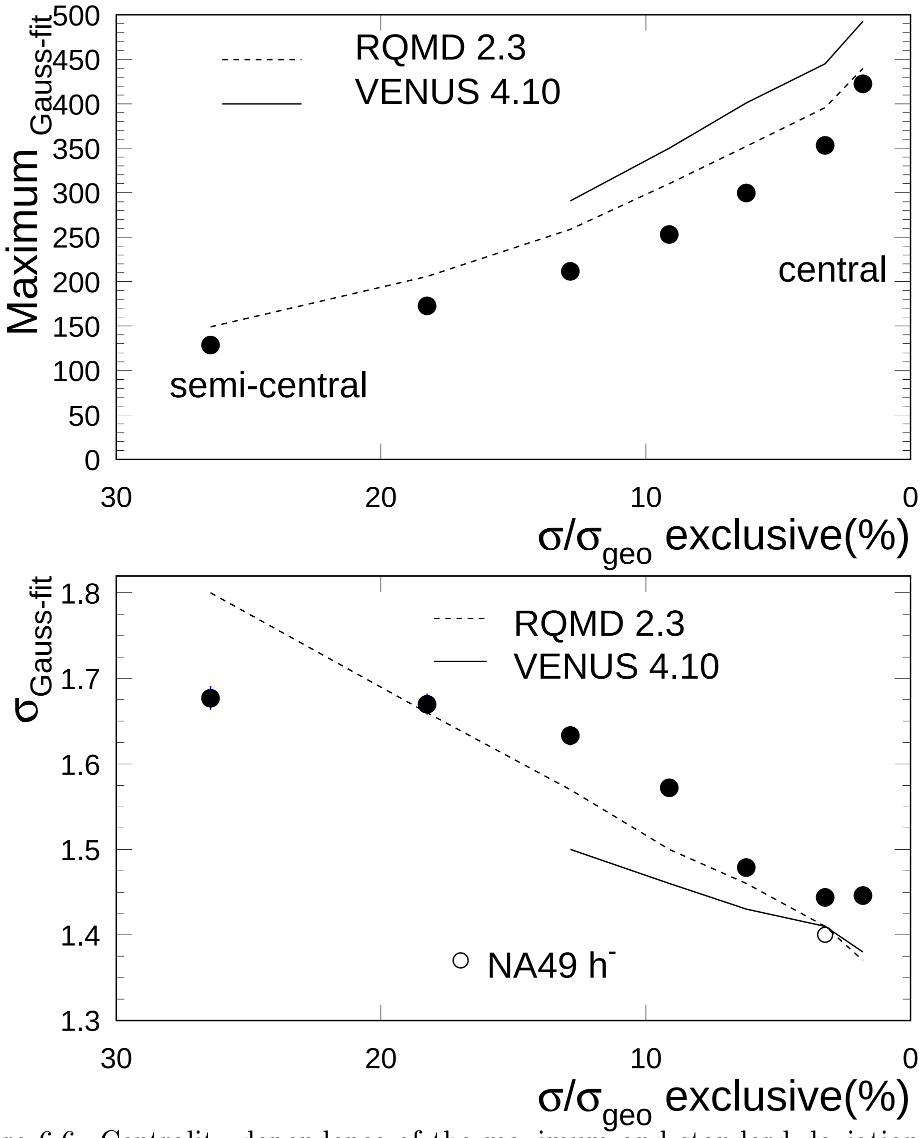

Figure 6.6: Centrality dependence of the maximum and standard deviation (width) of the Gauss-fit. Also shown are the comparisons with models (VENUS and RQMD) and the NA49 experiment (see text).

Chapter 7

Momentum spectra of charged hadrons

Using the information from the SDD telescope positioned in front of the magnetic field and the Pad Chamber located after it, CERES offers the possibility to measure the momentum distribution of positive and negative particles, on a statistical basis and without particle identification.

This chapter discusses in detail the statistical method used to extract the signal and the necessary corrections. The negative particle distributions consisting of mostly pions and the positive charge excess, which is closely linked to the net proton distribution, are presented. Particular emphasis is given to the centrality dependence of the spectra.

7.1 Analysis Method

The charged particle tracking in CERES extrapolates track segments from the SDD, about 10 cm after the target, $3m$ downstream to the Pad Chamber. Track candidates are defined by a match of the extrapolation with a hit in the Pad Chamber in polar angle θ and in azimuthal direction ϕ. The match in azimuthal direction defines a lower momentum cut off of 1 GeV/c. In this way, counting all the possible matches (M) found in the window, one obtains not only the true signal (S) but also random combinations (B) of track segments in the SDD and hits in the Pad Chamber not originating from the same particle.

The contribution of the random tracks can be estimated using an *event mixing* strategy in which, SDD data are analyzed together with Pad Chamber data from a different event of the same multiplicity. Instead of event mixing a similar but technically simpler method based on *detector rotations* is used. For every event, all hits in the Pad Chamber are shifted by a random angle in azimuthal direction. The physical signal is destroyed, tracks result by definition from random combinations and therefore the background B is measured. Now the signal (S) can be extracted by subtracting the two contributions S = M − B. The momentum and charge of the particle are calculated from the azimuthal ϕ deflection[1].

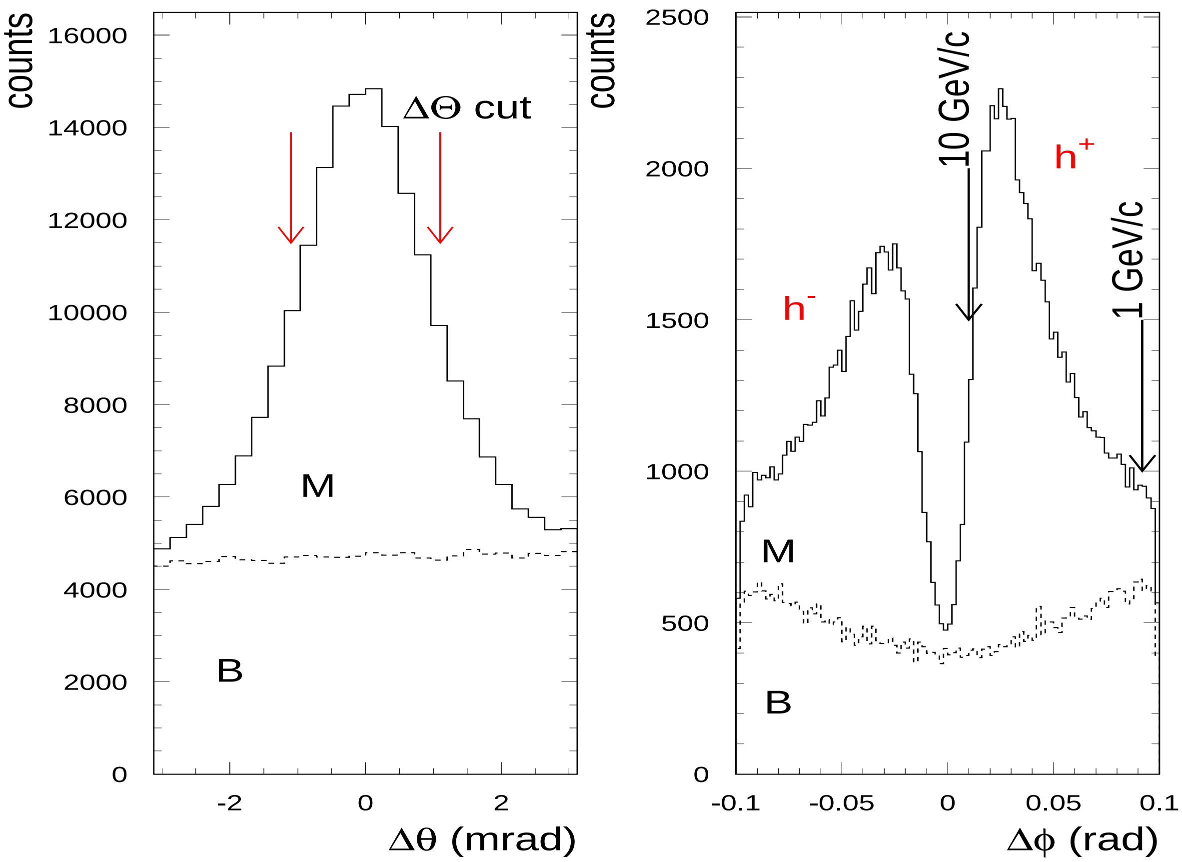

Figure 7.1: $\Delta\theta$ and $\Delta\phi$ distribution for *candidate tracks* (full line) and for *background tracks* (dashed line).

Fig. 7.1 presents the signal obtained with this method. On the left side, the θ match between the SDD and Pad Chamber is shown together with the cut used in the analysis:

$$\Delta\theta = \pm 1.28\ \sigma_{\Delta\theta}(\mathrm{p_t}),$$

This rather tight cut optimizes the statistical significance, i.e. the signal-to-background ratio and the efficiency. It has been determined by finding the maximum of the product of efficiency and S/B as a function of the cut values (in sigma) (Fig. 7.2).

On the right side of Fig. 7.1, the azimuthal deflection $\Delta\phi$ of the reconstructed tracks (full line) is compared to the background (dashed line). A positive $\Delta\phi$

[1]See section 4.4.1

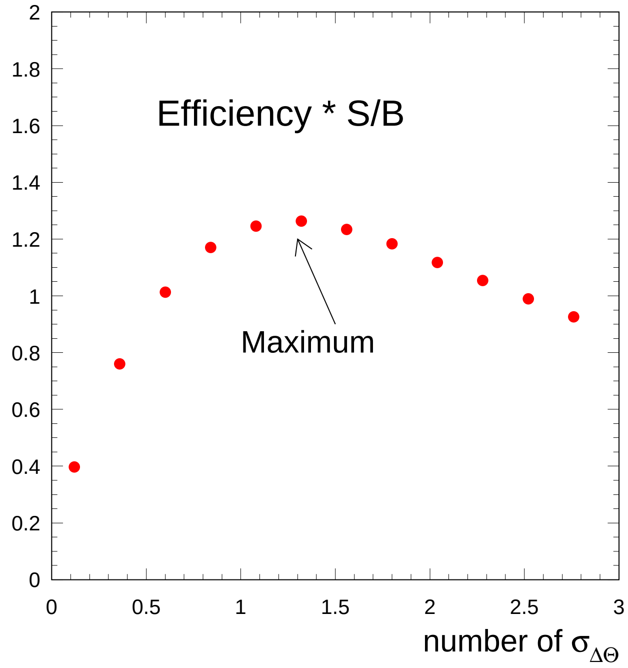

Figure 7.2: Product of efficiency and S/B as a function of the cut values (in sigma).

corresponds to a positive track h^+ and negative $\Delta\phi$ to a negative one h^-. To give an idea of the momentum range covered by this kind of analysis, lines representing the lower momentum cut at 1 GeV/c and an upper one at 10 GeV/c are also drawn. The non-flat distribution of the background is due to a momentum dependent $\Delta\theta$ cut which takes into account the momentum dependence of the θ match due to multiple scattering.

7.2 Spectrometer Acceptance

The fixed coverage of the polar angle θ of the CERES spectrometer (from 8^o to 15^o degrees) translates, for different particles, in a variable rapidity acceptance which is shown in Fig. 7.3 for protons and pions. For pions CERES covers quite homogeneously the rapidity interval from 2.1 to 2.6, therefore the spectra will be presented in such rapidity range. For protons instead, a larger range from 1.0 to 2.5 is covered but with different transverse momentum acceptance for each rapidity interval. Consequently in the following, the data will analyzed separately in 0.1 unit of rapidity.

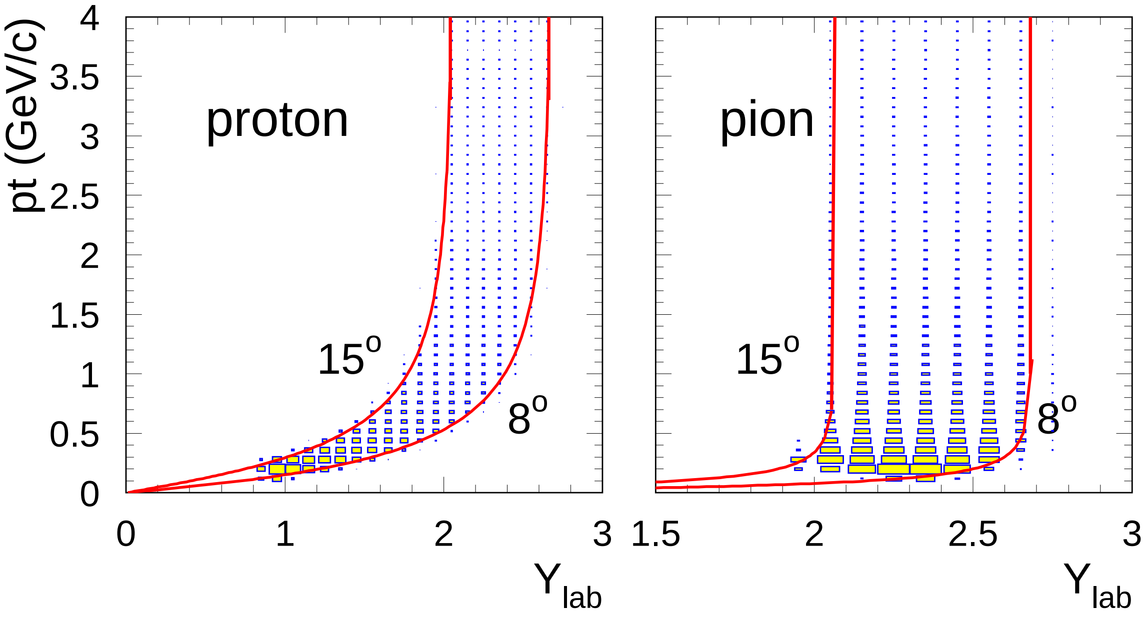

Figure 7.3: Spectrometer acceptance for protons and pions.

7.3 Raw Transverse Momentum Distributions

From the azimuthal deflection of the particles in the magnetic field, the momentum p of the negative and positive hadrons is determined (see 4.4.1). With the polar angle θ, the transverse momentum results as:

$$\mathrm{p_t} = \mathrm{p} \cdot \sin(\theta)$$

The distributions[2] for signal (S) and background (B) are shown in Fig. 7.4 (left) in the range $0-2$ GeV/c for a sample consisting of about 2000 events. The right hand side of the same figure illustrates the S/B ratio.

Over most of the $\mathrm{p_t}$ region covered, the ratio is well above 1. For small values (pt $<$ 300 MeV/c) it decreases due to the enhanced background resulting from the momentum dependent $\Delta\theta$ cut. At large p_t ($\mathrm{p_t} > 1$ GeV/c) where the particle yield decreases rapidly the S/B also deteriorates. The background subtracted transverse momentum distributions of the negative particles h^- and of the positive charge excess $\mathrm{h}^+ - \mathrm{h}^-$ are plotted respectively in Figs. 7.5 and 7.6. These spectra have been extracted from $3 \cdot 10^6$ analyzed raw data events, covering the upper 35% of the geometrical cross-section, and represent $70 \cdot 10^6$ negative and $88 \cdot 10^6$ positive tracks. [3]

7.4 Corrections

The data (Figs. 7.5 and 7.6) still have to undergo different corrections before

[2]See appendix A

[3]i.e. about 50 tracks/evt. This is much smaller than the overall charged particle multiplicity mainly because of the applied momentum cut.

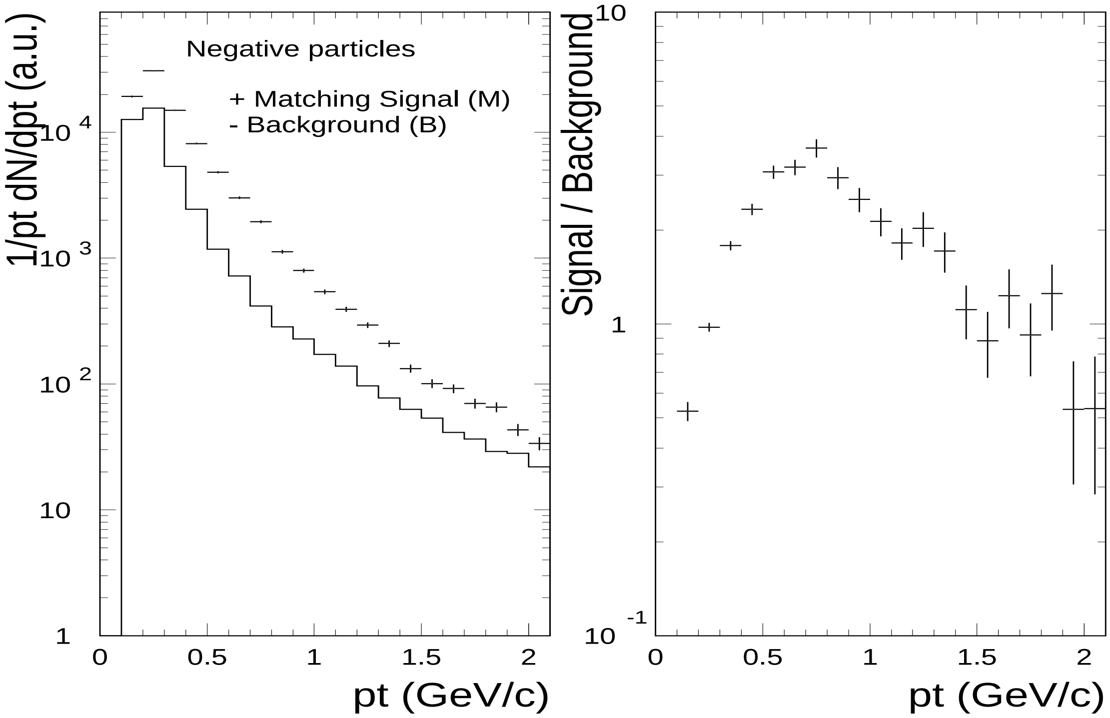

Figure 7.4: P_t distribution of the signal and the background for 2000 events.

they can be interpreted. Three contributions are distinguished: (i) pile up, (ii) efficiency and geometrical acceptance and (iii) momentum resolution.

7.4.1 Pile Up

The term *pile up* addresses the situation where it is not possible to resolve hits because they are too close in time and space.

If a particle falls into a detector region that for some reason is particularly rich of background, the true signal overlaps with background hits and can not longer be resolved. Its contribution would be subtracted in the above described method. The consequence is that in a region of high hit density, for example at small polar angle or high multiplicity, the track reconstruction will be characterized by a low efficiency which is due to pile up. More precisely, the matching signal M will be:

$$\mathrm{M} = (1-\omega)\ \mathrm{S} + \mathrm{B} \quad \text{or} \quad \mathrm{S} = \frac{\mathrm{M}-\mathrm{B}}{1-\omega},$$

where ω is the pile up probability. In the limit of ω equal zero, we have the normal case quoted before. With 100% pile up probability, it will not be possible to extract any signal.

The θ dependence of the average pile up probability is presented in Fig. 7.7, where the maximum value of 9%, for high hit densities, at small polar angle, decreases to 6% at large θ.

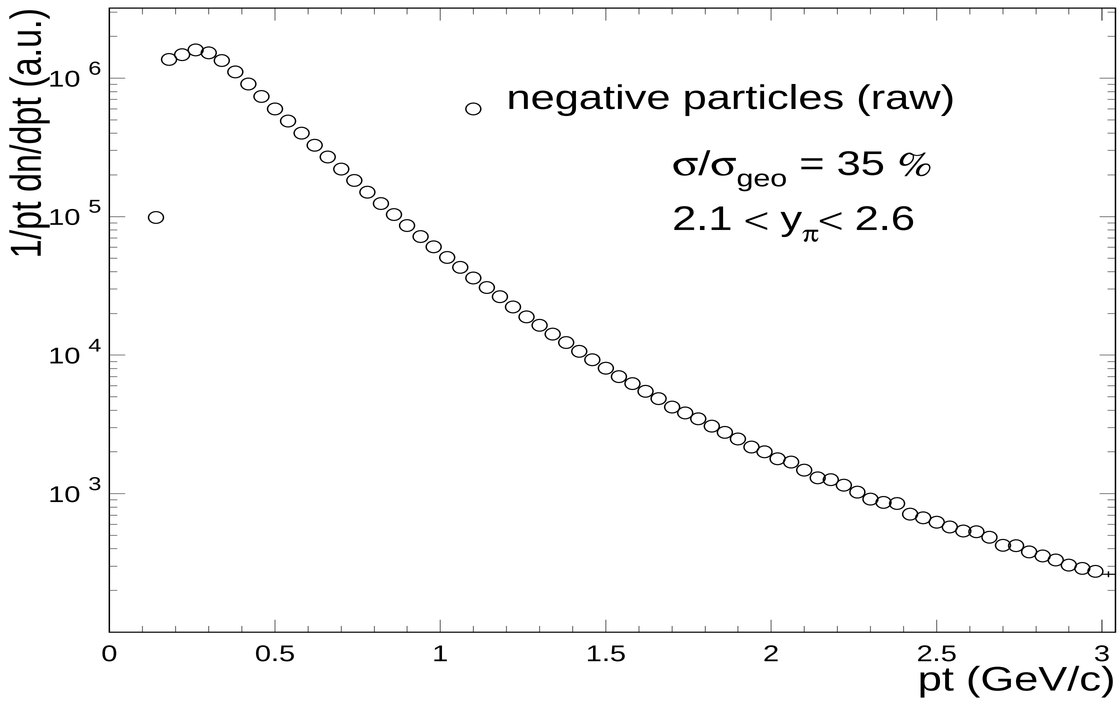

Figure 7.5: Transverse momentum distribution (not corrected) of negative particles.

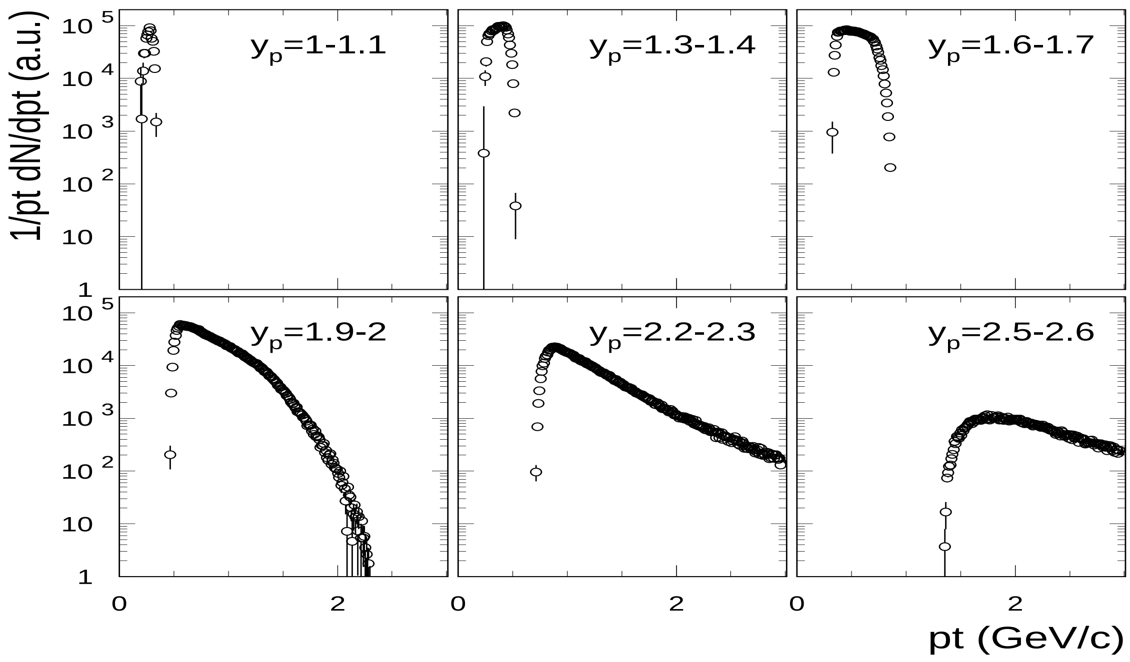

Figure 7.6: Raw momentum distribution of $h^+ - h^-$ for different rapidity intervals.

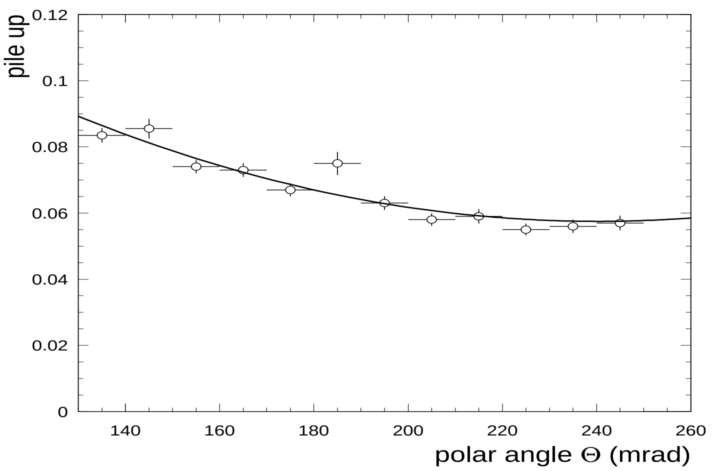

Figure 7.7: Theta dependence of the pile up probability.

7.4.2 Efficiency and Geometrical Acceptance

With the help of the Monte-Carlo simulation, the track reconstruction efficiency has been determined for both h^- and $h^+ - h^-$. It contains the efficiency of the track reconstruction algorithm, the efficiency of the individual detectors as well as the geometrical acceptance of the spectrometer. For the h^- (Fig. 7.8), the efficiency curve is characterized by a wide plateau between 800 MeV/c and 4 GeV/c.

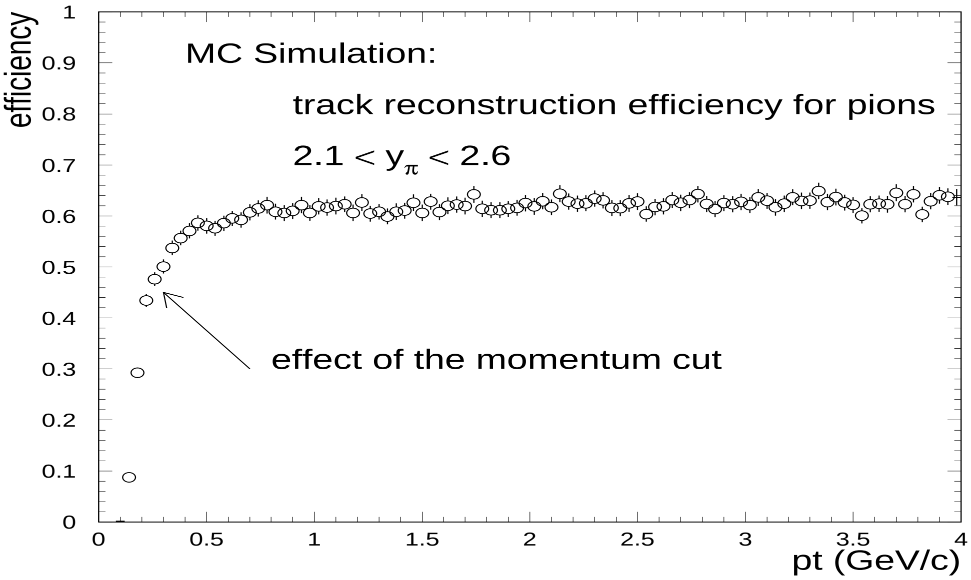

Figure 7.8: Track reconstruction efficiency for charged pion in the rapidity interval $2.1 < y_\pi < 2.6$.

The decrease for small p_t is caused by the fix cut off in azimuthal deflection applied in the analysis chain, which corresponds to a gradual cut in transverse momentum. The reconstruction efficiency does not vary within the rapidity window.

For protons, one has basically the same picture but, due to the geometrical acceptance of the spectrometer, a strong dependence of the efficiency correction for different rapidity range is observed (Fig. 7.9).

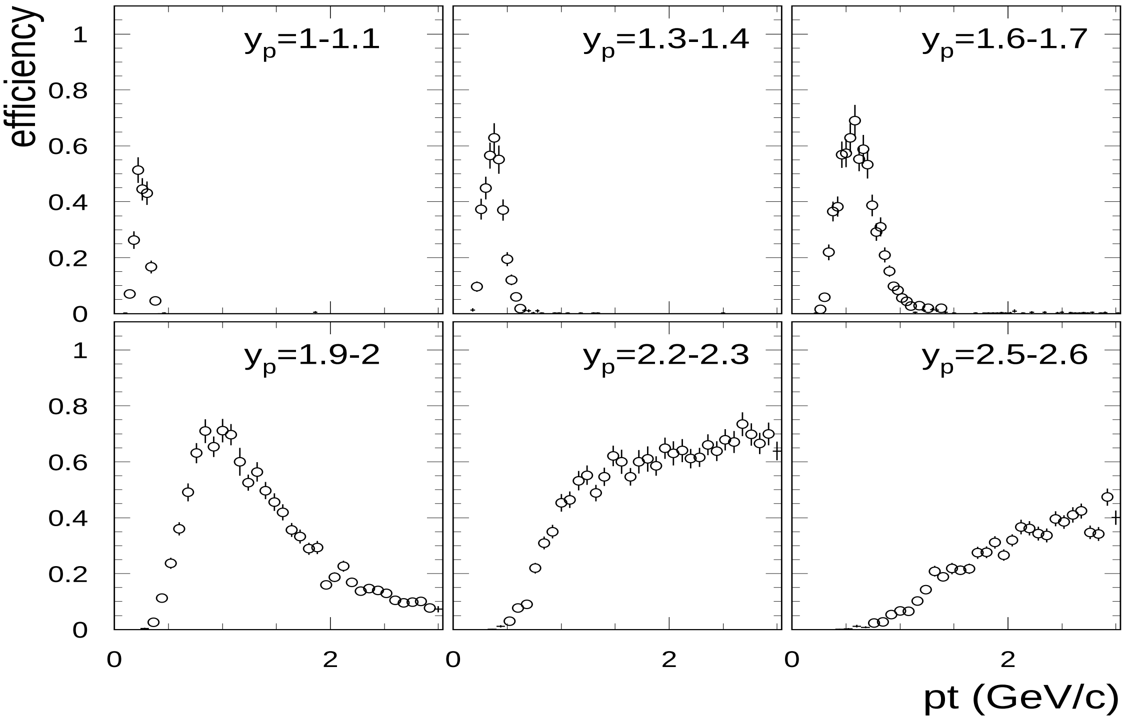

Figure 7.9: Proton track reconstruction efficiency for different rapidity ranges.

7.4.3 Momentum Resolution

Due to the limited resolution of the spectrometer the measured transverse momentum distributions are distorted at higher p_t. The correction is calculated by a Monte-Carlo (MC) procedure which automatically also takes in account the efficiency and acceptance effects described in 7.4.2.

Particles are generated with a certain momentum distribution and tracked through the Monte-Carlo simulation. The correction function is calculated as the ratio of MC input to output distribution:

$$\text{correction function} = \frac{f^{in}_{MC}(p_t, y)}{f^{out}_{MC}(p_t, y)}$$

The left hand side of Fig. 7.10 shows an example of how a Monte-Carlo input distribution represented by an exponential of inverse slope 200 MeV (full line), is strongly modified (dashed line) by the finite resolution. The smearing strongly depends on the Monte-Carlo input as indicated for different inverse slope parameter in Fig. 7.10 (right).

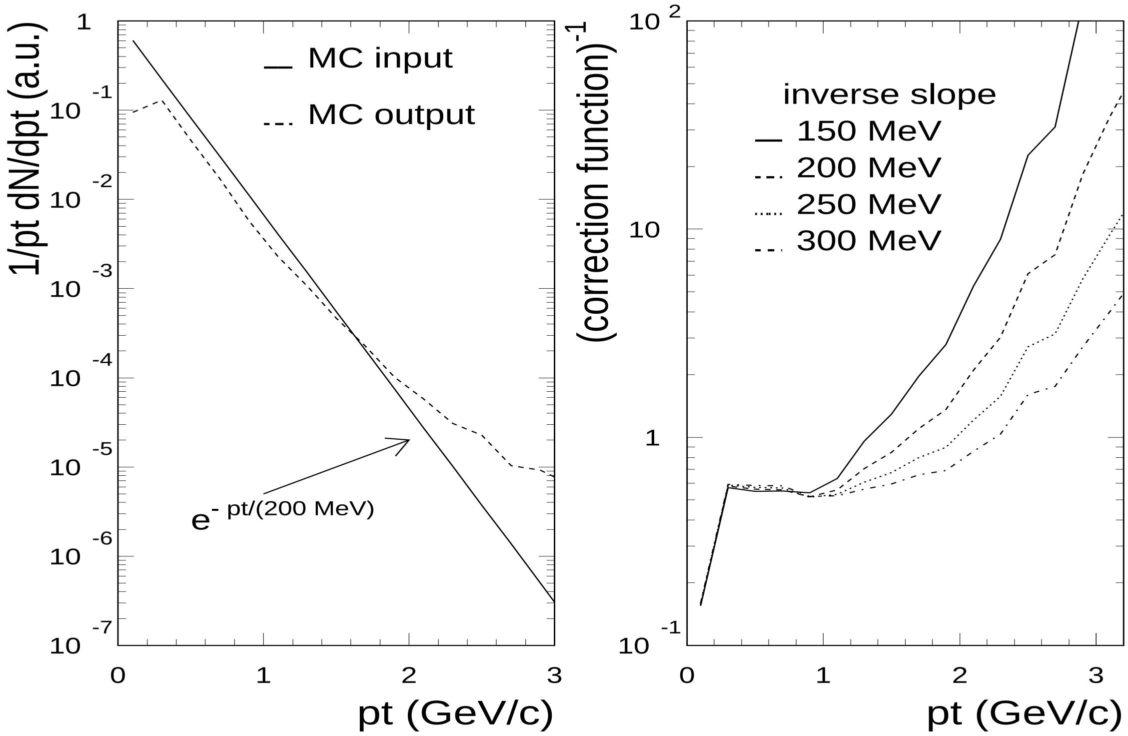

Figure 7.10: Due to the limited momentum resolution, the MC input distribution results modified (left). Dependence of the correction function from the MC input.

An iterative process is used to find the correct MC input distribution. The basic assumption of the technique is that the cross-section factorizes in $\mathrm{p_t}$ and y:

$$\mathrm{f^{in}_{MC}(p_t, y) = f(p_t) \cdot g(y)}$$

Both $\mathrm{p_t}$ and y are randomly distributed in the following intervals:

	π^-	p
y	2.0-2.8	1.0-2.8
$\mathrm{p_t}$	0.-5. (GeV/c)	0.-5. (GeV/c)

Large samples of pions and protons are generated and tracked through the detector simulation. A realistic $\mathrm{p_t}$ distribution is obtained by weighting different tracks by a factor, which is a function of the random p_t. The weight function can be iteratively changed such that various input distributions are produced without generating new GEANT events. The comparison of the MC output distribution to the data stops the iteration at the point where the MC distribution agrees with the measured one.

Fig. 7.11 presents some examples which compare the data (black symbol) with the Monte-Carlo output (histogram). The weight function is tuned until the ratio of the two distributions is constant as function of p_t and centered on one.

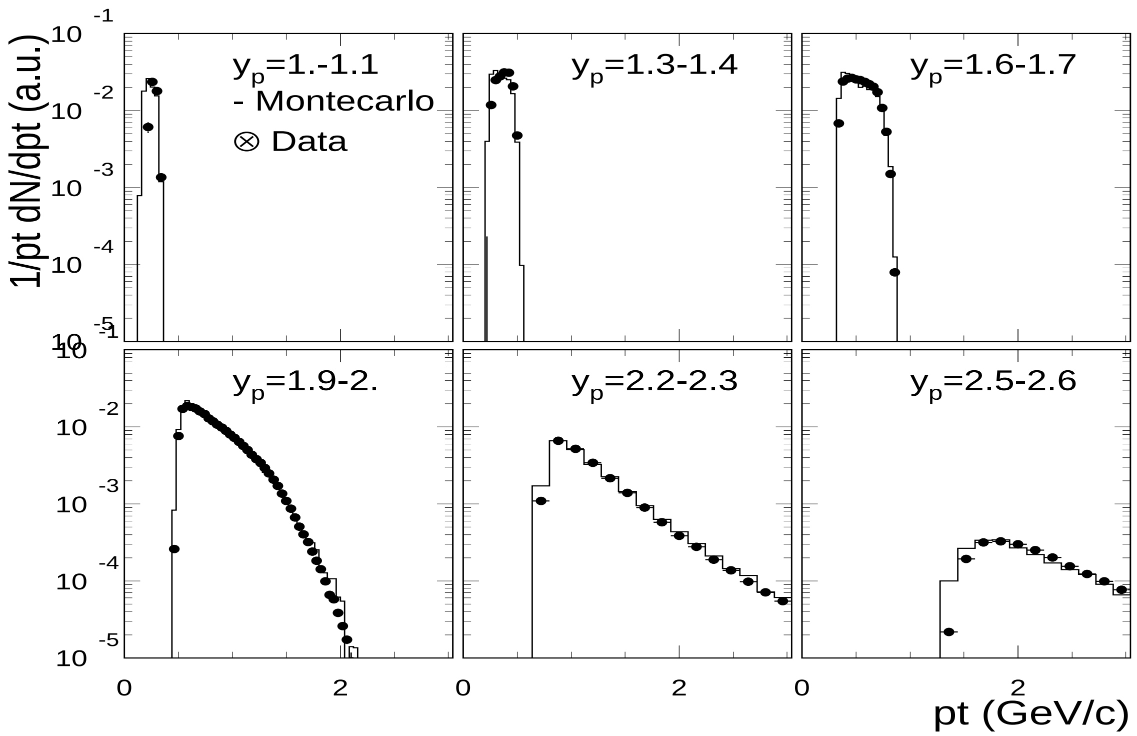

Figure 7.11: Comparison of Monte-Carlo output to data for different rapidity ranges.

7.5 Negative Hadrons h^-

The transverse mass distributions are shown in Fig. 7.12 for the range $2.1 < y < 2.6$. Transverse mass and rapidity have been calculated using the pion mass.

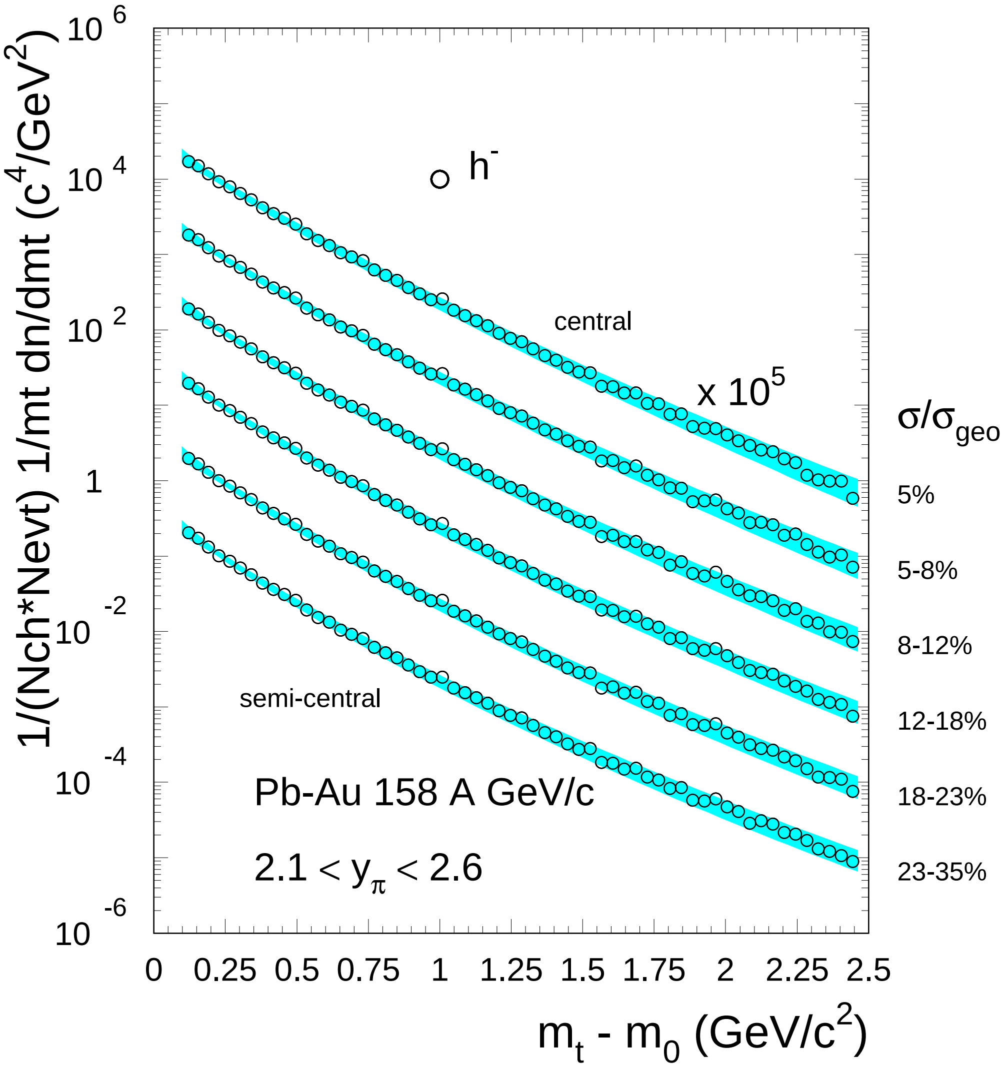

Figure 7.12: In the pseudorapidity interval between 2.1 and 2.6, the h^- spectra have been measured for different mutually exclusive centrality selections. The band represents the systematic uncertainty of the MC input distribution.

All the analyzed data have been divided in several not overlapping multiplicity bins (see chapter 6), which range from semi-central ($\sigma/\sigma_{\mathrm{geo}} = 22\%-35\%$) to central collisions ($\sigma/\sigma_{\mathrm{geo}} < 5\%$). The corrected data, normalized per event and per number of charged particles produced in one pseudorapidity interval, have been successively scaled by a factor of 10. The band represents the systematic uncertainties due to the MC input correction. It is approximatively 10% at $m_t - m_0 = 1\ GeV/c^2$ and

30% at 2 GeV/c^2.

An additional systematical error arises when interpreting negative particle as pion spectra. Possible contributions from other particles based on VENUS [33] events tracked through our GEANT simulation have been investigated. The m_t spectra obtained after our analysis procedure are shown in Fig. 7.13. The electron contamination is negligible for $m_t - m_0 > 100\ MeV/c^2$. Kaons and antiprotons become relevant only above 1 GeV/c^2 where they contribute 10% according to VENUS.

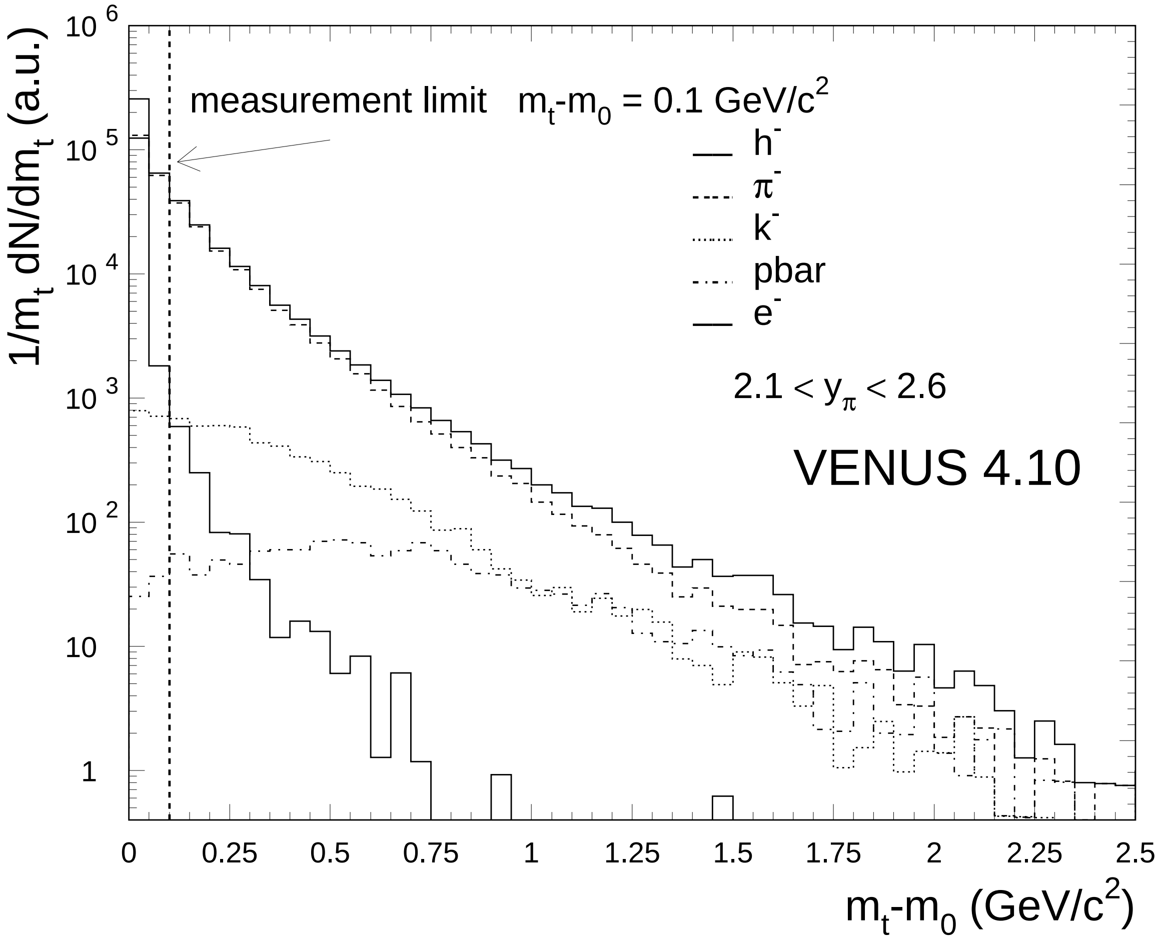

Figure 7.13: Contributions to the h$^-$ spectra from $\pi^-, k^-, \bar{p}, e^-$ obtained with the event generator VENUS. To simulate what happen in the data, for all particles the pion mass has been used to calculate the transverse mass and the rapidity.

Comparing the spectra in Fig. 7.12 no change with centrality is apparent. In Fig. 7.14 (left) the distributions for the central and semi-central interactions are shown on a larger scale. One can notice immediately that the shapes of the spectra are different. For central collision they are more exponential than for semi-central collisions. This is even more evident in the ratio of the two spectra (Fig. 7.14 (right)), where an effect of 20% is visible going from 0.1 to 1 GeV/c^2. Note that in this range the contamination from kaons and antiprotons is small.

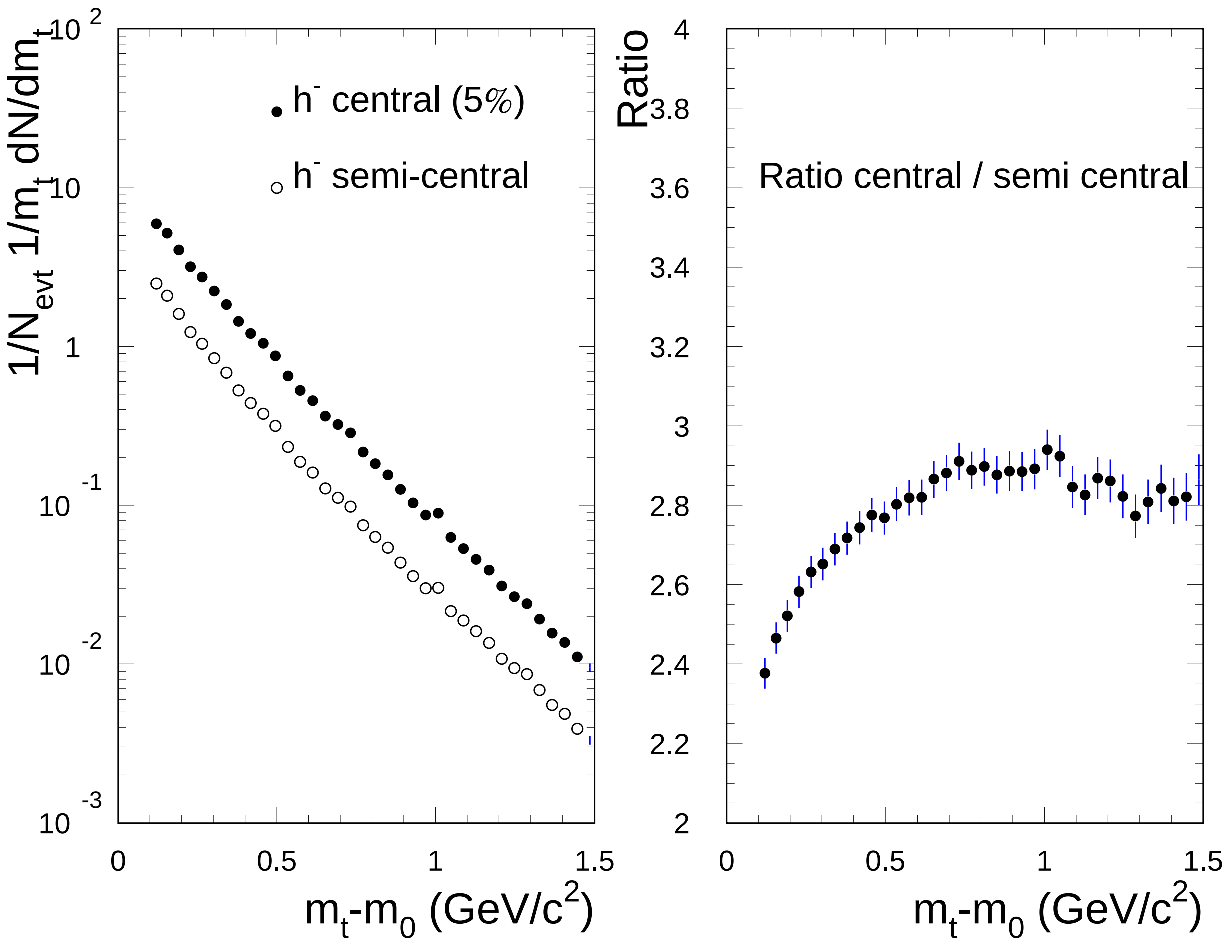

Figure 7.14: Comparison between spectra corresponding to central and semi-central collisions (left) and ratio of the two distribution (right).

The h^- distributions have been investigated also by other experiments. For example NA49 [54] has measured the h^- distribution in central Pb-Pb collisions under nearly identical conditions. The comparison between the two measurements is presented in Fig. 7.15, where the data are arbitrarily normalized at $m_t - m_0 = 0.6$ GeV/c^2. The agreement is remarkable.

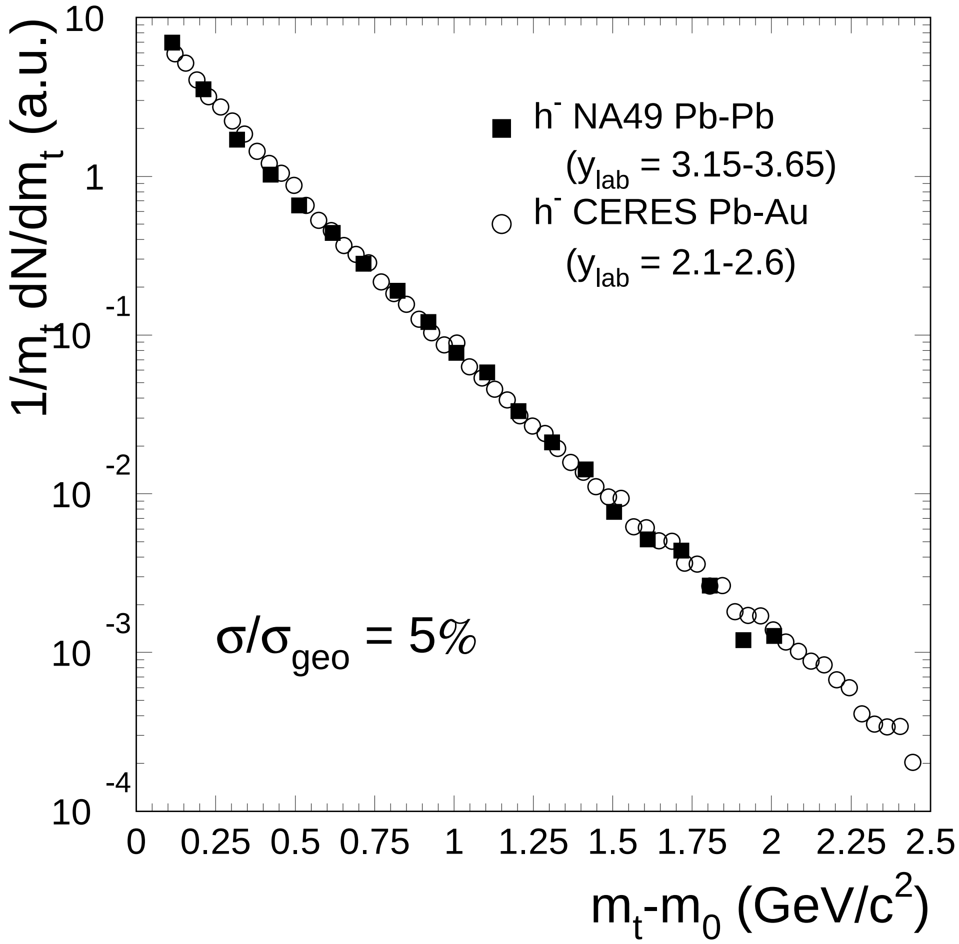

Figure 7.15: The CERES h^- spectra for the central collision ($5\%\sigma_{geo}$) are compared with the results obtained by NA49.

NA49 has applied corrections for electron misidentification, products of secondary interactions and decays. In NA49, the largest influence on the primary h^- distributions comes from the decays $\Lambda \longrightarrow p + \pi^-$. In CERES, since every track is required to point to the vertex and to have a good match to both SDD detectors, the secondary interactions and the decay contributions are below 1% and no correction is necessary.

7.6 Positive Charge Excess $h^{+} - h^{-}$

For CERES, the statistical analysis permits a way to extract the transverse mass distribution of the positive charge excess $h^{+} - h^{-}$ which is closely linked to the net-proton spectra. This quantity has often been extracted in the past from other experiments, having no possibility to identify the protons directly.

As for the h^{-}, the $h^{+} - h^{-}$ distributions are studied as a function of centrality. As the most representative, the transverse mass distributions for semi-central collisions, which correspond to an impact parameter of about 8 fm (Fig. 7.16), and for central collision (b $<$ 2.2 fm) are presented (Fig. 7.17). (The remaining spectra covering the other centralities are shown in Appendix B.)

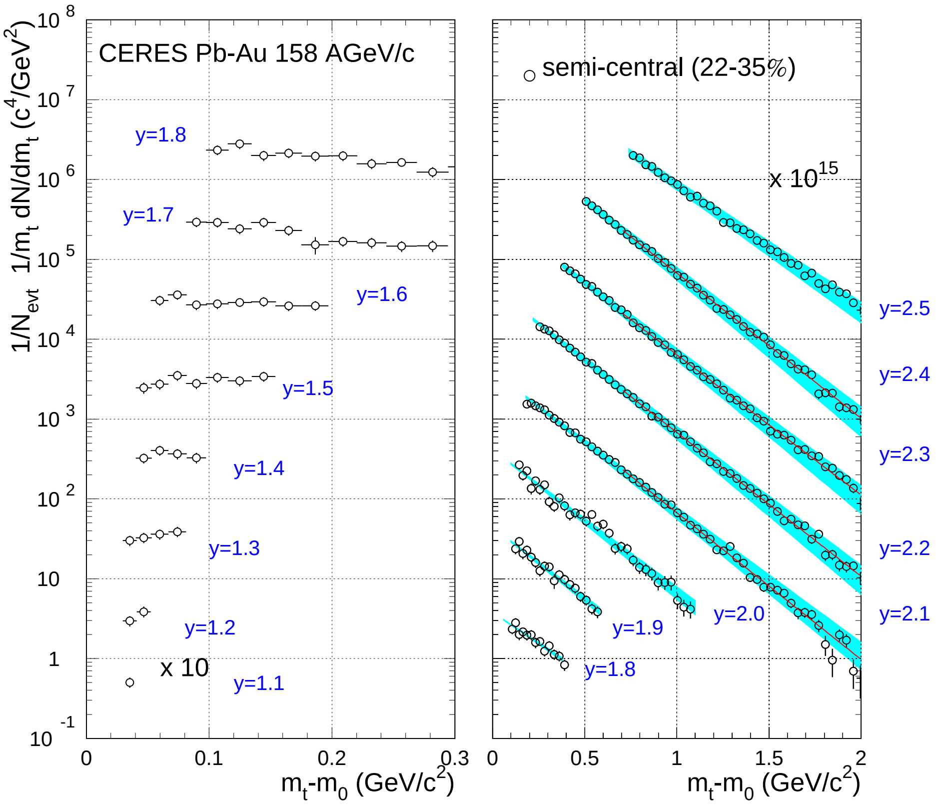

Figure 7.16: $h^{+} - h^{-}$ transverse mass distributions (semi-central). The spectra, corresponding to different rapidity (Δy = 0.1), are successively multiplied by a factor of 10.

All the corrections, which have been previously described, are applied to the raw $h^{+} - h^{-}$ spectra. The azimuthal symmetry of the spectrometer and the magnetic field does not require to use a different procedure or correction function for positive and negative particles. For $y > 2$ there is no acceptance cut off in p_t (compare Fig. 7.3). In this range the correction functions have been fitted by a smooth curve before application to the data. For smaller rapidity where the spectra are cut off at low and high p_t, no appropriate function has been found to describe the complicate shape of the corrections. Therefore the Monte-Carlo results was used bin by bin without smoothing. This results in a larger scattering of the corrected points due to the limited Monte-Carlo statistics.

Looking at the transverse mass distributions as function of rapidity, one observes that the spectra at smaller rapidity are much flatter than the ones near midrapidity. The effect is opposite to that measured by NA49 [54] which observes a steepening of the spectra with decreasing rapidity. A solution is provided if the change is interpreted as a variation of the spectral shape with $m_t - m_0$ rather than with rapidity. If interpreted in this way, dN/dm_t^2 peaks around 100 MeV/c^2.

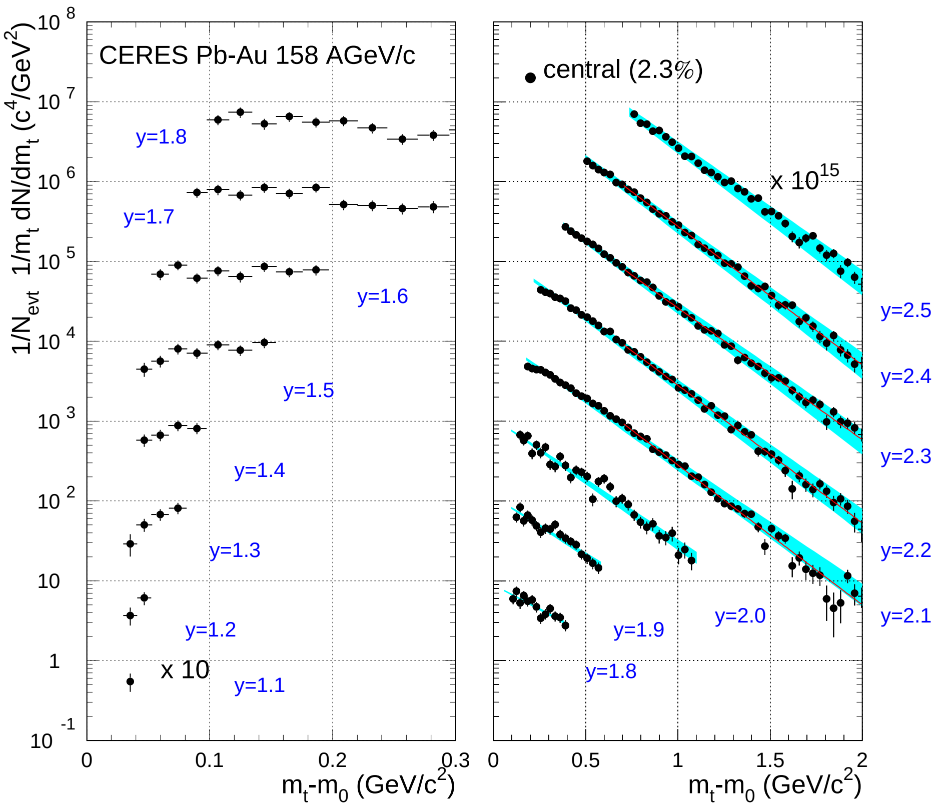

Figure 7.17: $h^+ - h^-$ transverse mass distributions (central).

From the comparison between different impact parameters (Figs. 7.16 and 7.17), one notices that the distributions at higher m_t do not change in shape.

The spectra from y = 2.1 to y = 2.4 have been fitted in the same range in $m_t - m_0$ $(0.7 - 2.\ GeV/c^2)$ with an exponential function of the type:

$$\frac{1}{m_t}\frac{dN}{dm_t} \propto e^{-\frac{m_t - m_0}{T}}$$

In Fig. 7.18, the extracted inverse slope parameters T are presented as a function of the centrality. If one estimates the number of participant A_{part} taking part in the collision from the integrated cross-section, one finds that A_{part} changes by roughly a factor of 3 in our centrality range covered. Surprisingly the inverse slope change only by 5%.

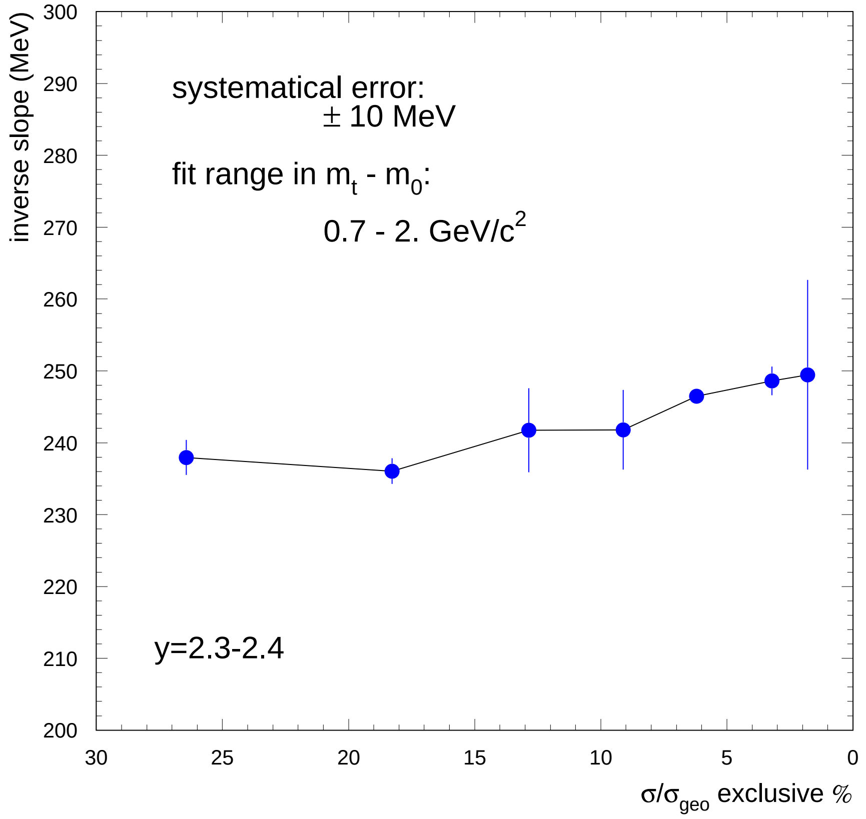

Figure 7.18: Inverse slope calculated for the interval $m_t - m_0 = 0.7 - 2.$ GeV/c^2 near midrapidity ($y = 2.3 - 2.4$).

For smaller m_t a stronger centrality dependence is observed. To illustrate this variation Fig. 7.19 presents the ratios of the distributions corresponding to progressively increasing centrality (from M2 to M7, taking as a reference M1) for the rapidity interval around $y = 1.9$. A significant change is observed. A shift in the maximum of the dN/dm_t^2 distribution to higher m_t with increasing centrality would give a natural explanation.

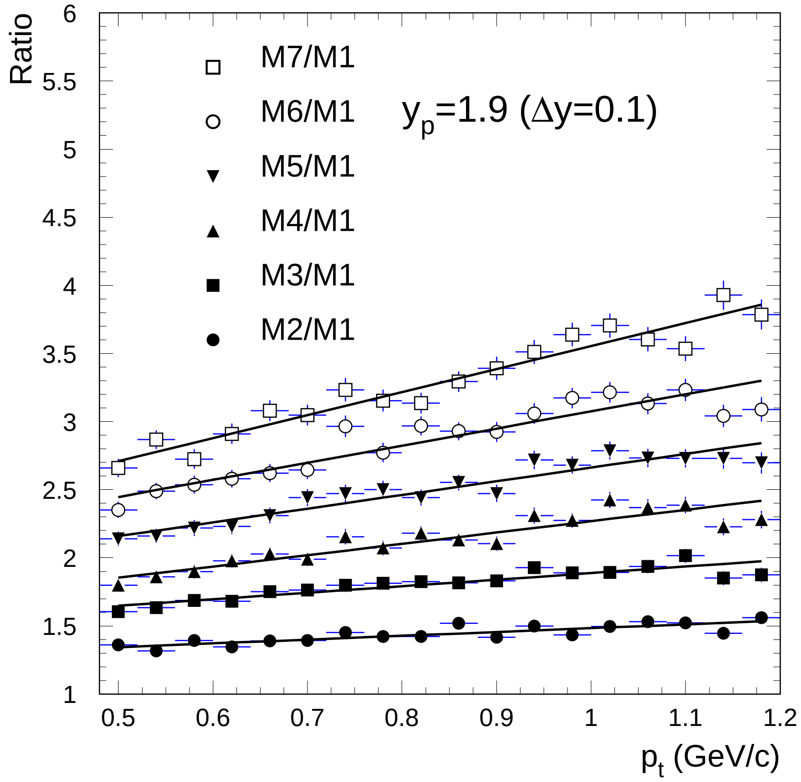

Figure 7.19: Relative ratio of the transverse mass distributions (y = 1.9) for different centrality selections (see text).

One should point out that in the region of overlap our data are in perfect agreement with other experiments. A comparison of the CERES spectra with NA44 [55] and NA49 [54] is shown in Fig. 7.20. Notice that different quantities are measured: NA44 shows identified protons at $y_{lab} \sim 3$ and NA49 uses also the $h^+ - h^-$ method but corrects the spectra for the imbalance between the K^+ and K^- yields and for protons originating from the decay of Λ particles according to VENUS. These differences however are small as one can judge from the good agreement of the data.

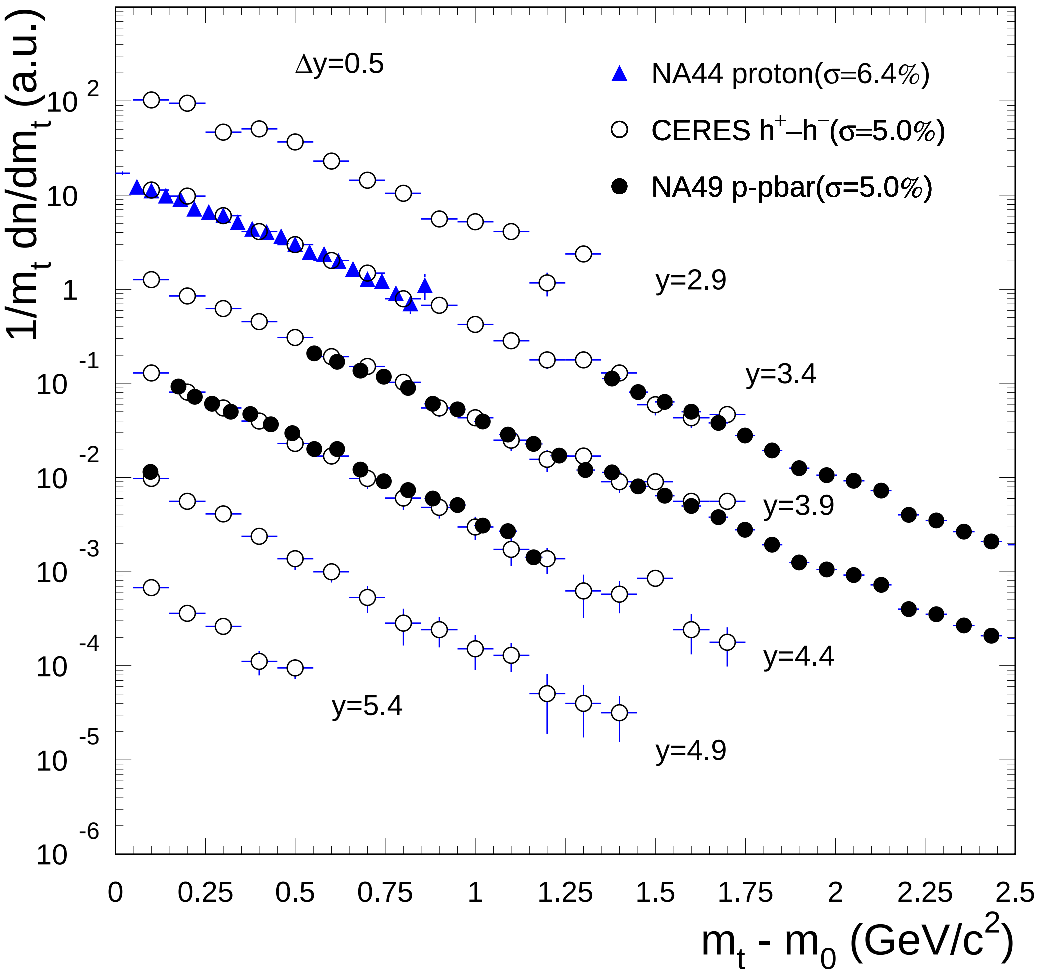

Figure 7.20: Comparison with other experiments.

Independently of the above observation, the question, how far and to what extent the CERES $h^+ - h^-$ spectra do resemble the net-proton spectra is addressed. In Fig. 7.21, for the most central collisions (2.3% σ_{geo}), the different contributions to the $h^+ - h^-$, near midrapidity, are shown for RQMD (top) and VENUS (bottom). In addition to the $p - \bar{p}$ component, one can distinguish two other contributions: (i) the $K^+ - K^-$ unbalance and (ii) the difference between the π^+ and π^- yield caused by the strong isospin asymmetry of the Pb-Au system ($\pi^- - \pi^+$ is plotted as a dashed line). In VENUS, the $K^+ - K^-$ (positive yield) is quite balanced by the $\pi^+ - \pi^-$ (negative yield) such that the net-proton $p - \bar{p}$ coincides with the $h^+ - h^-$. For RQMD in contrast the much higher production of K^+ results in an 30% enhancement of the $h^+ - h^-$ particularly at small $m_t - m_0$.

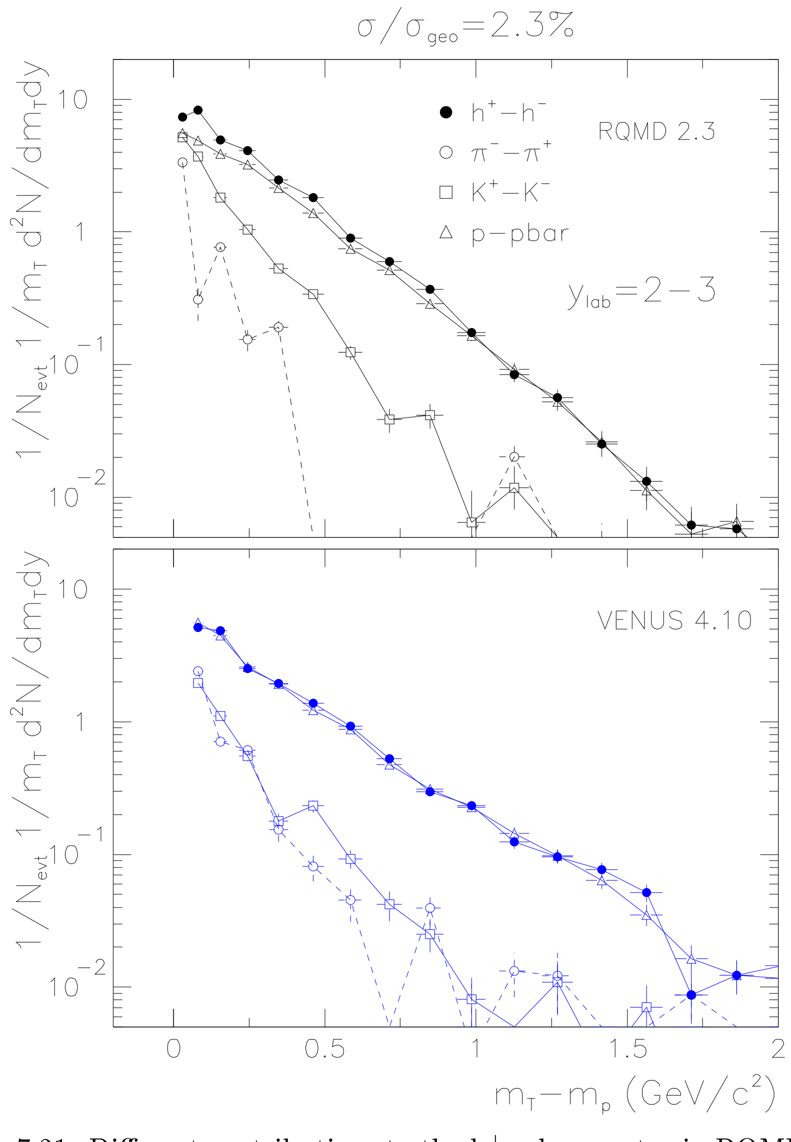

Figure 7.21: Different contributions to the $h^+ - h^-$ spectra in RQMD and VENUS. The rapidity and the $m_t - m_0$ have been calculated assuming for all particles the proton mass.

Among the other contributions which could modify the measured spectra, in particular the decay $\Lambda \longrightarrow p + \pi^-$ should be taken into account. Since the Λ is a neutral particle, no signal of its passage is left in the two SDD detectors. So, even if the proton will mainly conserve the direction of the mother particle and it will point to the vertex, only the decays before the first SDD will influence the $\mathrm{h}^+ - \mathrm{h}^-$ distributions. Knowing the rapidity dependence of the γ factor (full line in Fig. 7.22) and the Λ life time ($\mathrm{c}\tau = 7.89$ fm), the fraction of decays in the space between target and first SDD ($\sim$ 10 cm) can be easily calculated (dashed line in Fig. 7.22). The contamination of the net-proton spectra (Fig. 7.22 (right)) was estimated using the the $\Lambda - \bar{\Lambda}$ and $p - \bar{p}$ yields measured by NA49 [53]. Due to the fact that the calculation of the γ factor is done for $\mathrm{p_t} = 0$, the value of 7% near midrapidity represents an upper limit and the contamination of proton from Λ decays is negligible compared to other systematical errors.

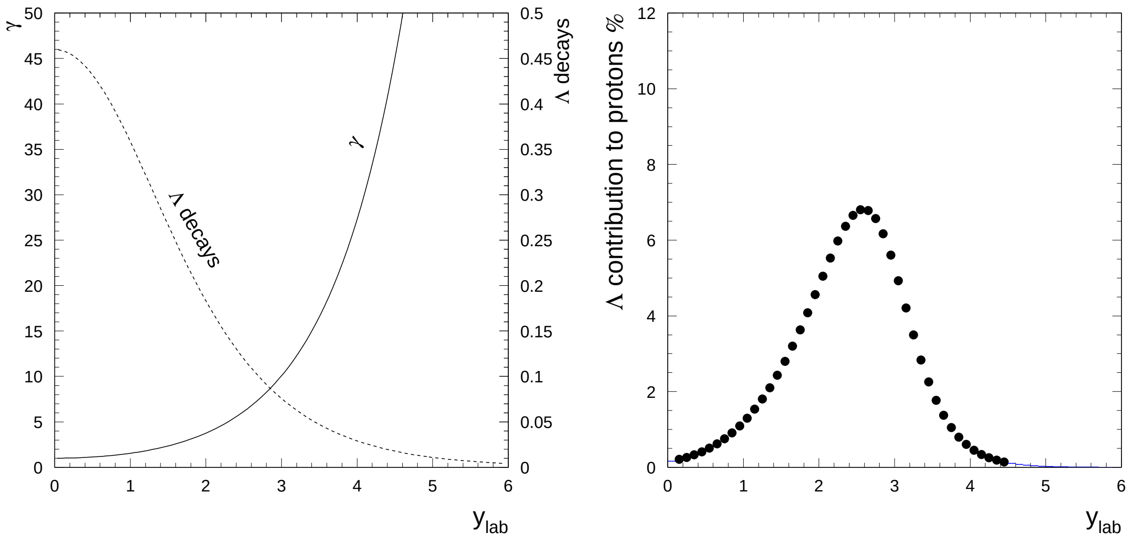

Figure 7.22: The rapidity dependence of the γ factor for $p_t = 0$ (full line) and the fraction of Λ decays before the first tracking detector (dashed line) are presented on the left side. On the right plot, the upper limit for the Λ decays contribution to protons yield is shown.

7.6.1 $h^+ - h^-$ Rapidity Distributions

Integrating the $h^+ - h^-$ spectra permits to calculate the rapidity distributions and study its dependence on the centrality. Since CERES does not measure the complete $h^+ - h^-$ yield, an extrapolation of the transverse mass distribution to low m_t has to be done. The observation that the spectra at low transverse mass are much flatter than at at higher $\mathrm{m_t}$, is taken into account trying to describe the distributions by two exponential components of inverse slope $\mathrm{T_{low}}$ (low m_t) and $\mathrm{T_{high}}$ (high m_t). The rapidity change of $\mathrm{T_{low}}$ and $\mathrm{T_{high}}$ is taken from the models and confirmed, for central collisions, also by the NA49 experiment [35]. Fig. 7.23 shows the change of the inverse slope constant as a function of rapidity.

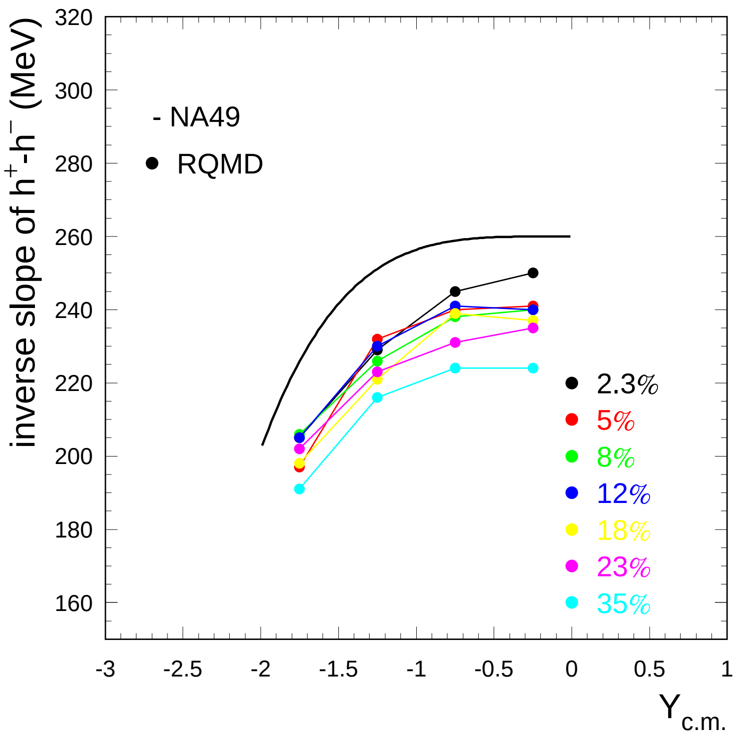

Figure 7.23: Inverse slope parameter as a function of the center of mass rapidity. Points are the model for different centralities and the line is a parameterization of the NA49 data.

If one concentrates on the shape, the points, obtained by RQMD for different centralities, show the same dependence as the NA49 measurements (full line). For the further analysis it is assumed that **both** T_{low} and T_{high} follow the same parameterization:

$$\mathrm{T_{low,high}(y) = T^{max}_{low,high} \cdot (1 - F \cdot y^4_{cm})}$$

where the $F = 0.014$ is taken from the NA49 data and the $T^{max}_{low,high}$ is obtained by fitting the data in the range $m_t - m_0 < 0.7\ GeV/c^2$ and $m_t - m_0 > 0.7\ GeV/c^2$

respectively[4] (Fig. 7.24).

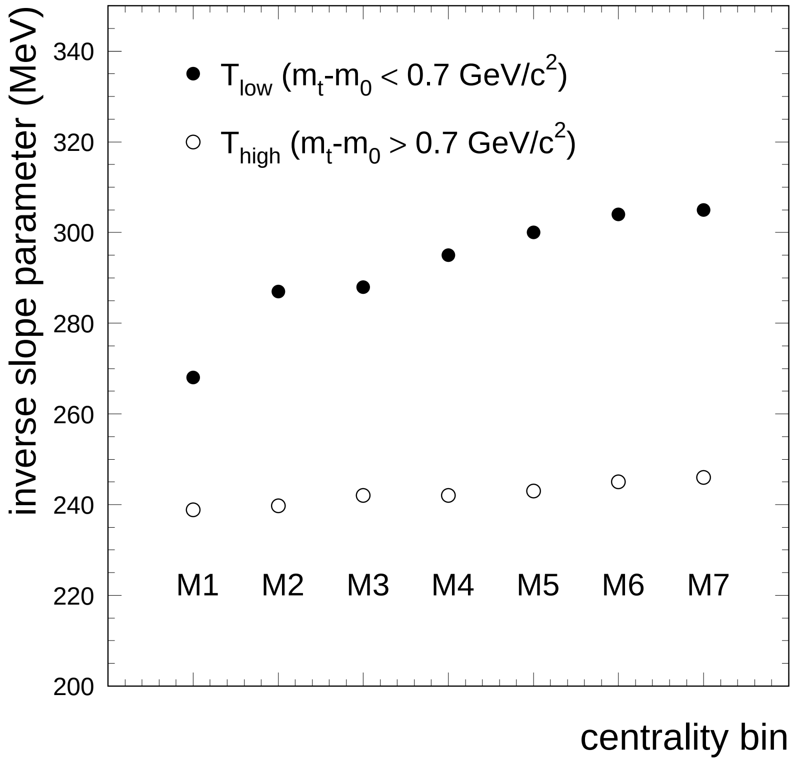

Figure 7.24: Multiplicity dependence of T_{low}^{max} and T_{high}^{max}.

In this way, knowing the shape of the distributions of all spectra corresponding to the different rapidity bins, the yield can be extrapolated. Here one wants to point out that even if the number of measured points is small (as for low m_t), the yield is well fixed by the data. On the other side, for the spectra measured only at high m_t, the extrapolation gets large (about 50% of the yield is extrapolated at y = 1.8 and 85% at y = 2.4).

The CERES data for three centrality selections are presented together with the data from NA49 [35] and NA44[55] in Fig. 7.25, where closed points indicate the measured values and open ones are obtained by reflection around midrapidity (y = 2.9). The rapidity distribution measured by CERES is similar to the NA44 one. NA49 measures a distribution of similar shape. The somewhat lower value of the dN/dy might indicate a difference in the centrality selection and/or in the correction of the data. Comparing different centrality one observes the increase of the number of 'protons' at midrapidity. This increase is well in line with the expected increase of number of participants corresponding to a decreasing impact parameter. In general the shape does not change very much with centrality how-

[4] Also RQMD shows the same trend as a function of the centrality.

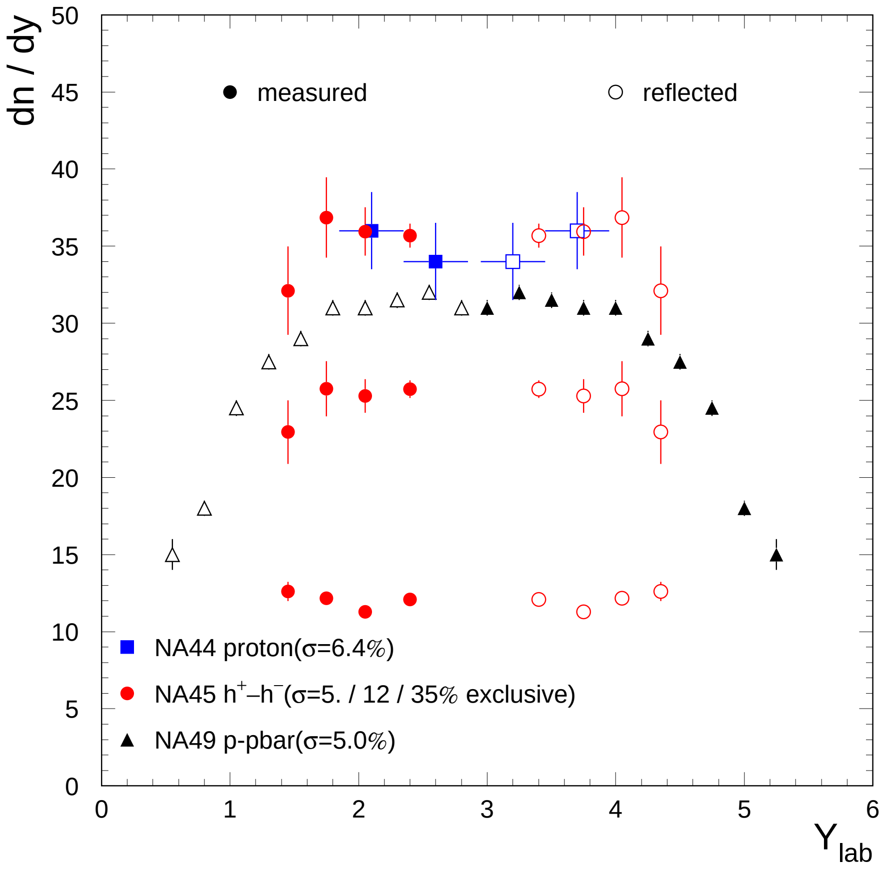

Figure 7.25: Rapidity distributions of the $h^+ - h^-$ and comparison with other experiments.

ever, the systematic errors due to the extrapolation are too large to draw definite conclusions.

Chapter 8

Identified Pions

If particles exceed the Cherenkov threshold in the RICH detectors, they can be identified. Therefore positive and negative pions can be measured for $p > 4.5\ GeV/c$. In this chapter the identification schema and the subtraction of background contributions as well as all necessary corrections will be discussed. As in the previous chapter the transverse momentum spectra, corrected for efficiency and momentum resolution, are presented as a function of the centrality.

8.1 e/π Separation

Positive and negative pions are identified by the size of the Cherenkov ring radius. The particle momenta are calculated through the equation 4.1:

$$p = \frac{m\gamma_{th}}{\sqrt{1 - (\frac{R}{R_\infty})^2}} \tag{8.1}$$

The azimuthal deflection $\Delta\phi$, used previously as a momentum measurement for charged particles, is employed only to determine the electric charge of the particle and to separate pions from electrons.

The ring radius R will reach the asymptotic limit R_∞ for very high velocities (Lorenz factor). In the region (p > 20 GeV/c), the separation between π and e is difficult. In Fig. 8.1 (left), the correlation of ring radius and azimuthal deflection is displayed. The electron component, artificially enriched of a factor 20, is clearly visible close to the asymptotic ring radius $\mathrm{R} = \mathrm{R}_\infty \sim 16$ pads. Differently from pions, electrons and positrons in our momentum range do not exhibit any correlation between $\Delta\phi$ and radius. The consequence is that the e^+e^- component is restricted to a small region of the plane which correlates ring radius and particle momentum calculated from the azimuthal deflection (Fig. 8.1(right)). In both plots, the

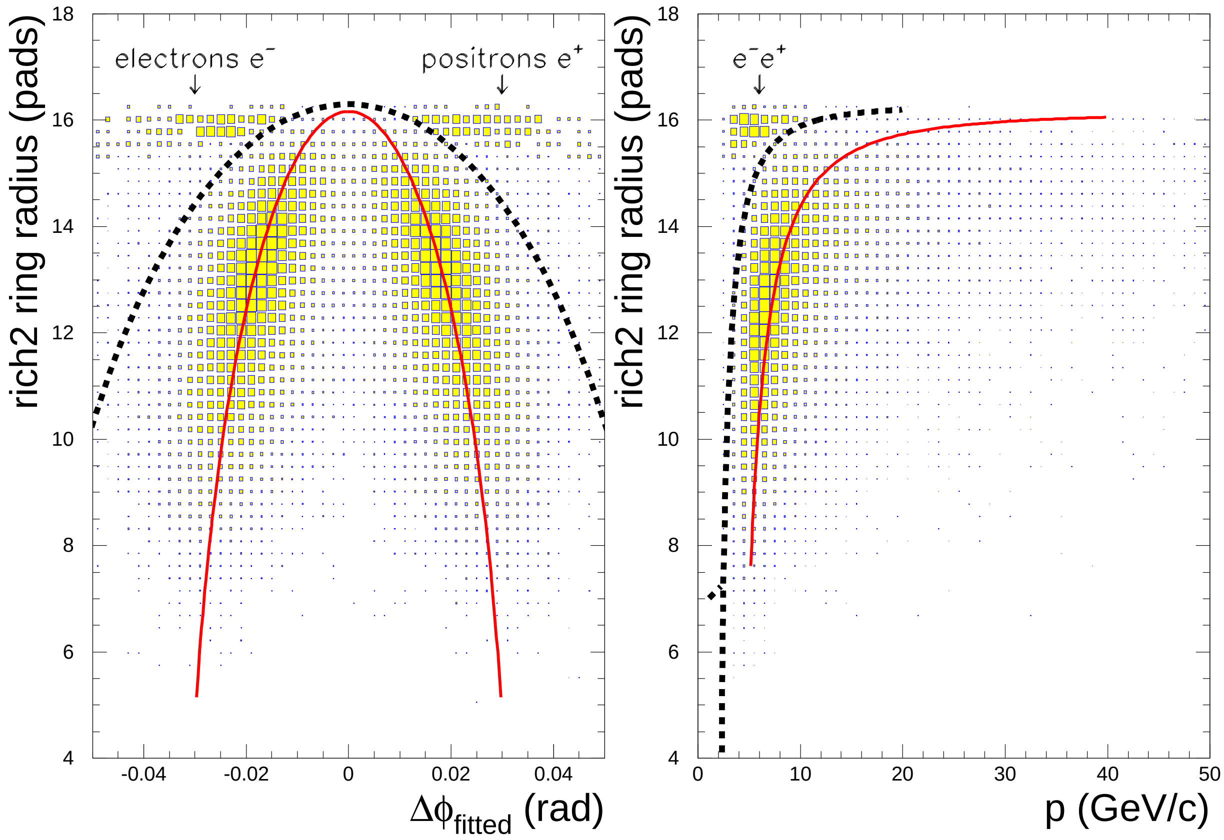

Figure 8.1: Correlation of ring radius and azimuthal deflection with an artificially enriched electron background (20 times).

dashed line indicates the cut used to discriminate the electron background from the pion signal.

The rather homogeneous continuum observed in this figure is mostly caused by the photon conversions or π^0 Dalitz decays where the two closely overlapping rings from e^+ and e^- allowed a false reconstruction of a ring of smaller dimensions, which eventually is misidentified as a pion.

8.2 Background Analysis

To analyze in a systematical way the momentum distribution of the identified pions, one has to correctly estimate the different background contributions to the spectra. Two main categories of background can be distinguished. The first one is a *fake track* component, also defined as *random* background. Into the second category falls the background which has a *physics* origin: for example electrons not removed by the e/π separation cut.

This background originates from different types of reconstructed tracks. Firstly electron tracks which have very high momenta are distinguished from the one that have a smaller one. The former, which are less probable, are *completely* reconstructed and have exactly the same signature as the pions (Fig 8.2). The latter produce a pion-like signal in the detectors before the field but are then stronger deflected because of their low momentum. Even though they have a *physics* origin those *partially* reconstructed tracks (before the magnetic field) are matched with a fake segment after the field and therefore are studied as a normal fake component (Fig 8.2). Slightly open conversions and π^0 decays constitute also, as already mentioned, a possible source of background.

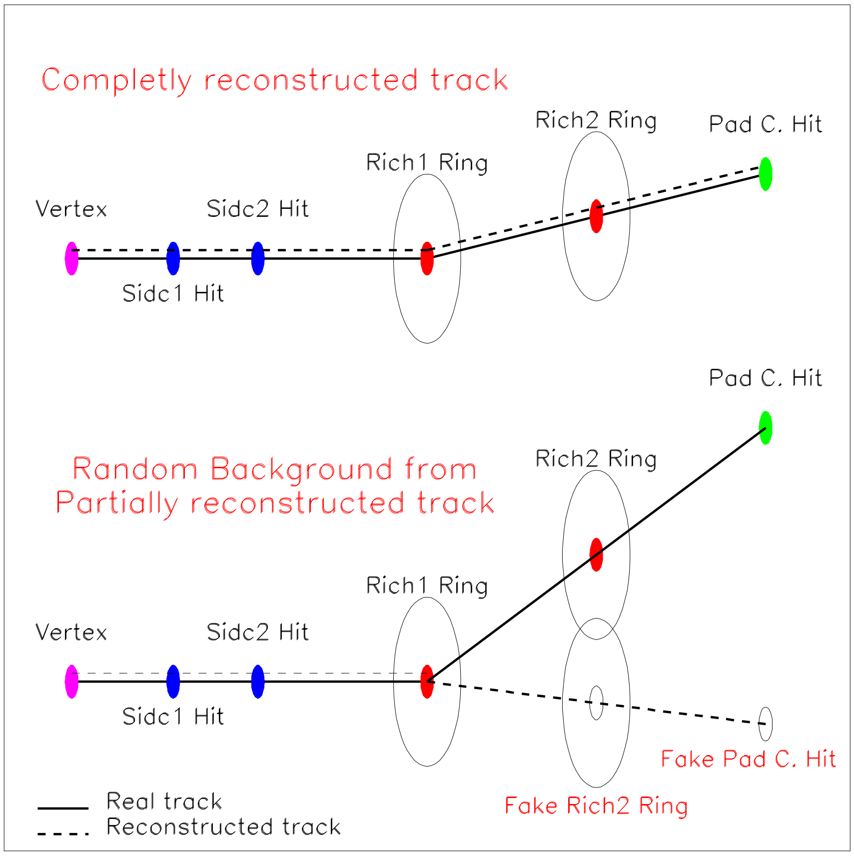

Figure 8.2: Completely and partially reconstructed background tracks.

The influence of the random background is studied using the same technique of detector rotation already described in chapter 6 but now adapted to the new situation. Since the system is comprised of several components, care needs to be

	SDDs	Rich1	Rich2	Pad Chamber
1	0	$\pi/2$	π	$3\pi/2$
2	0	$\pi/2$	π	π
3	0	$\pi/2$	$\pi/2$	$\pi/2$
4	0	0	π	$3\pi/2$
5	0	0	π	π
.	0	...	...	...
.	...	...	...	...

Table 8.1: Examples of rotation possibilities in a system of 4 detectors.

taken when estimating the fake contribution for rotated or mixed events. The case in which all detectors are rotated independently by different angles sets only a lower limit for the fake track component and it does not reliably describe the real background. In this sense, for example SDD1 and SDD2 should be treated just like one single detector because their information is highly correlated. In Table 8.1, some examples of rotation possibilities in a system of 4 detectors are shown. Most of those underestimate the real background contribution, in the approach chosen here only those detectors, whose information is not directly correlated, are rotated against each others, which means only all the detectors before the field (SDDs and RICH1) are rotated against the ones after the field (RICH2 and Pad Chamber). In this way, the contribution of the pure fake tracks will be estimated together with the background generated by the *partially* reconstructed tracks (Fig 8.2).

The only way to extract the influence of the *physics* background and in particular of the *completely* reconstructed tracks, is via a Monte-Carlo simulation. This procedure includes the following steps:

- A sample of π^o Dalitz decays and γ conversions is generated (using the GENESIS generator [1]).
- GEANT [27] simulates the detector response which is later overlayed onto real events to simulate a realistic environment for these tracks.
- The 'overlay' events are analyzed with the same analysis chain used for the normal data.

To quantitatively estimate the number of π^o Dalitz decays the Monte-Carlo result is scaled by $\frac{\pi^o}{N_{ch}} = 0.46$ [36] and the branching ratio in the channel $\gamma\ e^+\ e^- = 1.198\ \%$. One expects $0.552 * 10^{-2}\ e^+\ e^-$ pairs per charged particle. For γ conversions, the factor $\frac{\gamma}{\pi^o} \sim 2.2$ will give $1.012\ \gamma$ per charged particle.

The number of photons that will convert into e^+e^- pairs can be calculated from:

$$\mathrm{N}_{\mathrm{e^+e^-}} = \frac{7}{9} \cdot \frac{\mathrm{X}}{\mathrm{X_0}} \cdot \mathrm{N}_\gamma$$

where X_0 is the radiation length of the material in the flight path of the photons:

- Conversions in the target ($\frac{X}{X_o} = 0.22\%$) and in the air (0.03%) before SDD1 are suppressed by cutting on the correlation between the amplitudes of the two SDD. In this case, if the pair is still close, a double $\frac{dE}{dX}$ signal in both drift detectors is visible. (The rejection power of this cut is around 60%).
- The conversions in SDD1 (0.27%) can be only partially eliminated by the double $\frac{dE}{dX}$ cut (30%).
- Between SDD2 and in (half of the) RICH1 radiator, a fraction of radiation length of 0.35% gives a probability of $2.72 * 10^{-3}$ to have a conversion. This number should be still multiplied by the probability to find a random hit that matches in SDD1, on average $\sim 20\%$.
- The conversions which happen in the remaining part of RICH1 will not produce enough photon hits and the ring will not be reconstructed.

Those values can be still reduced by the applications of detailed cuts as for example requiring a very tight correlation between ring radius and azimuthal deflection (Fig. 8.1).

In Fig. 8.3, the raw transverse momentum distribution of $2 \cdot 10^6$ identified π^+ and π^-, obtained from the analysis of $10 \cdot 10^6$ events, is compared to the distributions of the *physics* and random background. The *physics* background is negligible while the random background reaches $\sim 10\%$ at $p_t > 5\ GeV/c$.

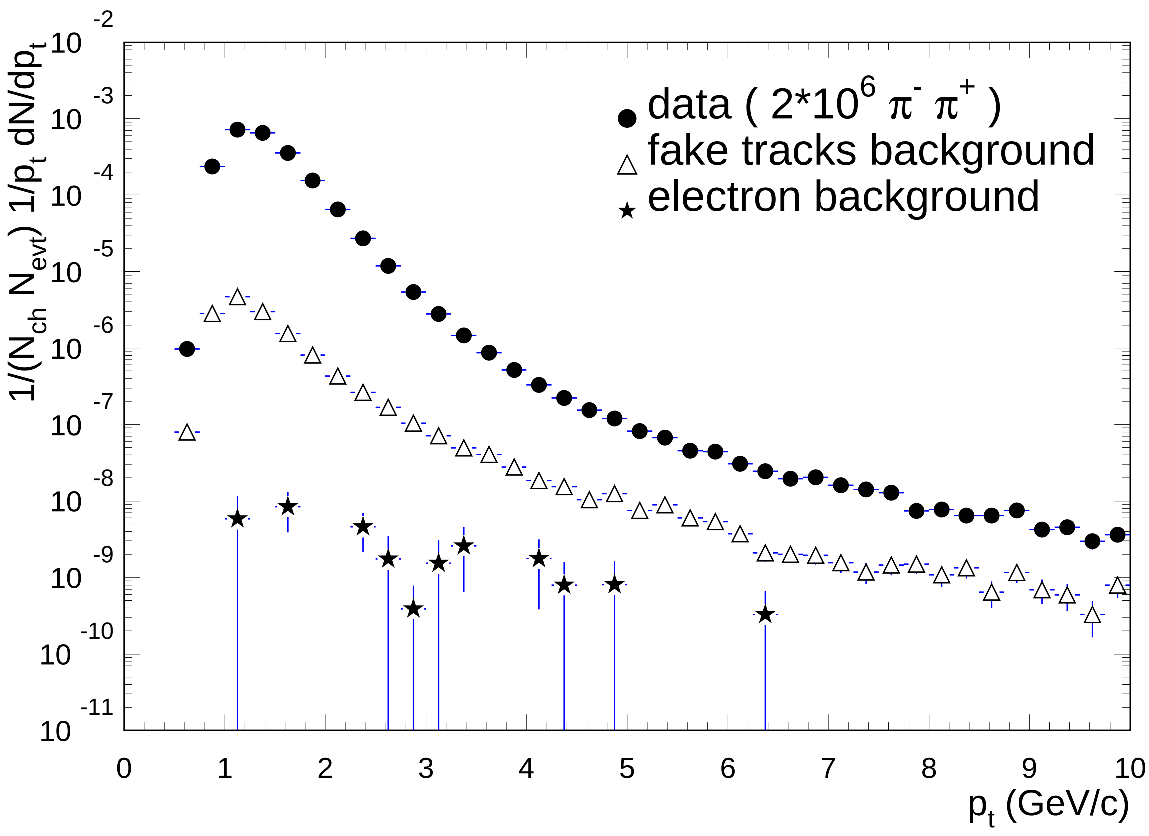

Figure 8.3: Comparison of the uncorrected transverse momentum distribution with the *physics* and random background.

8.3 Correction of the Raw Data

At very high p_t signal and background have similar slopes. The fact that at $p_t = 10\ GeV/c$, there is still a significant pion yield is due to the momentum resolution which produces a smearing of the spectra, moving usually particles from the low (where the yield is higher) to the high momenta.

The effect of the limited momentum resolution of the spectrometer is simulated with a Monte-Carlo simulation. To start the simulation with a realistic momentum distribution one can parameterize the data measured by NA49[54], NA44[55] and WA98[56] (Fig. 8.4). The data was normalized at $m_t - m_0 = 300\ MeV/c^2$.

The curve (dashed line) represents the best fit to the data of the three experiments with three exponential components:

$$\frac{1}{m_t}\frac{dN}{dm_t} \propto 700 * exp(-x/T1) + 240 * exp(-x/T2) + 50 * exp(-x/T3)$$

where x is $m_t - m_0$, and the three inverse slopes $T1$, $T2$ and $T3$ are respectively 75 MeV/c^2, 165 MeV/c^2 and 250 MeV/c^2.

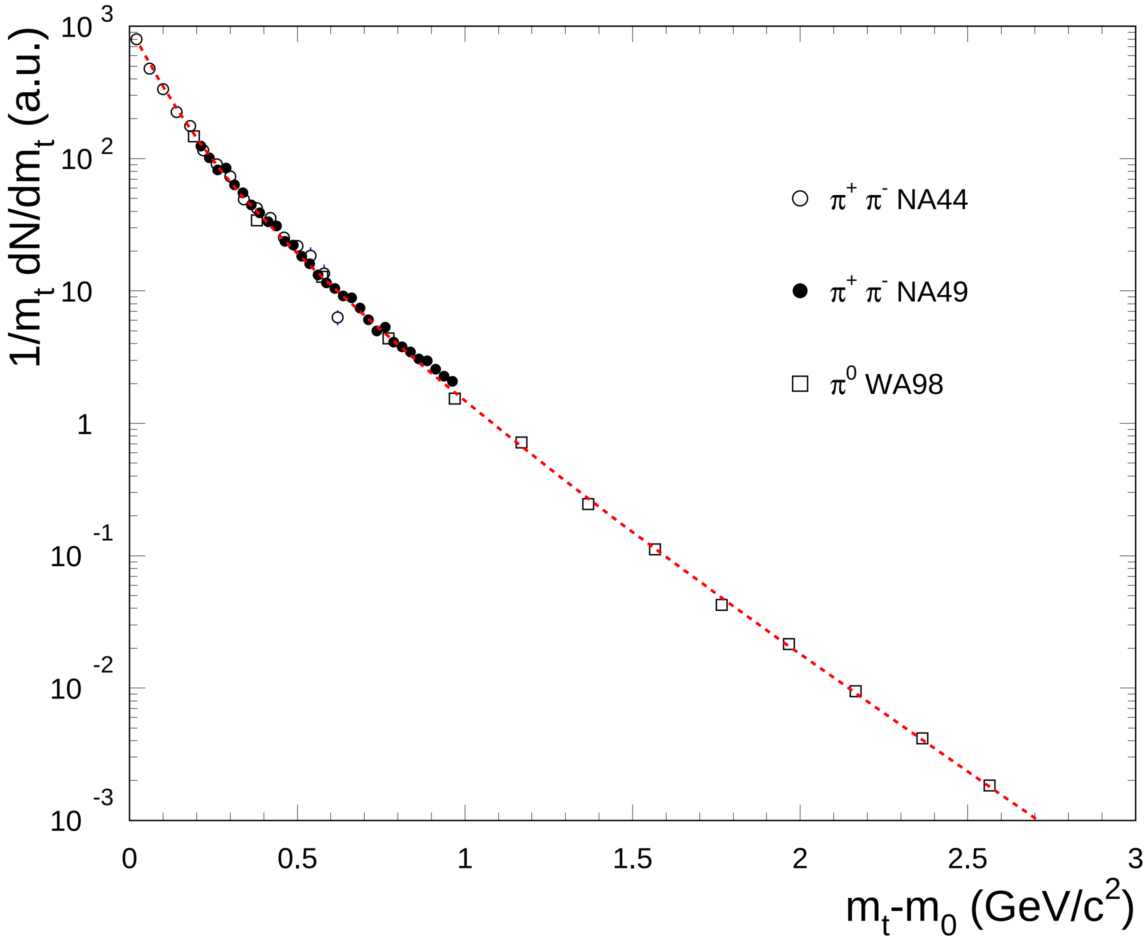

Figure 8.4: Transverse mass distribution of π^0 π^+ $\pi-$ measured by NA44, NA49 and WA98 in Pb-Pb collisions at CERN SPS.

The output obtained by the Monte-Carlo is compared with the background subtracted raw data spectra (Fig. 8.5 (left)). The ratio of the two distributions is presented on the right side of the same figure. As one can see, the agreement between the two spectra is very good. The deviation of about 20% at small $\mathrm{p_t}$ is due to an imperfect Monte-Carlo description in the region of the Cherenkov threshold. This region is very sensible to small gain variations in the two RICH because of the low number of hits which compose a ring.

As usual, the ratio between the Monte-Carlo input and output distributions provides the correction function (Fig. 8.6). The increase above 1 at high p_t is caused by the momentum resolution. The drop below 1 is due to the low number of emitted photons for pions with small momenta.

Since the reconstruction efficiency of the analysis chain as well as the momentum resolution of the spectrometer depend on the multiplicity environment, the

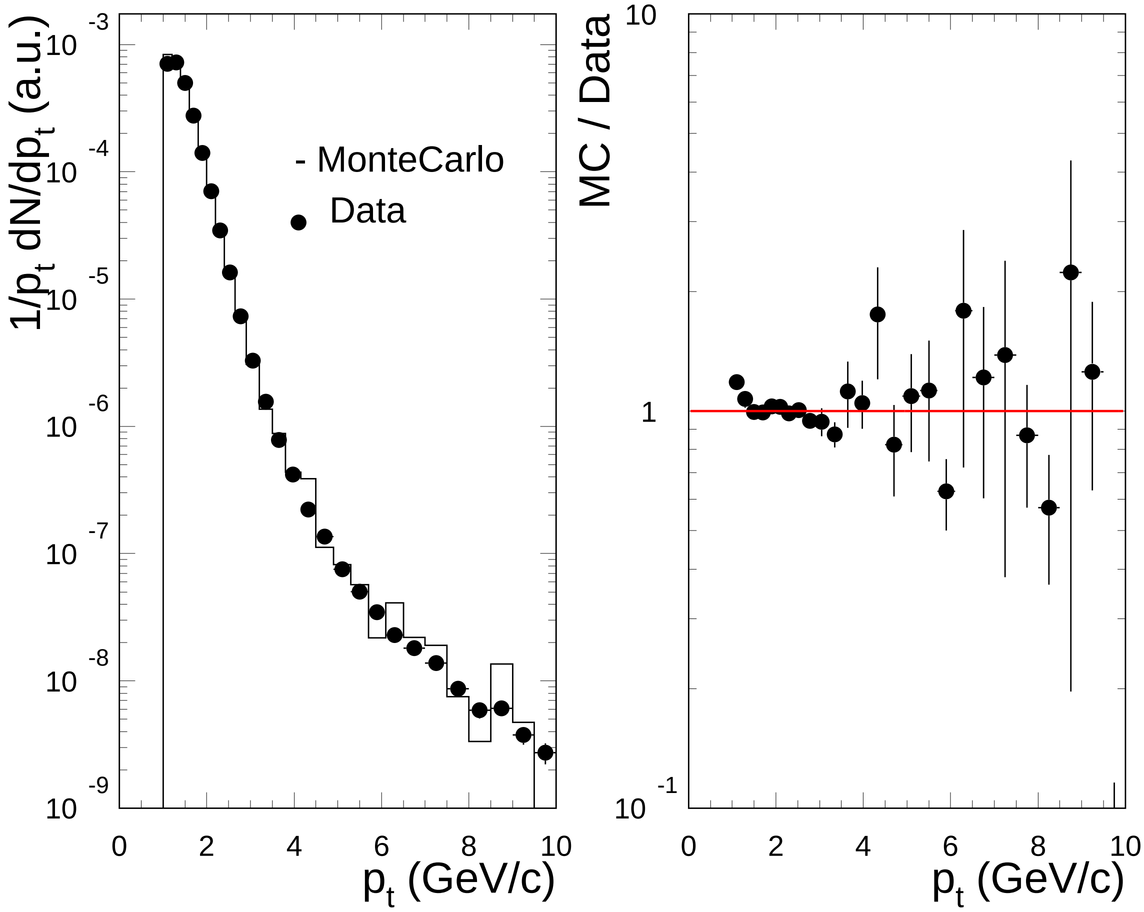

Figure 8.5: Raw data (background subtracted) and Monte-Carlo output.

influence of these effects on the correction function was carefully studied. The variation for two extreme cases (low and high multiplicity) is presented as a shaded area in the same figure. One can observe that, at small momenta, the shape of the function is independent from the multiplicity: only the absolute value changes. Close to the asymptotic ring radius, however, the presence of background hits strongly influences the ring radius resolution, leading to the steep rise of the function at high p_t.

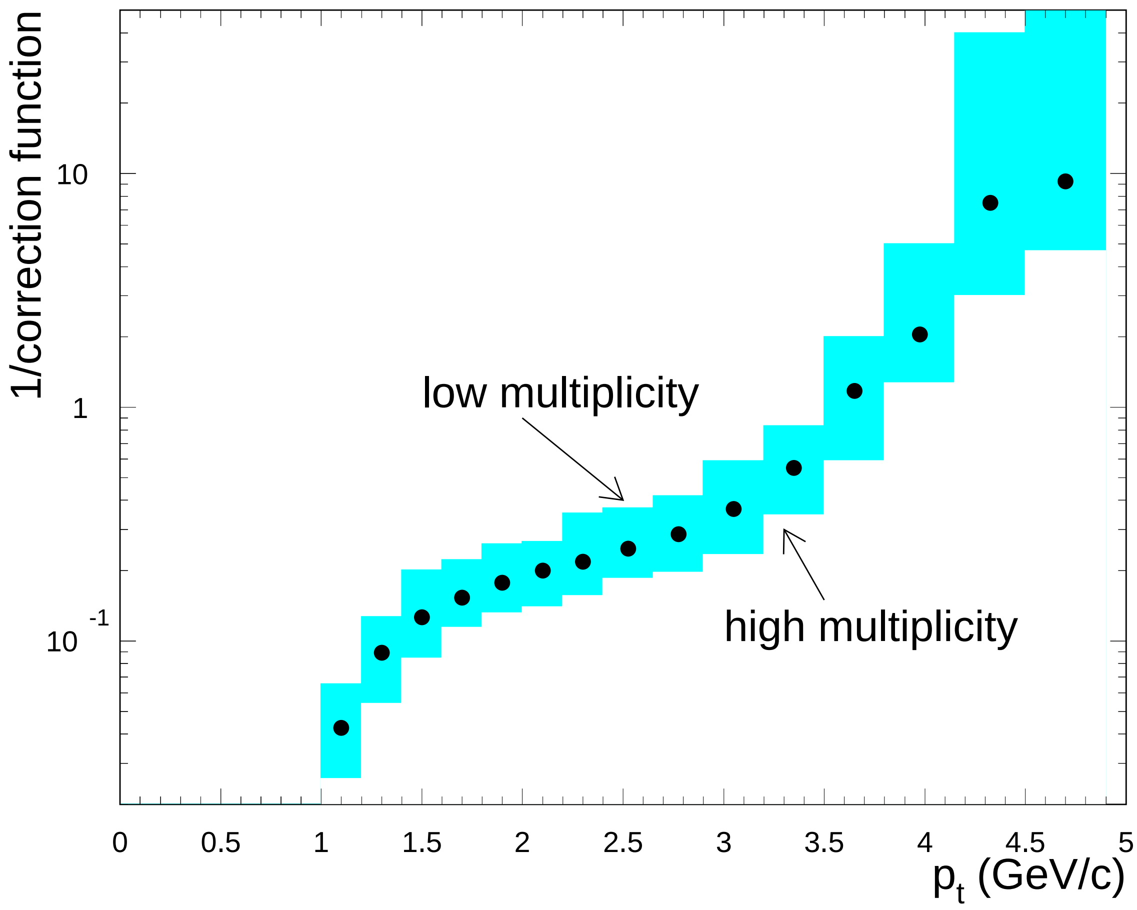

Figure 8.6: Inverse correction function. The shaded area represents the variation of the correction with multiplicity.

8.4 Results

In order to cover the largest possible p_t range the π^+ and π^- distributions are added. The π^+ π^- spectra covering the $m_t - m_0$ range from 1.2 to 4. GeV/c^2 are presented in Fig. 8.7. As for the h^- distribution, the data have been divided into several centrality bins, each of which has been independently corrected for efficiency and momentum resolution. Since the corrections, in particular for momentum resolution, become large at high p_t, the transverse mass distributions are reliable only up to 4 GeV/c^2, where the correction factor varies between 2 to 5 depending on multiplicity.

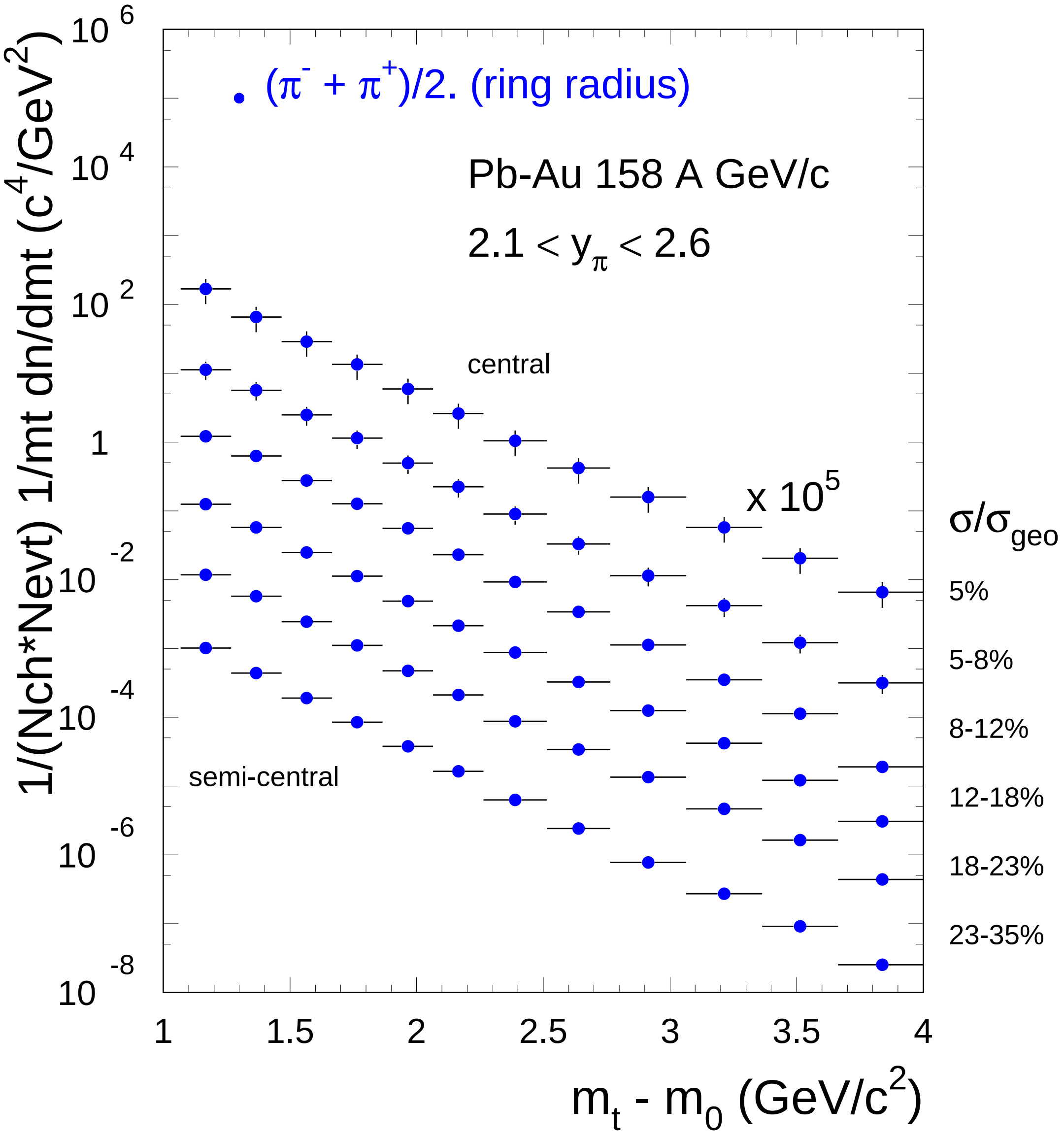

Figure 8.7: π^- π^+ spectra for different exclusive centrality bins.

The systematical errors are mainly given by the accuracy of the ring radius resolution. Close to the Cherenkov threshold, the error is about 30% due to the high sensitivity of the reconstruction algorithm to the gain variation. The uncertainty drops to 10% at $m_t - m_0 = 2$ GeV/c^2 but increases again to about 25% at 3 GeV/c^2 and more than 40% at 4 GeV/c^2 due to the rapid worsening of the momentum resolution.

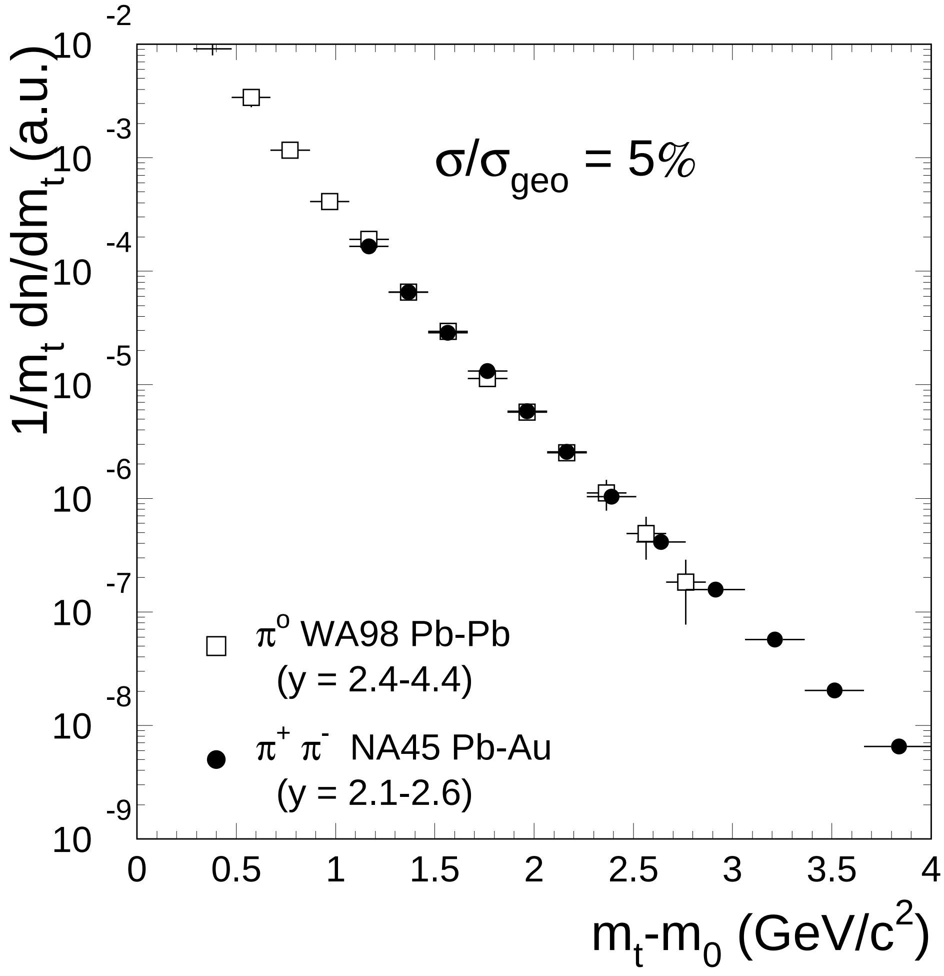

Figure 8.8: The CERES $\pi^- + \pi^+$ spectra for central collision are compared with the results obtained by WA98.

The only other experiment which has measured high p_t pions is WA98. They identify π^0s via their decay: $\pi^0 \longrightarrow \gamma + \gamma$. The comparison of the charged pion spectra obtained by CERES with the neutral ones of WA98 [56] is shown in Fig. 8.8. The two distributions, normalized arbitrarily at 1.3 GeV/c^2, present within the errors a good agreement in the overlap region (1. - 2.6 GeV/c^2).

A separate analysis of negative and positive pions is possible only for a restricted range of momenta. When the $\Delta\phi$ deflection is of the order of the azimuthal resolution of the spectrometer, it is not possible to distinguish between the two different charge signs.

The ratio π^-/π^+ is plotted as a function of p_t in Fig. 8.9. A larger production of π^- with respect to π^+ is observed but the effect is smaller than 5%. The misidentification of positive pions as negative pions (and vice versa) plays a role only at high p_t ($p_t > 3\ GeV/c$). The following table reports the fraction of particles that are wrongly identified as a consequence of the restricted azimuthal resolution of the spectrometer.

p_t (GeV/c)	% misidentification
1.0	0.
1.5	0.2
2.0	1.3
2.5	3.4
3.0	4.5

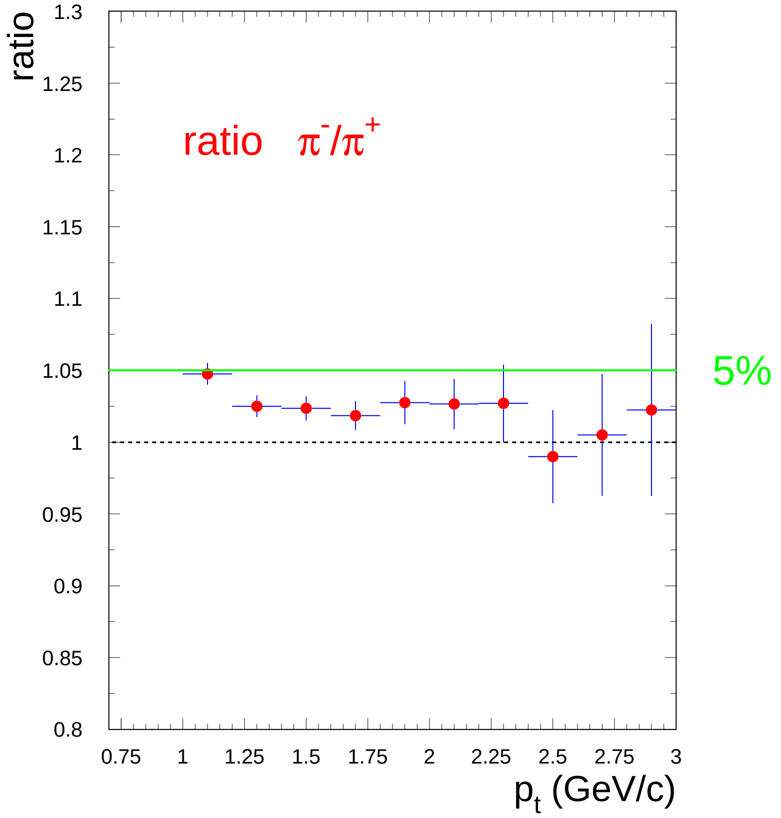

Figure 8.9: Transverse momentum dependence of the π^-/π^+ ratio.

Chapter 9

Discussion and Conclusions

The transverse mass spectra and the charged particle distributions presented in the previous chapters are now discussed and compared with the results obtained in hadron-hadron and hadron-nucleus collision. Through the section the $h^+ - h^-$ distribution are referred as net proton spectra.

9.1 Charged Particle Distributions and Stopping

The pseudo-rapidity density of charged particles consisting mostly of pions and protons, has been presented in chapter 6. The width (σ) of the distribution is around 1.5 rapidity units. This is much broader than for the case of an isotropic thermal source of $T = 160\ MeV$ [51]. The picture, which resembles more that of local isotropic sources equally distributed over a broad rapidity interval about midrapidity, is supporting an high degree of collectivity and in particular an expansion of the system in longitudinal direction [51].

The narrowing of the distribution, observed with increasing centrality is also very interesting. The phenomenon is correlated with an increasing degree of stopping reached in the most central collisions. It provides important information how the incoming energy is transfered into new degrees of freedom. Starting from the charged particle distributions (Fig. 6.5) and the $\mathrm{h}^+ - \mathrm{h}^-$ rapidity densities (Fig. 7.25) it is possible to extract how many charged particles are produced for each proton stopped in the middle of the reaction zone.

Fig. 9.1 shows this value as a function of charged particle multiplicity. Within the errors, which are dominated by the systematical uncertainty in the extrapolation of the 'proton' yield, no change is observed and the ratio remains constant over a wide range in multiplicity, from relatively small sources to the largest ones.

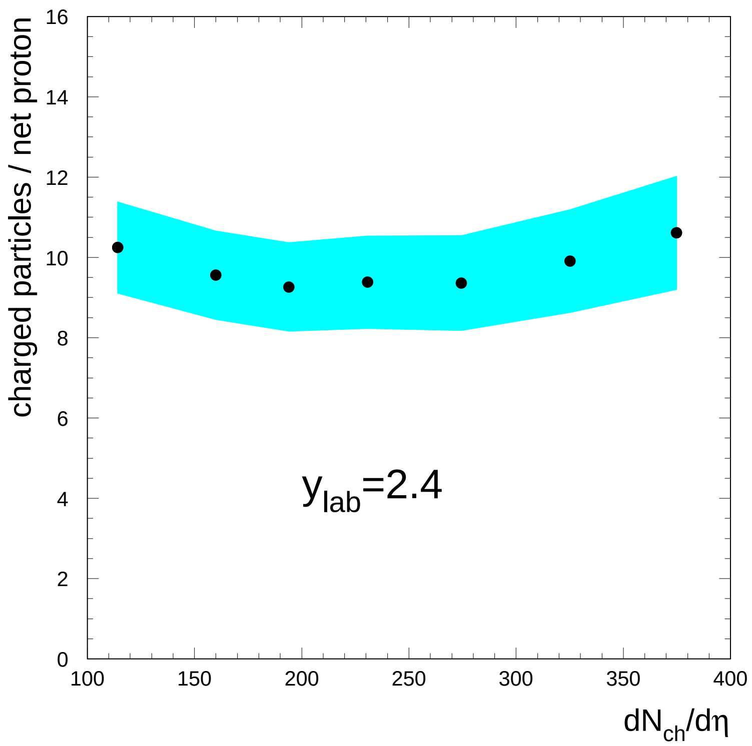

Figure 9.1: Number of produced charged particles per net proton near midrapidity.

9.2 Transverse Mass Spectra

When the negative hadron spectra are combined with the spectra from identified pions, the range of the m_t-spectra measured by CERES is fairly wide: $0.2 < m_t - m_0 < 4\ GeV/c^2$.

Over a limited region, from 1.2 GeV/c^2 to 2.5 GeV/c^2, the two measured spectra, obtained with totally different approaches, overlap and can therefore be compared on an absolute scale (Fig. 9.2). For all centrality selections we obtain a good agreement, proving the consistency of the measurements. The typical concave shape of the pion (or h^-) transverse mass distributions is measured also by other experiments[1]. At small p_t, this is mostly likely due to resonance decays [51, 13], at high p_t, hard scattering processes start to influence the slope of the spectra.

Since it is not possible to describe such spectra with a single exponential, an analysis of the local slope is useful. For central ($\sigma/\sigma_{geo} = 5\%$) and semi-central collisions ($\sigma/\sigma_{geo} = 22 - 35\%$), the local inverse slope T_{loc} is plotted as a function of $m_t - m_0$ in Fig. 9.3. The local slope has been extracted by fitting small consecutive m_t interval ($\pm$200 MeV/c^2 for h$^-$ and $\pm$500 MeV/c^2 for π^-). T_{loc} continuously change from values of about 180 MeV to 250 MeV. At small $m_t - m_0$ (for h$^-$), a difference in shape is seen between central and semi-central interactions. The effect, already noticed in Fig. 7.14, is consistent with distributions becoming

[1]See figure 7.15

more exponential with increasing centrality. For higher m_t, we do not observe any centrality dependence.

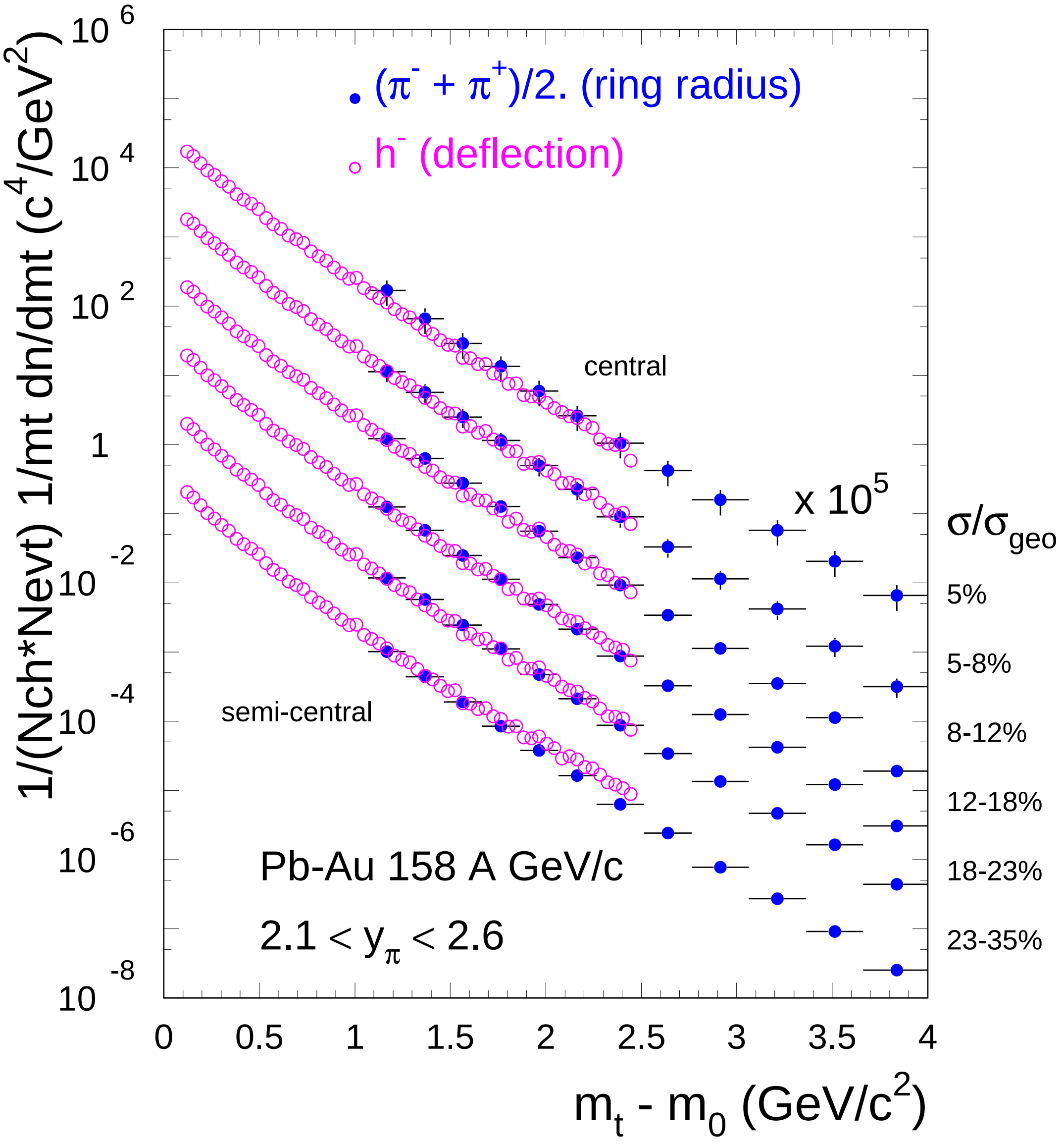

Figure 9.2: π^- π^+ spectra and negative hadrons distributions for different centrality bins.

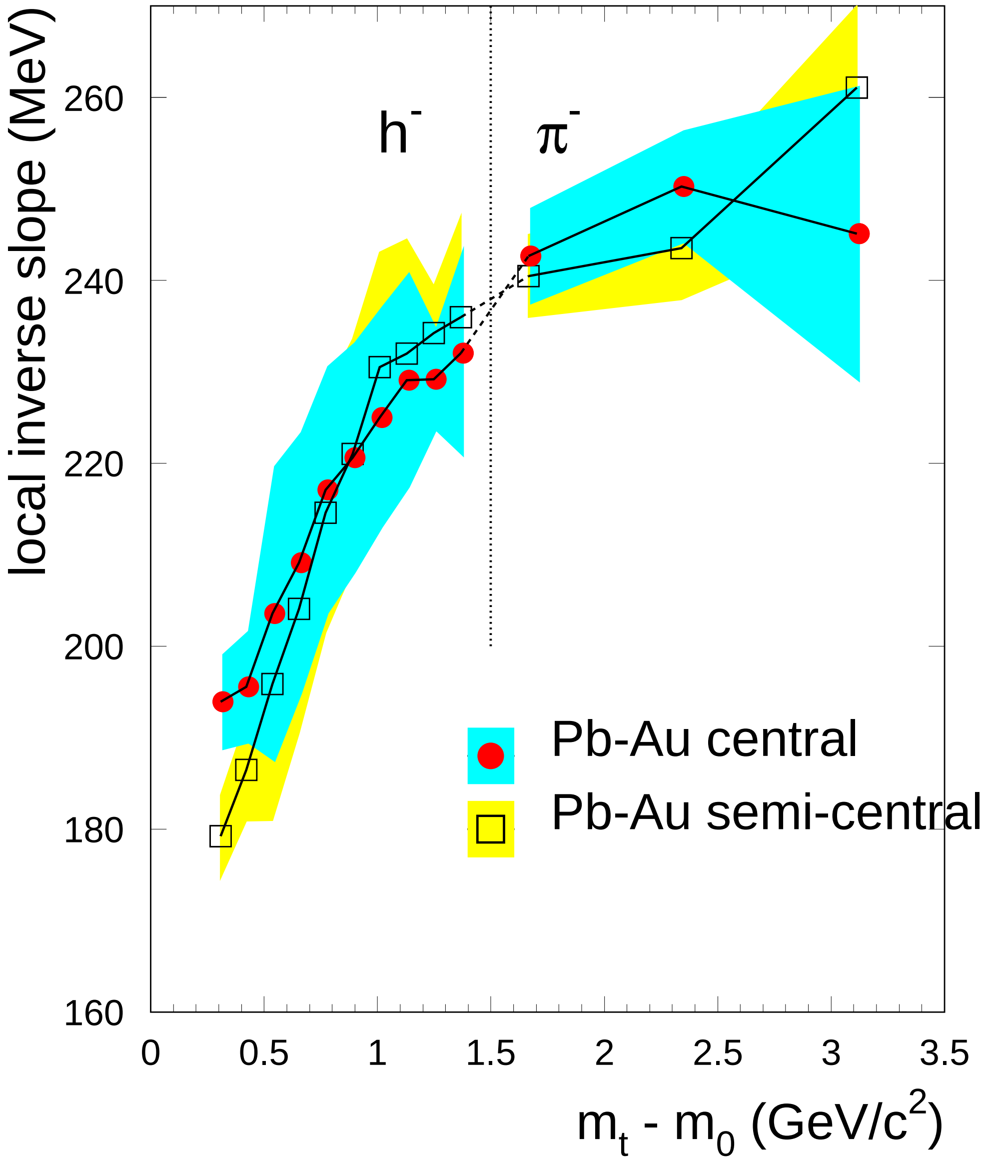

Figure 9.3: Local inverse slope for h$^-$ and π^- as a function of $m_t - m_0$ for two different centralities.

A similar analysis of the net-proton spectra ($h^+ - h^-$), already presented in chapter 7, shows that close to midrapidity, in the interval $0.7 < m_t - m_0 < 2.$ GeV/c^2 a very weak centrality dependence of the inverse slope is noticed (Fig. 7.18). At small m_t (Fig. 7.19), we observe a much stronger change. This change can be interpreted as a shift of the maximum of the dn/dm_t^2 distribution to higher m_t with increasing centrality. However, this interpretation has to be taken with care since the $h^+ - h^-$ spectra can deviate from the net-proton distribution because of increased imbalance between K^+ and K^-, isospin asymmetry in the π^- and π^+ production and Coulomb effects. The influence of those effects, together with the change of the rapidity window with p_t, are difficult to predict. The models are at the present state not reliable enough to permit a quantitative correction.

9.3 Comparison with p-p and p-A Collisions

To investigate the presence of new effects that could hint to a new state of matter reached in heavy ion interactions, one should first compare the spectra to the corresponding distributions measured in nucleon-nucleon and nucleon-nucleus collisions.

The inclusive cross-section of π^- for different center of mass energy $\sqrt{s}$ has been measured at both, the CERN ISR[2] and the Fermi-lab, already more than 20 years ago. Inclusive production of charged pions in proton-proton collisions at c.m. energies from $\sqrt{s} = 23$ to 63 GeV/c over the transverse momentum range 0.1 GeV/c $< p_t <$ 4.8 GeV/c have been precisely measured as a function of the rapidity y by Alper et al. [37], who provide also a convenient parameterization of all data (equation 9.1): the first term is a simple exponential in p_t which describe the low-p_t region and the second term is inspired by QCD and explains the high-p_t part of the spectrum:

$$\mathrm{E}\frac{\mathrm{d}\sigma}{\mathrm{d}\bar{\mathrm{p}}} = \mathrm{A_1 exp(-Bp_t) exp(-Dy^2)} + \mathrm{A_2}\frac{(1-\mathrm{p_t/p_{beam}})^{\mathrm{m}}}{(\mathrm{p_t^2 + M^2})^{\mathrm{n}}} \tag{9.1}$$

where y is the center of mass rapidity and $\mathrm{p_{beam}}$ is the beam momentum. The constants derived from their fit are:

	A_1	B	D	A_2	M	m	n
π^-	205 ± 4	7.44 ± 0.09	0.21 ± 0.01	12.8 ± 0.9	1.08 ± 0.02	13.1 ± 0.4	4.0

The comparison of the data corresponding to the most central collisions to the Alper parameterization is presented in Fig. 9.4 normalized to the charged particle density. One can observe that the transverse mass distribution from proton-proton collisions (full line) is much more concave and steep than our Pb-Au data. We

[2]Intersecting Storage Rings

conclude that the system we are observing is **not just** a simple super-position of independent nucleon-nucleon collisions.

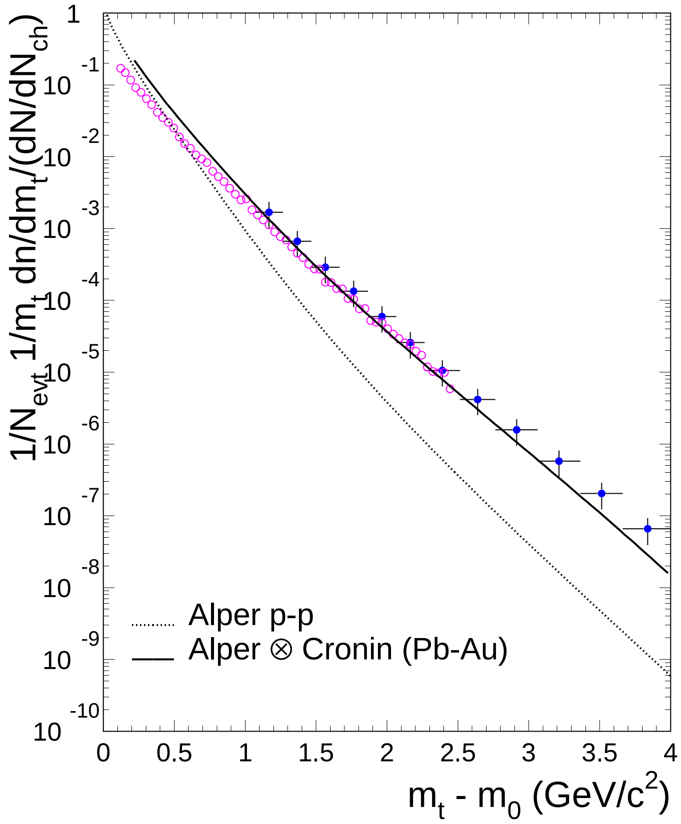

Figure 9.4: Comparison with proton-proton spectra and extrapolation to Pb-Au obtained using the Cronin exponent (see text).

However, also p_t spectra for pA are known to deviate from pp data. The effect, not yet completely understood, was measured for the first time in 1975 and it is known as *Cronin effect* [38, 39, 43, 44, 57]. It describes the nucleon-nucleus (pA) collisions as obtained from the product of the nucleon-nucleon cross-section (σ_{pp}) and a term A^{α}, where A is the target mass and α is a function which depends on p_t such that:

$$\sigma_{\mathrm{pA}} = \mathrm{A}^{\alpha(\mathrm{p_t})} \cdot \sigma_{\mathrm{pp}}$$

A compilation of the α exponent is presented as a function of p_t in Fig. 9.5 [43, 44, 39, 57]. One has to notice that Cronin [39] and Garbutt [43] measure proton, Chaney [44] neutron, while Frisch [57] and E706 π^- induced collisions. The values range from 0.8 to 1.15: an α larger than 1 suggests that the nucleons in the target and projectile act in some collective way. From the plot, we observe that even though Frisch and E706 observe a steeper rise of the α exponent with respect to Cronin, at higher p_t all the measurements are consistent. Since Cronin and Garbutt have very small errors, the fit of all data is dominated by those measurements.

Here we report the parameter of the polynomial fit (7 grade in p_t (GeV/c)) we have performed in the range $0.2 < p_t < 6$ GeV/c:

Order	coefficient	error
0	0.83263	$0.27163\ 10^{-2}$
1	$-0.67039\ 10^{-2}$	$0.26333\ 10^{-2}$
2	0.16769	$0.85350\ 10^{-3}$
3	-0.10464	$0.18030\ 10^{-3}$
4	$0.32671\ 10^{-1}$	$0.34555\ 10^{-4}$
5	$-0.56964\ 10^{-2}$	$0.63251\ 10^{-5}$
6	$0.51363\ 10^{-3}$	$0.10368\ 10^{-5}$
7	$-0.18419\ 10^{-4}$	$0.12499\ 10^{-6}$

Successive measurement of pW, OW and SW collisions [40, 41] showed a similar behavior also for the projectile B:

$$\sigma_{\mathrm{AB}} = \mathrm{B}^{\beta(\mathrm{p_t})} \cdot \sigma_{\mathrm{pA}}$$

and it was concluded [40, 41] that the two effects have a common origin ($\alpha \approx \beta$).

This recognition is used to extrapolate Pb-Au collision ($A = 208, B = 197$) (Fig. 9.4 dotted line) taking σ_{pp} from Alper et al. Even though the extrapolation seems to be closer to the data than the Alper parameterization alone, visible differences are still present in particular at small p_t.

A complementary way to analyze spectra is the study of the local inverse slope. In Fig. 9.6, we show, as a function of transverse mass $m_t - m_0$, the dependence of the local inverse slope for the data as well as for the previous parameterizations.

The Pb-Au data (circles), presented already in Fig. 9.3, are now compared with the results obtained from other collision systems. The full triangles are CERES results for identified π^- π^+ obtained in central S-Au collision at 200 GeV/c [45]. The cross is from p-p reactions measured at CERN ISR at $\sqrt{s} = 23GeV$ [46] and the star is p-p at 250 GeV/c as measured by NA22 [47]. From the comparison of those data to the Alper parameterization (dotted-dashed line), one notices that the Alper inverse slope agrees with the p-p data but is smaller than the values obtained in Pb-Au and S-Au data in the region of moderate m_t: $m_t - m_0 < 2.\ GeV/c^2$. The flattening of the p-p slope around 2 GeV/c^2 at a value $T \sim 250MeV$ signals the onset of hard parton scattering as new production mechanism of high-p_t pions [52]. One observes that the Pb-Au data exhibit the same saturation feature as the S-Au data. However, the local inverse slopes are significantly larger in the low m_t-region for the Pb-Au system. Therefore the m_t spectrum is closer to an exponential function than in the case of the smaller systems. This could be interpreted as a consequence of an increasing number of successive scatterings in the dense 'fireball' which in turn lead to a higher degree of thermalization. The extrapolation from

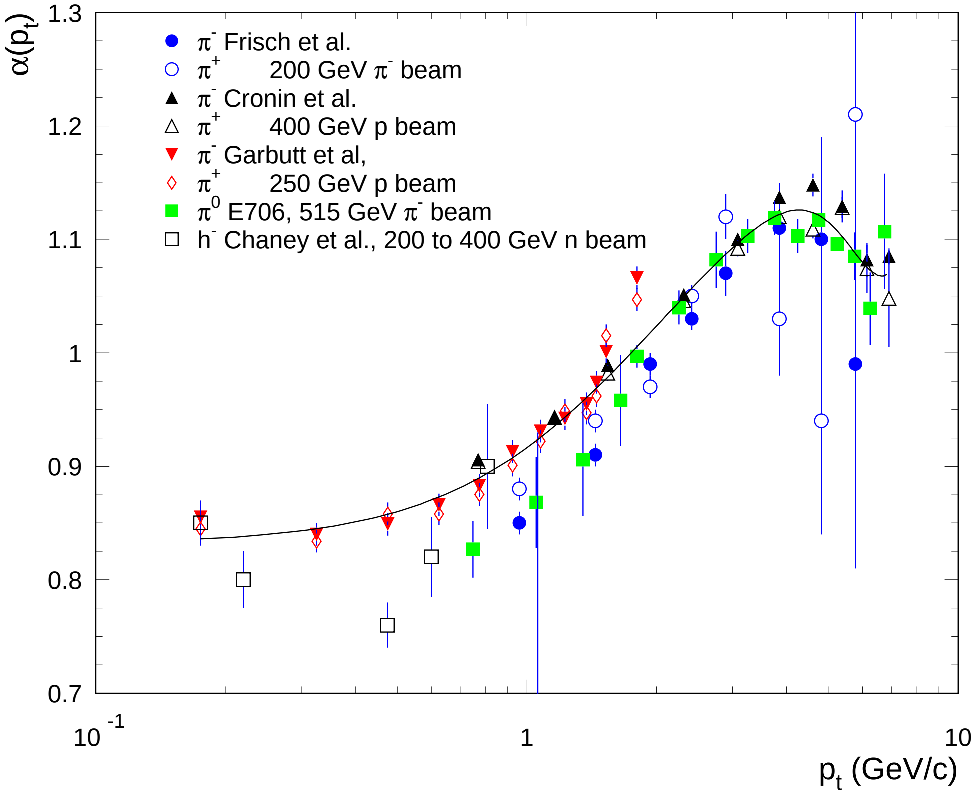

Figure 9.5: α exponent as a function of p_t.

pp to AB collisions tends to reproduce the S induced reactions while the Pb-Au data seems to saturate at lower p_t.

The Cronin effect has been interpreted as rescattering in the nuclear medium but on the parton level [42]. Combining both observations can suggest that the high degree of thermalization is reached early in the collision.

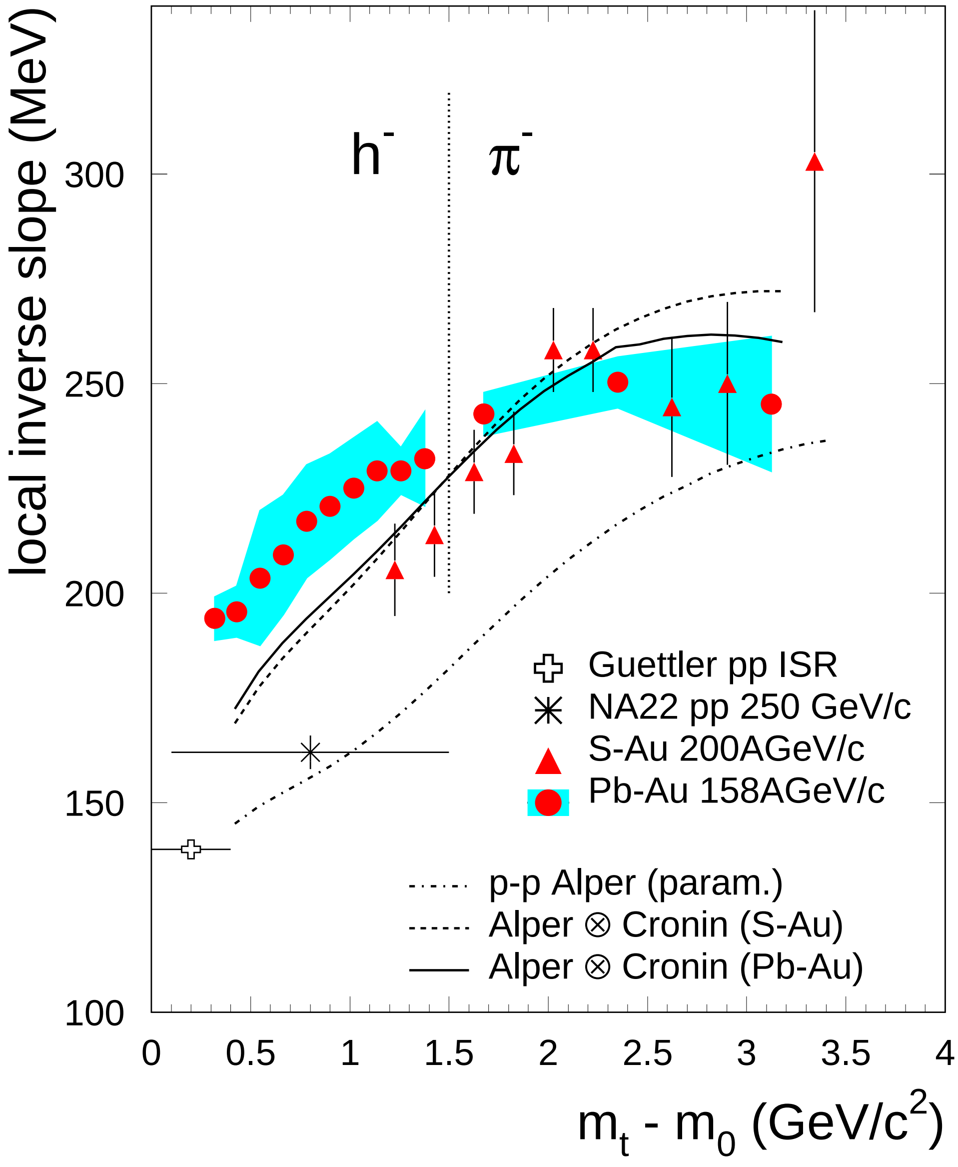

Figure 9.6: Local inverse slope analysis for different systems.

9.4 Hydrodynamical Model

The transverse mass spectra of the h^- and $h^+ - h^-$ as well as the distributions of all other particle (kaons, deuteron, etc.) can be interpreted in a complete different theoretical approach using a hydrodynamical model. In this case, the spectra are described by:

$$\frac{1}{m_t}\frac{dN}{dm_t} \propto \int_0^R r\ dr\ m_t I_0(\frac{p_t \sinh\rho}{T_f}) K_1(\frac{m_t \cosh\rho}{T_f}) \tag{9.2}$$

which represent the superposition of independent local thermal sources boosted with the angle $\rho = tanh^{-1}\beta(r)$. The term $\beta(r)$ is the transverse velocity of those local sources. It depends on the radius as $\beta(r) = \beta_s(r/R)^\alpha$ in the region $0 < r < R$ and on α which determines the velocity profile ($\alpha = 1/2, 1, 2$). I_0 and K_1 are modified Bessel functions. The flow velocity profile $\beta(r)$ depends on the initial conditions as well as on the underlying equation of state (EOS) which is altered in the presence of a first order phase transition [58].

The use of this function to fit the data does not yield a unique solution, different combinations of T_f and β_s can describe the data. For example, the effect of a high T_f and a small β_s is similar to that of a low T_f and a larger β_s.

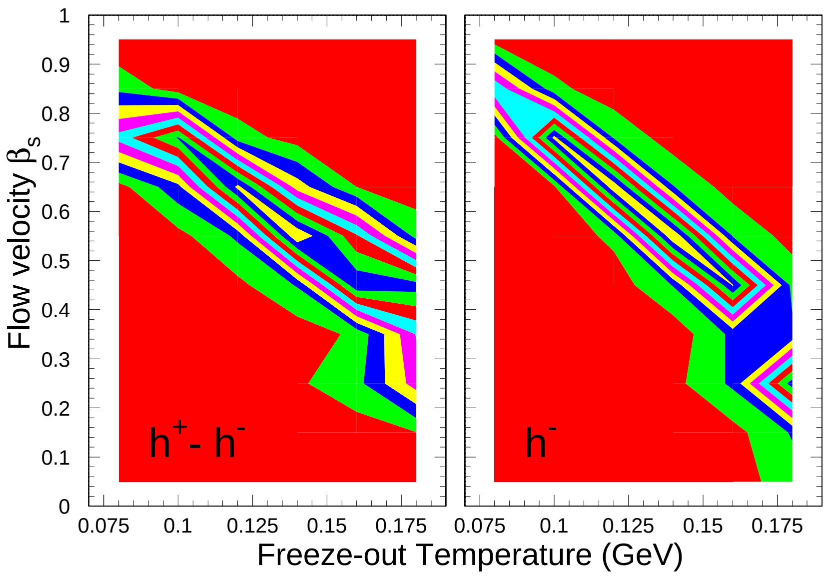

Figure 9.7: χ^2 contour map over the two dimensional space T_f and β_s for different velocity profiles.

To analyze the correlation between those two quantities, one can fit the data for all combinations and calculate for each pair (T_f, β_s) the χ^2. Fig. 9.7 presents the χ^2 map in the T_f and β_s plane obtained for $\alpha = 1$ (No resonance decays have been included). As one can see, equal values of the χ^2 are obtained starting from different freeze-out temperatures T_s and maximum velocity β_s, so that the data can be described with high temperature and small flow or low temperature and large flow. Choosing a $T_f = 140MeV$ results in a $\beta_s = 0.55 - 0.6$ which corresponds to a mean $\beta \sim 0.4$, in line with the results of NA44 [48, 55].

Since the hydrodynamical picture describes the reaction as a collective flow of matter with a certain velocity $\beta(r)$ common to all particles, it implies that the inverse slope parameter T, which is a measure of the particle energy, should depend on the mass of the particle. Indeed this effect is observed by several experiments [37, 53, 55] for different colliding systems [48, 55]. In Fig. 9.8, positive and negative particle of the same species, e.g. π^+ and π^-, have been averaged. Since, as already shown, the local slope of the m_t distributions changes significantly with m_t, the good agreement between the NA49 and NA44 (for $m_t - m_0 < 1\ GeV/c^2$) not necessarily match the slopes quoted for CERES (open points) which are measured at higher m_t where the spectra are nearly exponential. For pions also a value for low p_t is added. This results is more consistent with the other measurements.

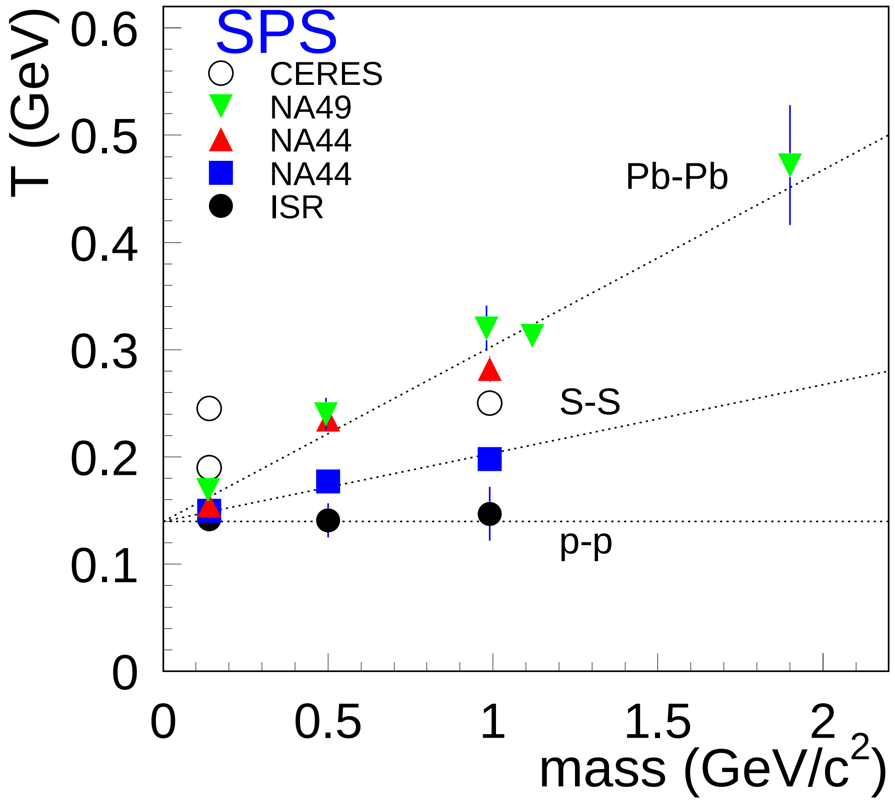

Figure 9.8: Dependence of the inverse slope T from particle mass and system as measured by Alper et al.,NA44, NA49, CERES (see text).

9.5 Random Walk

The random walk [49, 50] represents a possible theoretical explanation of the Cronin Effect. It is assumed that the successive collisions in nuclear reactions are much like elementary $p-p$ interactions. During such nucleon-nucleon scatterings, the polar angle of the projectile nucleon is generally not conserved. Further scatterings of the 'wounded' nucleon take place with respect to an axis different from the beam axis. Consequently the transverse momentum of the particles produced in the reaction will appear broader relative to the incident beam. The higher the number of scatterings, the larger the p_t broadening. In Fig. 9.9 [50], we present a comparison between random walk and hydrodynamical models for different velocity profiles: v_t-*const* assumes a constant velocity, v_t-*profile* instead a linear dependence between radius and v_t ($\alpha = 1$), and *hydro 2+1 dim* takes into account also a dependence of the freeze-out time from the radius. Only high quality data, covering the region from small $m_t - m_0$ to at least 2 GeV/c^2 can distinguish between the different models.

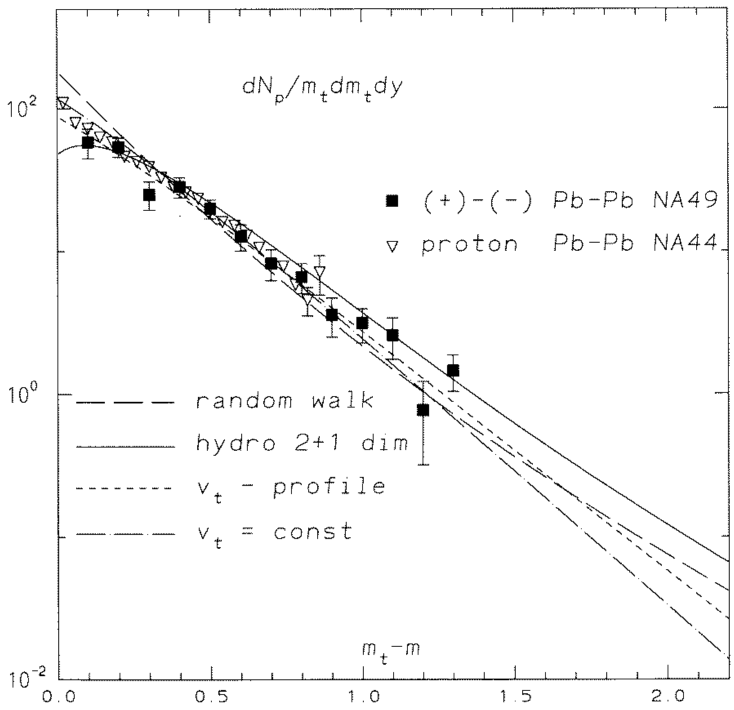

Figure 9.9: Comparison of different models.

The impact parameter dependence of the random walk as been investigated in reference [59]. In Fig. 9.10 (left), the comparison of the 'proton' data to the model is shown. From the top to the bottom different mean impact parameters 2, 2.5, 3.5, 4.3, 5.1, 6.0 and 7.4 fm are respectively plotted. The lines, corresponding to the prediction of the random walk model, describe only the most central collisions (upper curves) in the range from $0.7 < m_t - m_0 < 2\ GeV/c^2$. For more peripheral collisions, the model slopes are much steeper than the data.

The comparison of the inverse slope constant of the data (Fig. 7.18) and of the random walk calculations in the range $0.6 < m_t - m_0 < 2.\ GeV/c$ is illustrated more quantitatively in Fig. 9.10 (right). The conclusion [59] that one obtains from this picture is that the random walk model in its present form fails to describe the observed impact parameter dependence of the inverse slope constants.

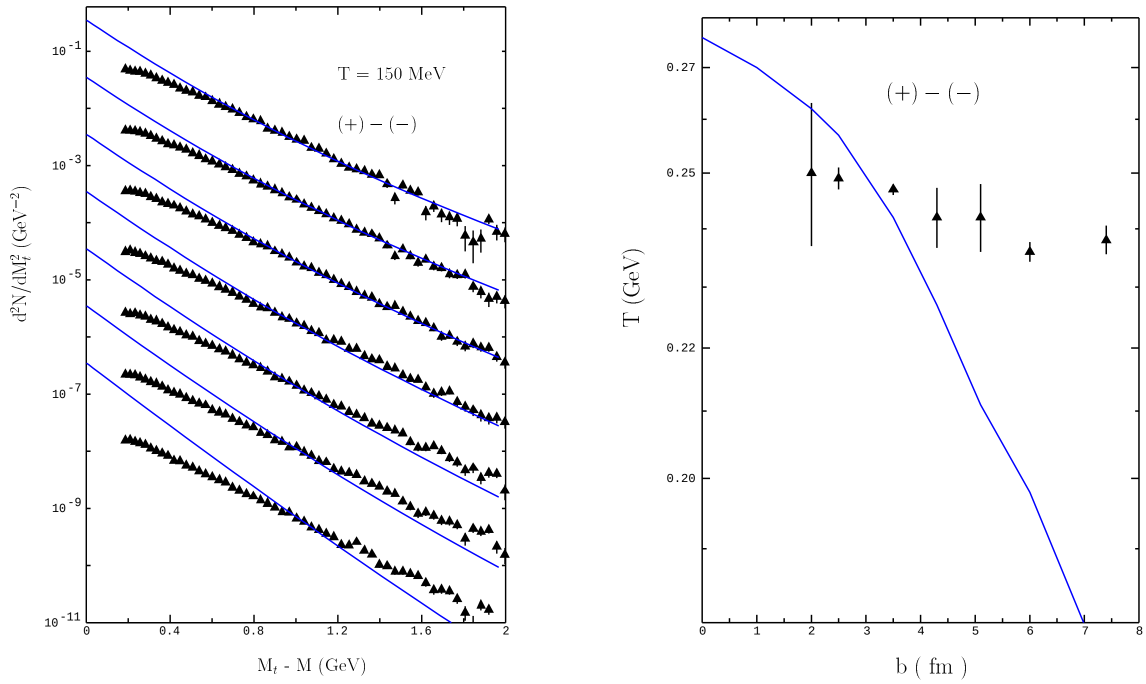

Figure 9.10: Comparison of the $h^+ - h^-$ spectra with predictions of the random walk model for different centralities (left) and measured inverse slope constants for data and random walk calculation.

Bibliography

[1] Th. Ullrich, Doktorarbeit, University Heidelberg, Germany (1994)

[2] C. Voigt, Doktorarbeit, University Heidelberg, Germany (1998)

[3] F. Karsch, Nucl. Phys. **A590** (1995) 367c

[4] T. Blum *et al.* Phys. Rev. **D51** (1995) 5153

[5] J.D. Bjorken, Phys. Rev. **D27** (1983) 140

[6] G.E. Brown, C.-H. Lee and R. Rapp, nucl-th/9712017

[7] J. Rafelski, Phys. Rep. **88** (1982) 331

[8] P. Koch, B. Muller and J. Rafelski, Phys. Rep. **142** (1986) 167

[9] T. Matsui and H. Satz, Phys. Lett. **B178** (1986) 416

[10] F. Karsch, M.T. Mehr and H. Satz, Z. Phys. **C37** (1988) 717

[11] C. Gale and J. Kapusta, Phys. Rev. **C35** (1987) 2107

[12] F. Karsch, K. Redlich and L. Turko Z. Phys. **C60** (1995) 519

[13] E. Schnedermann, J. Sollfrank and U. Heinz, Phys. Rev. **C48** (1993) 2462

[14] R. Baur *et al.* Nucl. Phys. **A566** (1994) 87c

[15] D. Irmscher *et al.* Nucl. Phys. **A566** (1994) 347c

[16] G. Agakichiev *et al.* Phys. Lett. B (1998) (in print)

[17] Proposal to the SPSLC, CERN SPSLC/94-1/P280

[18] CERES/NA45 Report to Cogne 1995, CERN SPSLC/95-20/M542

[19] U. Faschingbauer *et al.* Nucl.Instr.Meth., **A377** (1996) 362

[20] G. Agakichiev *et al.* Nucl.Instr.Meth., **A394** (1997) 225

[21] R. Baur *et al.*, Nucl.Instr.Meth. **A343** (1994) 87

[22] A. Breskin *et al.* IEEE Trans. Nucl. Sci. **35** (1988) 404

[23] G. Agakichiev *et al.* JINR Rapid Communications No.3[83] (1997) 17

[24] MINUIT, CERN PLLW D506/92/3

[25] B. Jaehne, Digitale Bildverarbeitung S.198 ff, Springer-Verlag

[26] A. Schön, Doctorarbeit, Univerisity Heidelberg (1993)

[27] R. Brun *et al.* CERN DD/EE/84-1

[28] G.A. Ososkov *et al.* Nucl.Instr.Meth. **A371** (1996) 243

[29] Particle Physics Booklet (July 1996)

[30] F. Ceretto *et al.*, Quark Matter 97, Proc.Int.Conf. on Ultra-Relativistic Nucleus-Nucleus Collisions, Tsukuba 1997

[31] C. Weber, Diplomarbeit, University Heidelberg, Germany (1997)

[32] T. Alber *et al.* (NA49 Coll.), Phys. Rev. Lett. **75** (1995) 3814

[33] K. Werner, Phys. Rep. **232** (1995) 87

[34] H. Sorge, Phys. Rev. **C52** (1995) 3291

[35] P. Jacobs (NA49 Collaboration) Jaipur, India, March 17-21, 1997.

[36] R. Baur *et al.* (CERES Collaboration) Z.Phys. **C71** (1996) 571

[37] B. Alper *et al.* Nucl.Phys. **B100** (1975) 237

[38] J.W. Cronin *et al.* Phys.Rev. **D11** (1975) 3105

[39] D. Antreasyan *et al.* Phys.Rev. **D19** (1979) 764

[40] A. Drees, Doktorarbeit, University Heidelberg, Germany (1989)

[41] T. Akesson *et al.* Z. Phys. **C46** (1990) 361

[42] M. Lev and B. Petersson, Z. Phys. **C21** (1983) 155

[43] D.A. Garbutt *et al.* Phys.Lett. **B67** (1977) 355

[44] D. Chaney *et al.* Phys.Rev. **D19** (1979) 3210

[45] B. Lenkeit, Diplomarbeit, University Heidelberg, Germany (1995)

[46] K. Guettler *et al.*, Phys.Lett. **B64** (1976) 111

[47] M. Adamus *et al.*, Z.Phys. **C39** (1988) 211

[48] S. Esumi, QCD Phase Transitions Proceeding, Hirschegg, Austria (1997) 355

[49] A. Leonidov *et al.*, Nucl.Phys. **A610** (1996) 124c

[50] H. Satz *et al.*, nuch-th/9707042

[51] J. Stachel, Nucl.Phys. **A610** (1996) 509c

[52] R.D. Field and R.P.Feymann, Phys. Rev. **D15** (1977) 2590

[53] G. Roland *et al.* (NA49 Collaboration), Quark Matter 97, Proc.Int.Conf. on Ultra-Relativistic Nucleus-Nucleus Collisions, Tsukuba 1997

[54] P.G. Jones *et al.* (NA49 Collaboration), Nucl.Phys. **A610** (1996) 188c

[55] Nu Xu *et al.* (NA44 Collaboration), Nucl.Phys. **A610** (1996) 175c

[56] Th. Peitzmann *et al.* (WA98 Collaboration), Nucl.Phys. **A610** (1996) 200c

[57] H.J. Frisch *et al.* Phys.Rev **D27** (1983) 1001

[58] D.H. Rischke, Nucl.Phys. **A610** (1996) 88c

[59] P. Braun-Munzinger and J. Stachel, Quark Matter 97, Proc.Int.Conf. on Ultra-Relativistic Nucleus-Nucleus Collisions, Tsukuba 1997

Appendix A

Kinematic variables

A.1 Rapidity

A useful variable, commonly used to quantify the longitudinal motion of particles with mass greater than 0. is the *rapidity* y, which is defined in terms of the energy and longitudinal momentum component of the particle, as:

$$\mathrm{y} = \frac{1}{2}\ln\frac{\mathrm{E}+\mathrm{p_z}}{\mathrm{E}-\mathrm{p_z}} \tag{A.1}$$

where E is the energy, $\mathrm{p_z}$ is the momentum component in beam direction.

The advantage of the rapidity variable can be seen in an easy transformation when changing the reference system for example from the lab system into the center of mass system. Under a Lorenz transformation from a reference system R to an other R' moving with velocity β_z in longitudinal direction, the rapidity y' (in R') is related to y (in R) just by an additive constant: $\mathrm{y}' = \mathrm{y} - \mathrm{y}_\beta$, where $\mathrm{y}_{\beta_\mathrm{z}}$ is the rapidity of the moving frame:

$$\mathrm{y}_\beta = \tfrac{1}{2}\ln(\tfrac{1+\beta_\mathrm{z}}{1-\beta_\mathrm{z}}). \tag{A.2}$$

For a given incident energy, the rapidity of the target and projectile nuclei can be calculated. In our case, the fixed target is at $\mathrm{y_{target}} = 0$ and the beam momentum $\mathrm{p_{beam}} = 158$ A GeV/c corresponds to a beam rapidity of $\mathrm{y_{beam}} = 5.84$. For symmetric systems, the center of mass system moves with a rapidity $y_{cm} = 0.5\ y_{beam}$ which is therefore also called mid-rapidity. In the limit of a particle with small mass the *pseudorapidity* η is often used. It can be calculated knowing the polar angle θ of the emitted particle:

$$\eta = -\ln(\tan\frac{\theta}{2}) \tag{A.3}$$

For large rapidities and small masses one has : $\eta \approx y$

A.2 Invariant Cross-Section

Usually in an experiment with Ultra Relativistic Heavy Ion Collision, only a restricted number of particles can be measured completely. Therefore most commonly inclusive cross-sections are evaluated. The *inclusive cross-section* describes the characteristic of a particular type of particle, independently from the remaining reaction products:

$$\mathrm{A} + \mathrm{B} \Longrightarrow \mathrm{h} + \mathrm{X}$$

in which A is the target nucleus, B is the projectile, h is the particle we are interested in and X is whatever.

The Lorenz-invariant single-particle spectra is defined through the invariant cross-section:

$$\mathrm{E} \cdot \frac{\mathrm{d}^3\sigma}{\mathrm{d}\mathbf{p^3}} = \frac{\mathrm{E}}{\pi} \frac{\mathrm{d}^2\sigma}{\mathrm{d}\mathrm{p}_\perp^2\ \mathrm{d}\mathrm{p}_\parallel} = \frac{1}{\pi} \frac{\mathrm{d}^2\sigma}{\mathrm{d}\mathrm{p}_\perp^2\ \mathrm{d}\mathrm{y}} = \frac{1}{2\pi \mathrm{p}_\perp} \frac{\mathrm{d}^2\sigma}{\mathrm{d}\mathrm{p}_\perp \mathrm{d}\mathrm{y}}$$

where E and **p** are respectively the energy and momentum of the detected particle, $\mathrm{p}_\perp$ or p_t is the component of **p** perpendicular to the beam direction and the $\mathrm{p}_\parallel$ is the parallel one. In addition to p_t another quantity, the transverse mass of a particle, is frequently used:

$$\mathrm{m}_\perp = \sqrt{\mathrm{p}_\perp^2 + \mathrm{m}_0^2} \qquad (\mathrm{m}_0 = \text{particle rest mass}),$$

From the definition of m_t it is easy to derive that:

$$\frac{1}{\mathrm{p}_\perp} \frac{\mathrm{d}\sigma}{\mathrm{d}\mathrm{p}_\perp} = \frac{1}{\mathrm{m}_\perp} \frac{\mathrm{d}\sigma}{\mathrm{d}\mathrm{m}_\perp}$$

Appendix B

$h^+ - h^-$ Spectra

The following plots show the transverse mass distributions of the positive charge excess ('net-proton' like spectra) for different centrality selections. The wide rapidity coverage ($y_{lab} = 1. - 2.5$) has been divided in 15 bins, each of $\Delta y = 0.1$. They are successively scaled by a factor of 10.

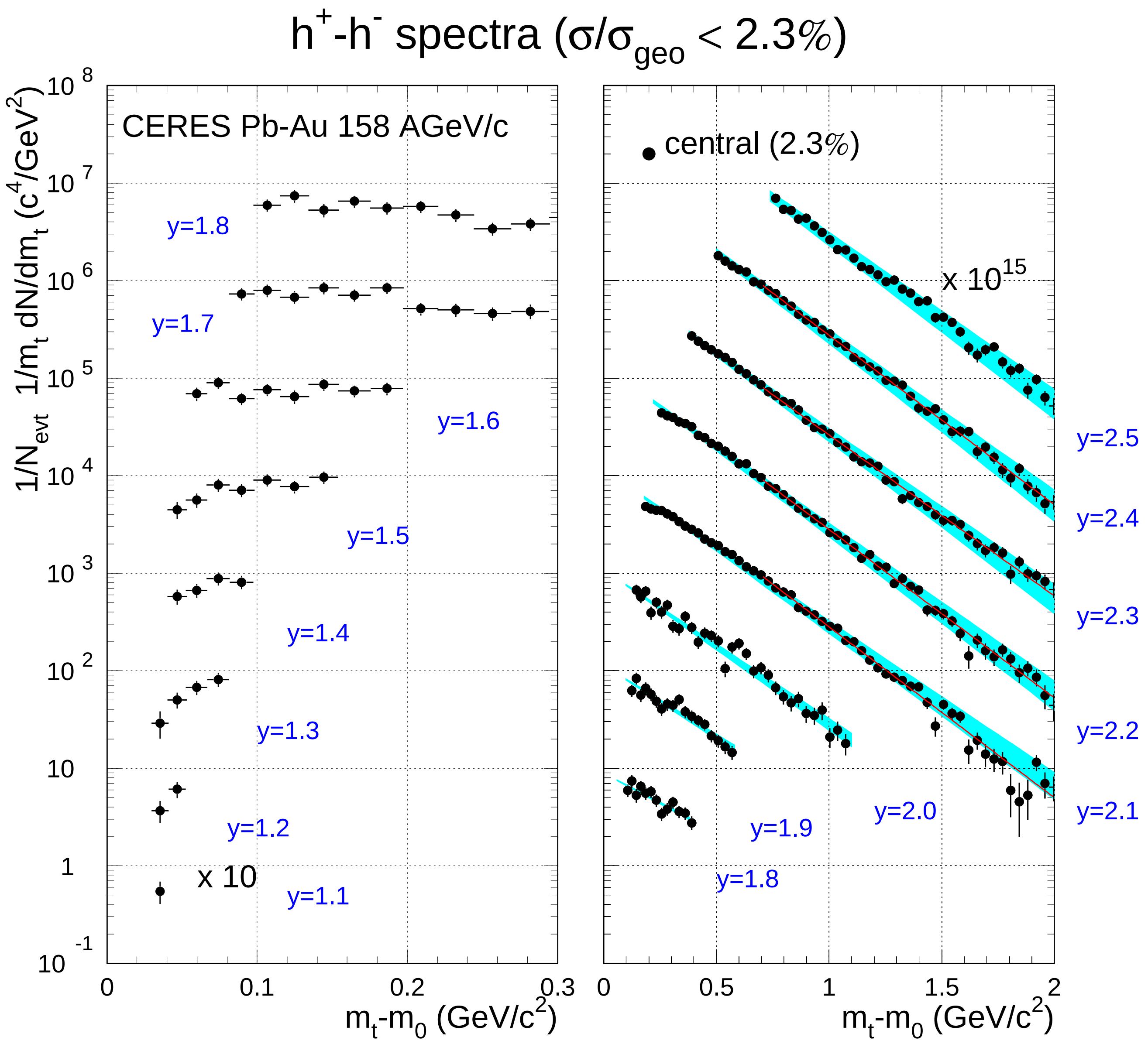

h+-h- spectra (σ/σgeo < 2.3%)
CERES Pb-Au 158 AGeV/c
central (2.3%)
1/Nevt 1/mt dN/dmt (c4/GeV2)
mt-m0 (GeV/c2)
x 10
x 1015
y=1.1
y=1.2
y=1.3
y=1.4
y=1.5
y=1.6
y=1.7
y=1.8
y=1.9
y=2.0
y=2.1
y=2.2
y=2.3
y=2.4
y=2.5

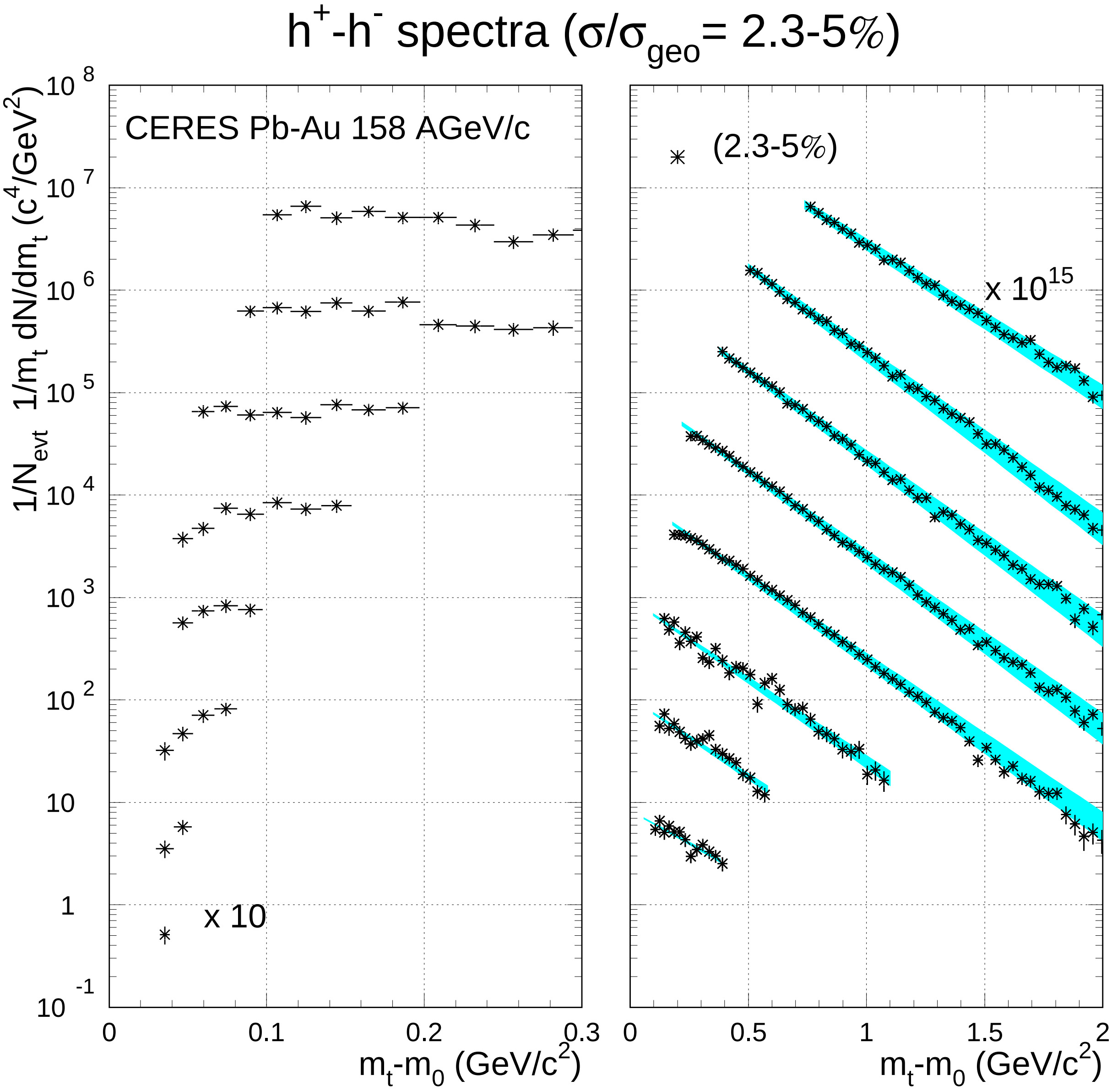

h+-h- spectra (σ/σgeo= 2.3-5%)
CERES Pb-Au 158 AGeV/c
(2.3-5%)
x 10^15
x 10
1/Nevt 1/mt dN/dmt (c^4/GeV^2)
mt-m0 (GeV/c^2)
mt-m0 (GeV/c^2)

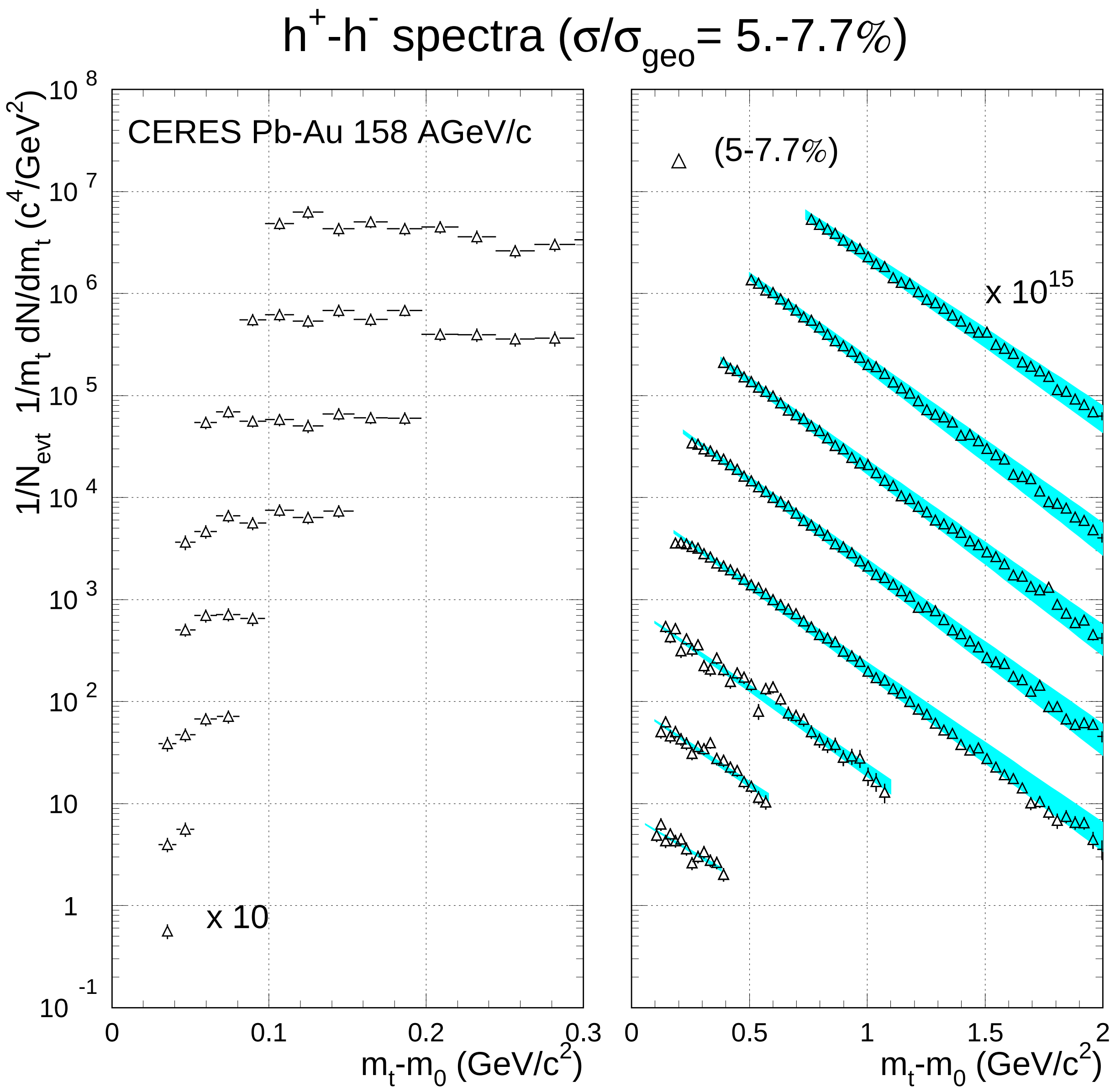
h+-h- spectra (σ/σgeo= 5.-7.7%)
CERES Pb-Au 158 AGeV/c
1/Nevt 1/mt dN/dmt (c4/GeV2)
x 10
(5-7.7%)
x 1015
mt-m0 (GeV/c2)
mt-m0 (GeV/c2)

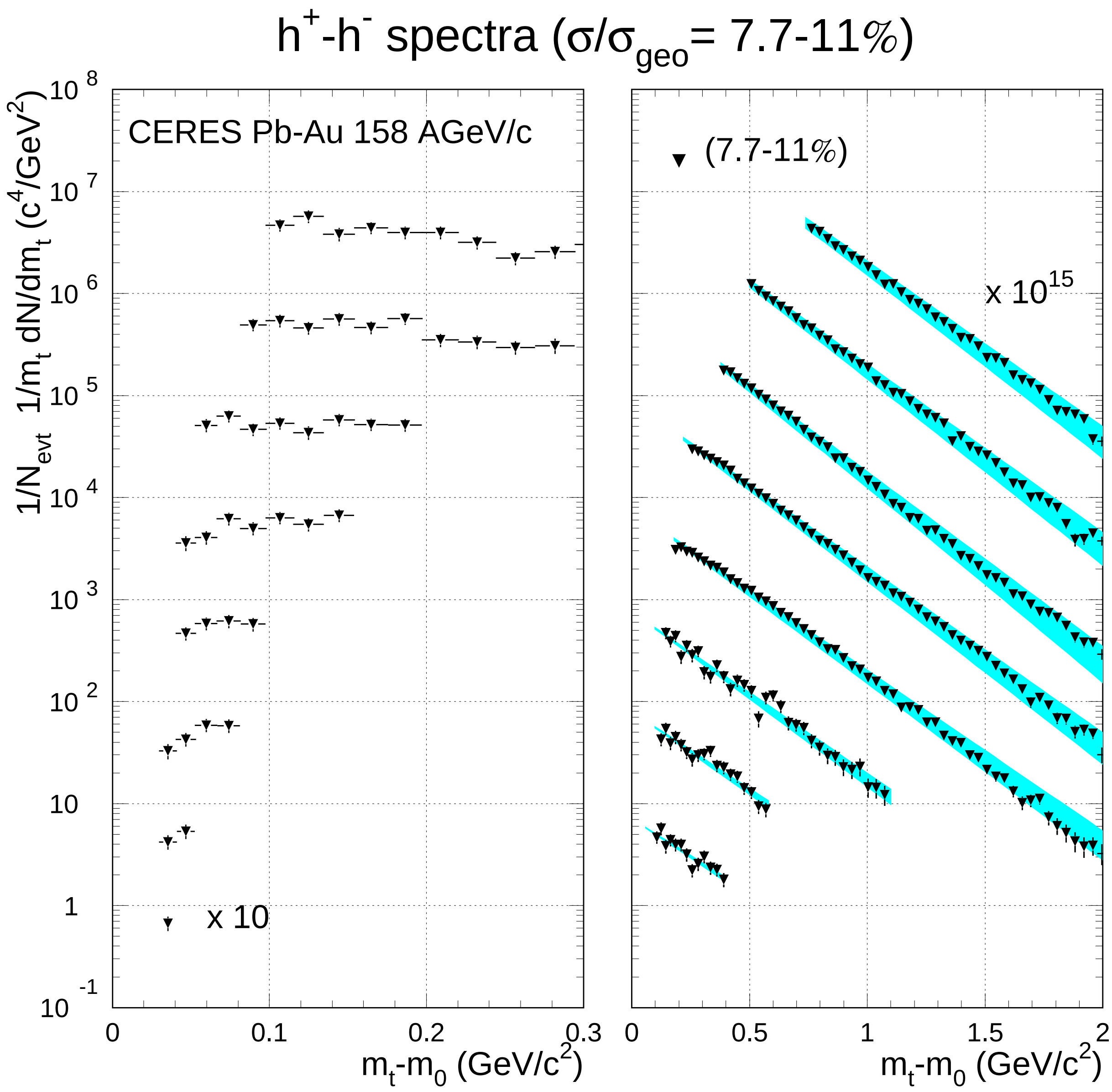

h+-h- spectra (σ/σgeo= 7.7-11%)
CERES Pb-Au 158 AGeV/c
(7.7-11%)
x 10
x 10^15
1/Nevt 1/mt dN/dmt (c^4/GeV^2)
mt-m0 (GeV/c^2)
mt-m0 (GeV/c^2)

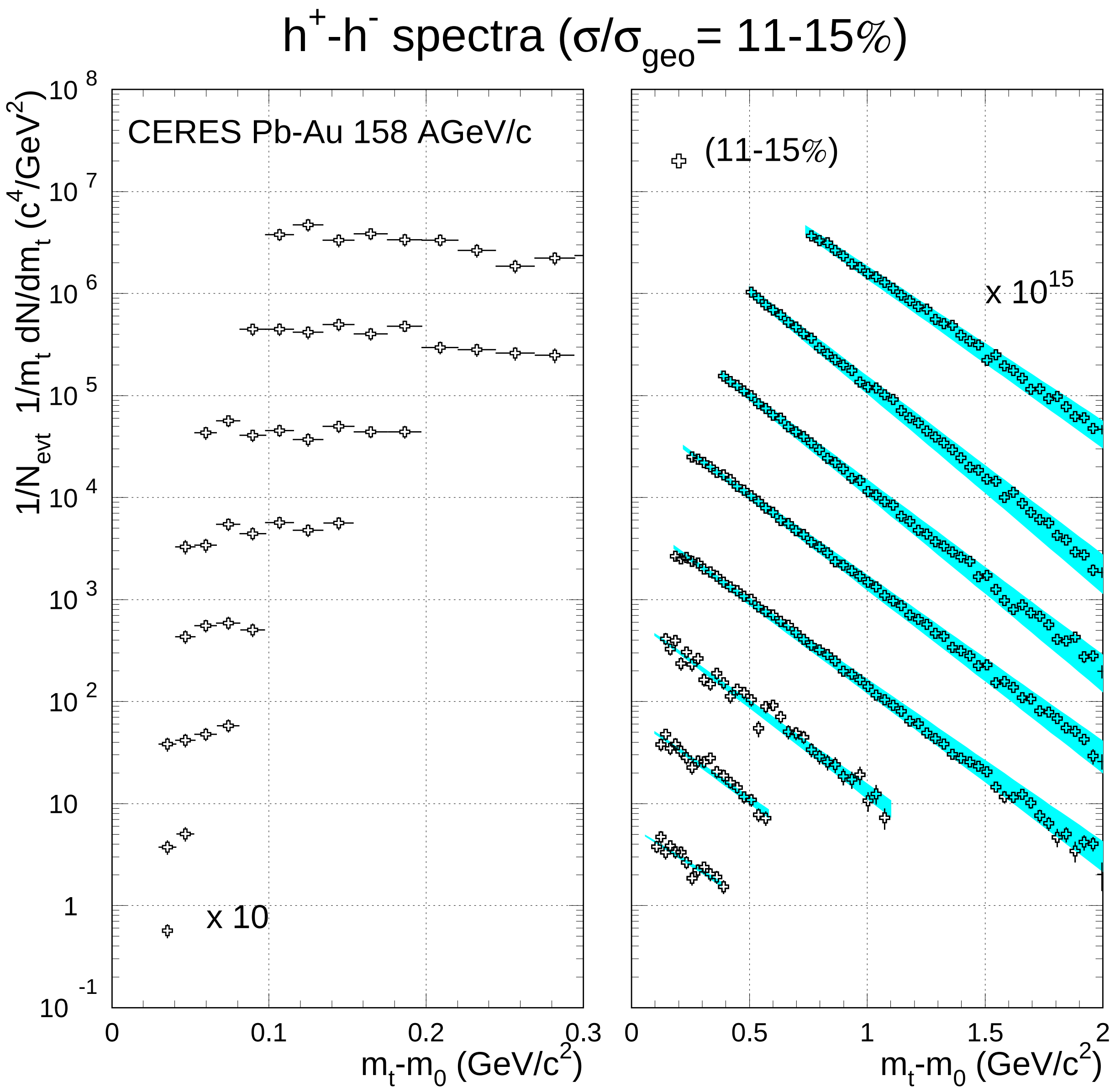
h+-h- spectra (σ/σgeo= 11-15%)
CERES Pb-Au 158 AGeV/c
1/Nevt 1/mt dN/dmt (c4/GeV2)
x 10
(11-15%)
x 1015
mt-m0 (GeV/c2)
mt-m0 (GeV/c2)

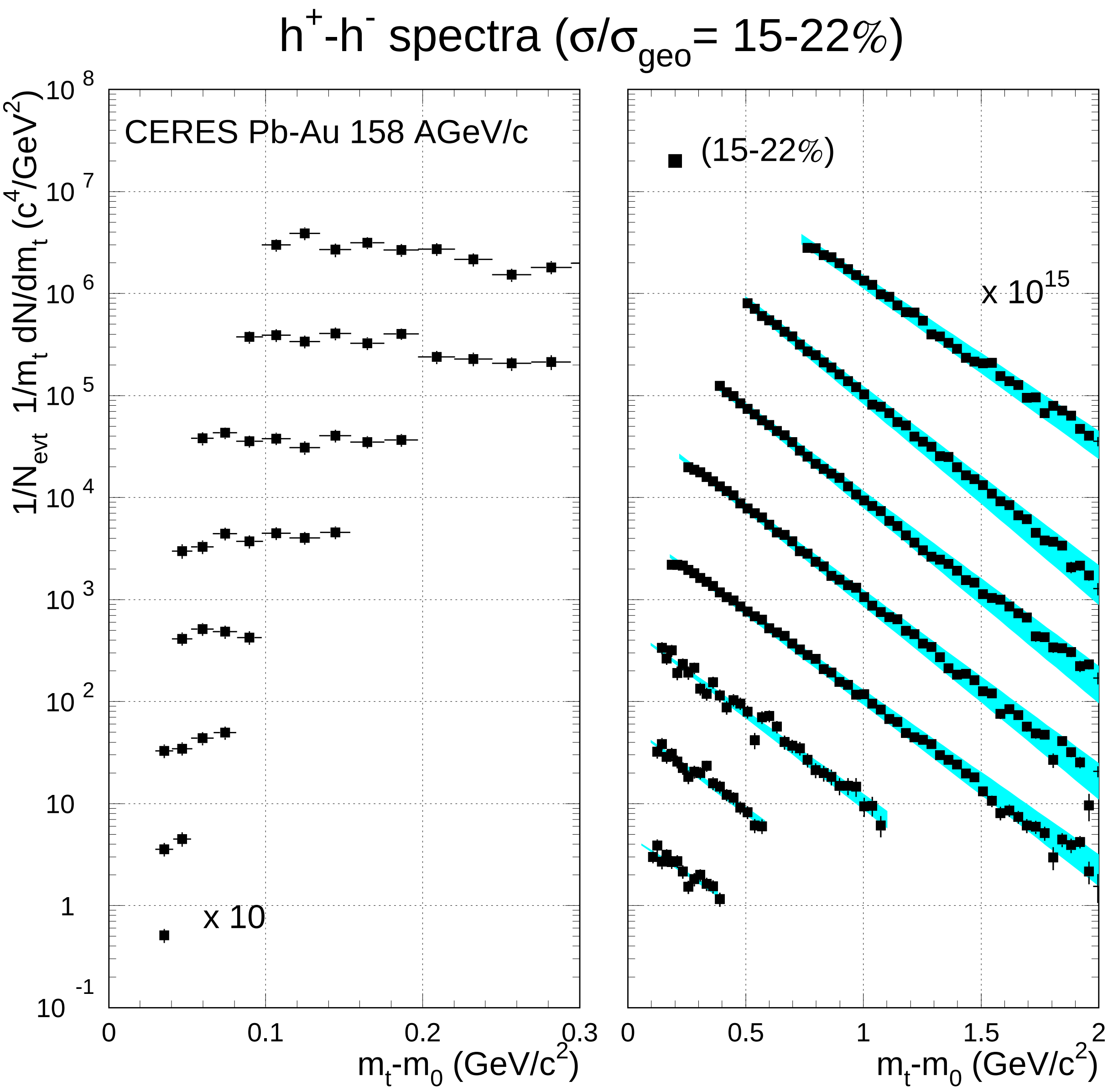
h+-h- spectra (σ/σgeo= 15-22%)
CERES Pb-Au 158 AGeV/c
1/Nevt 1/mt dN/dmt (c4/GeV2)
x 10
(15-22%)
x 1015
mt-m0 (GeV/c2)
mt-m0 (GeV/c2)

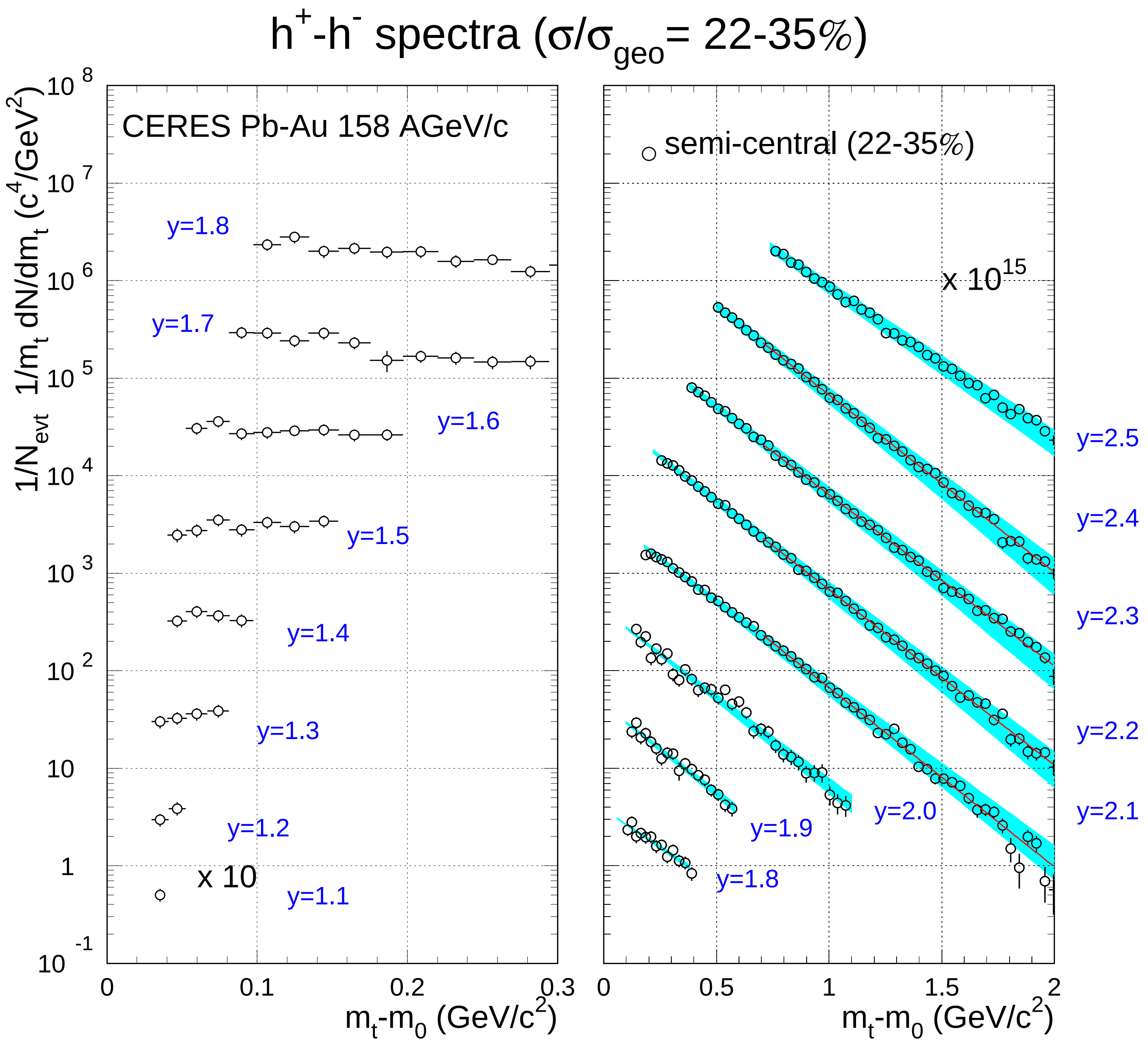
h+-h- spectra (σ/σgeo= 22-35%)
CERES Pb-Au 158 AGeV/c
semi-central (22-35%)
1/Nevt 1/mt dN/dmt (c4/GeV2)
mt-m0 (GeV/c2)
x 10
x 10^15
y=1.1
y=1.2
y=1.3
y=1.4
y=1.5
y=1.6
y=1.7
y=1.8
y=1.9
y=2.0
y=2.1
y=2.2
y=2.3
y=2.4
y=2.5

The CERES Collaboration

From 1994 to February 1998

Physikalisches Institut University Heidelberg
H. Appelshäuser, R. Baur, K. Dandl, A. Drees, P. Ernst, S. Esumi, P. Glässel, D. Irmscher, C. Jung, K. Lee, B. Lenkeit, L. Marquard, M. Messer, A. Pfeiffer, M. Richter, W. Schmitz, W. Seipp, H.J. Specht, J. Stachel, H. Tilsner, T.S. Ullrich, C. Voigt, C. Weber, J.P. Wessels, T. Wienold, B. Windelband
Guest of the University Heidelberg,
S. Voloshin

Max-Planck-Institut für Kernphysik, Heidelberg
F. Ceretto, U. Faschingbauer, Ch. Fuchs, M. Hemberger, O. Nix, J. Rak, J.P. Wurm

Gesellschaft für Schwerionenforschung, Darmstadt
P. Braun-Munzinger, G .Hering, A. Marin, D. Miskowiec, A. Sharma, P. Stiller

Weizmann Institure of Science, Rehovot, Israel
A. Cherlin, Z. Fraenkel, C. P. de losHeros, A. Gnaenski, A. Milov, I. Ravinovich, E. Socol, G. Tel-Zur, I. Tserruya

CERN, Genf, Schweiz
J. Schukraft

Brookhaven National Laboratory, Brookhaven, USA
P. Rehak, H. Kraner, P. Holl

Politecnico di Milano, Milan, Italy
E. Gatti, M. Sampietro

Joint Institute for Nuclear Research, Dubna, Russia
G. Agakischiev, Y. Minaev, Y. Panebrattsev, S. Razin, N. Saveljic, S. Schimansky, V. Yurevich

Acknowledgments

I would like to thank Prof. J.P. Wurm for the possibility he gave me to work in CERES, Prof. H.J. Specht, Prof. J. Stachel, Prof. P. Glassel for the interesting discussions and advices at every Friday meeting, Priv. Doz. Norbert Herrmann for reviewing this thesis, Axel for his professional guidance and for teaching me the most important German word, Thomas for his helpful suggestions, his infinite patience and continuous correction of my English, Andreas for his pleasant humor and for 'die schnellste DAQ der Welt', Johannes for his support in Japan, Sergei for introducing me to the field of the anisotropic flow, ShinIchi for the (hydro)-dynamical discussions, the Post-docs: Christian, Jan, Roland and the electronic group: Wolfram, Michael for the hard work at CERN, all the PhD students that have worked with me and in particular Carsten for the 'theoretic' explanation of C++, Björn for the Monte-Carlo simulation, Natasha for the discussion from girl to girl, Matthias for the crazy physics conversations until late night and for teaching me how to cook, swim, speak German and drink wine without becoming 'Besoffen',my family Mami, Papi, Albi, Dani, la mia Nonna e Yankee per i continui incoraggiamenti e le calorose accoglienze a casa.